

Using Computational Fluid Dynamics and Fluid–Structure Interaction to Study Upper Airway Occlusion in Obstructive Sleep Apnea

by
Moyin Zhao

A thesis submitted to fulfil the requirements for
admission to the degree of Doctor of Philosophy
of The University of New South Wales



Department of Mechanical and Manufacturing Engineering
The University of New South Wales
Sydney, Australia
March 2014

PLEASE TYPE

THE UNIVERSITY OF NEW SOUTH WALES
Thesis/Dissertation Sheet

Surname or Family name: Zhao

First name: Moyin

Other name/s:

Abbreviation for degree as given in the University calendar: Phd

School: Mechanical engineering and Manufacturing

Faculty:Engineering

Title: Using Computational Fluid Dynamics and Fluid-Structure Interaction to Study Upper Airway Occlusion in Obstructive Sleep Apnea

Abstract 350 words maximum: (PLEASE TYPE)

This thesis used the computational fluid dynamics (CFD) method to analyse the therapeutic effect of an oral device (mandibular advancement splint—MAS) that protrudes the lower jaw during sleep as a treatment for obstructive sleep apnea (OSA). Anatomically-accurate upper airway (UA) computational models were reconstructed from magnetic resonance images of seven patients with and without an MAS device fitted. CFD simulations of UA airflow were performed at the maximum flow rate during inspiration. The CFD results indicated that the lowest pressure often occurred close to the soft palate and base of the tongue. The airway pressure gradient was estimated as the best indicator for treatment response, since the change in the pressure drop formed a linear correlation with the change in the patients' apnea-hypopnea index. This correlation has the potential to be developed into a model for predicting the outcome of MAS treatment. However, the rigid wall assumption of CFD models was a major uncertainty. To overcome this uncertainty, we set up a full fluid-structure interaction (FSI) model with a typical responder case with a compliant UA wall. The results demonstrated the different UA flow field associated with alleviated the airway collapse by MAS, which was successfully predicted for the untreated patient. Thus, this thesis shows for the first time that FSI is more accurate than CFD with rigid walls for the study of sleep apnea, and can predict treatment response. Through comparison with the CFD results, more realistic UA flow and pressure profiles were found in the FSI analysis, which proved FSI to be a more suitable approach to investigate OSA problems with severe UA collapse.

Declaration relating to disposition of project thesis/dissertation

I hereby grant to the University of New South Wales or its agents the right to archive and to make available my thesis or dissertation in whole or in part in the University libraries in all forms of media, now or here after known, subject to the provisions of the Copyright Act 1968. I retain all property rights, such as patent rights. I also retain the right to use in future works (such as articles or books) all or part of this thesis or dissertation.

I also authorise University Microfilms to use the 350 word abstract of my thesis in Dissertation Abstracts International (this is applicable to doctoral theses only).

.....
Signature

.....
Witness Signature

.....
Date

The University recognises that there may be exceptional circumstances requiring restrictions on copying or conditions on use. Requests for restriction for a period of up to 2 years must be made in writing. Requests for a longer period of restriction may be considered in exceptional circumstances and require the approval of the Dean of Graduate Research.

FOR OFFICE USE ONLY

Date of completion of requirements for Award:

COPYRIGHT STATEMENT

'I hereby grant the University of New South Wales or its agents the right to archive and to make available my thesis or dissertation in whole or part in the University libraries in all forms of media, now or here after known, subject to the provisions of the Copyright Act 1968. I retain all proprietary rights, such as patent rights. I also retain the right to use in future works (such as articles or books) all or part of this thesis or dissertation.

I also authorise University Microfilms to use the 350 word abstract of my thesis in Dissertation Abstract International (this is applicable to doctoral theses only).

I have either used no substantial portions of copyright material in my thesis or I have obtained permission to use copyright material; where permission has not been granted I have applied/will apply for a partial restriction of the digital copy of my thesis or dissertation.'

Signed

Date

AUTHENTICITY STATEMENT

'I certify that the Library deposit digital copy is a direct equivalent of the final officially approved version of my thesis. No emendation of content has occurred and if there are any minor variations in formatting, they are the result of the conversion to digital format.'

Signed

Date

ORIGINALITY STATEMENT

'I hereby declare that this submission is my own work and to the best of my knowledge it contains no materials previously published or written by another person, or substantial proportions of material which have been accepted for the award of any other degree or diploma at UNSW or any other educational institution, except where due acknowledgement is made in the thesis. Any contribution made to the research by others, with whom I have worked at UNSW or elsewhere, is explicitly acknowledged in the thesis. I also declare that the intellectual content of this thesis is the product of my own work, except to the extent that assistance from others in the project's design and conception or in style, presentation and linguistic expression is acknowledged.'

Signed

Date

Abstract

This thesis used the computational fluid dynamics (CFD) method to analyse the therapeutic effect of an oral device (mandibular advancement splint—MAS) that protrudes the lower jaw during sleep as a treatment for obstructive sleep apnea (OSA). Anatomically-accurate upper airway (UA) computational models were reconstructed from magnetic resonance images of seven patients with and without an MAS device fitted. CFD simulations of UA airflow were performed at the maximum flow rate during inspiration. The CFD results indicated that the lowest pressure often occurred close to the soft palate and base of the tongue. The airway pressure gradient was estimated as the best indicator for treatment response, since the change in the pressure drop formed a linear correlation with the change in the patients' apnea-hypopnea index. This correlation has the potential to be developed into a model for predicting the outcome of MAS treatment. However, the rigid wall assumption of CFD models was a major uncertainty. To overcome this uncertainty, we set up a full fluid–structure interaction (FSI) model with a typical responder case with a compliant UA wall. The results demonstrated the different UA flow field associated with alleviated the airway collapse by MAS, which was successfully predicted for the untreated patient. Thus, this thesis shows for the first time that FSI is more accurate than CFD with rigid walls for the study of sleep apnea, and can predict treatment response. Through comparison with the CFD results, more realistic UA flow and pressure profiles were found in the FSI analysis, which proved FSI to be a more suitable approach to investigate OSA problems with severe UA collapse.

Declaration of Originality

I certify that this thesis does not incorporate without acknowledgement any material previously submitted for a degree or diploma in any university; and that to the best of my knowledge and belief it does not contain any material previously published or written by another person except where due reference is made in the text.

Signed: _____ On: ____/____/____

Acknowledgements

I would like to thank my supervisors, Professor Gary Rosengarten, Associate Professor Tracie Barber and Associate Supervisor Professor Anne Clinton, for their support and guidance throughout my study. They always helped guide me to solve problems regarding experiment setup and simulation. Since I am not a native speaker of English, they were also very patient in helping me overcome my difficulties in English writing and speaking. I also want to sincerely thank my conjunction supervisor, Professor Peter A. Cistulli, and colleague, Dr Kate Sutherland. They provided significant advice to me regarding knowledge in the medical field. The validating experiments of this project were supported by four undergraduate students: Cicily, Miriam, Josh and Arjun. Thank you all for your effort in this project. Sometimes it was not easy, but we did it. Finally, I wish to thank to my family—without your support, I would not have been able to travel to Australia and finish my PhD degree. Thank you to Judi, my wife; Ming, my mother; and Yenshen, my father. You gave me the encouragement to join the academic field.

Publication List

Journal Publications

- Zhao M, Barbar T, Cistulli P, Sutherland K and Rosengarten G 2013. Computational fluid dynamics for the assessment of upper airway response to oral appliance treatment in obstructive sleep apnea. *Journal of Biomechanics*, 46, 142–150.
- Zhao M et al. 2013. Simulation of upper airway occlusion without and with mandibular advancement in obstructive sleep apnea using fluid-structure interaction. *Journal of Biomechanics*, 46(15), 2586–2592.

Conference Publications

- Zhao M, Barbar T, Cistulli P, Sutherland K and Rosengarten G 2010. Computational fluid dynamic study of upper airway flow to predict the success of oral appliances in treating sleep apnea. 17th Australian Fluid Mechanics Conference, Auckland, New Zealand.
- Zhao M, Rosengarten G, Sutherland K, Barber T and Cistulli P 2011. Understanding pharyngeal airflow and upper airway collapse in OSA: Use of computational fluid dynamics and fluid-structure interaction. *Journal of Sleep Research* 20(Suppl 1), 27.
- Zhao M, Rosengarten G, Barber T, Sutherland K, Grunstein RR and Cistulli PA 2010. Computational fluid analysis of the effect of mandibular advancement on pharyngeal air flow in obstructive sleep apnoea. *Sleep and Biological Rhythms* 8(Suppl 1), A49.
- Zhao M, Barbar T, Cistulli P, Sutherland K and Rosengarten G 2013. Predicting the treatment response of oral appliances for obstructive sleep apnea using computational fluid dynamics and fluid-structure interaction. IMECE (paper accepted).
- Zhao M, Barbar T, Cistulli P, Sutherland K and Rosengarten G 2013. Using

two-way fluid-structure interaction to study the collapse of the upper airway of OSA patients. ACCM (paper accepted).

Contents

Abstract	i
Declaration of Originality	ii
Acknowledgements	iii
Publication List	iv
Contents	vi
List of Figures	ix
List of Tables	xii
Nomenclature	xiii
Chapter 1: Introduction	1
1.1 History of Obstructive Sleep Apnea	1
1.2 Consequences and Clinical Symptoms of Obstructive Sleep Apnea Syndrome.....	2
1.3 Demographic Studies	2
1.4 Anatomical Study of Human Upper Airway.....	3
1.5 Risk Factors.....	4
1.6 Obstructive Sleep Apnea Diagnosing Methodologies and Medical Treatments ...	5
1.7 Aim of this Thesis	7
1.8 Structure of the Thesis	8
Chapter 2: Literature Review	9
2.1 Introduction	9
2.2 Computational Fluid Dynamics Simulation.....	9
2.2.1 Modelling and 3D Reconstruction of Human UA	9
2.2.2 Meshing by Using Commercial Programs	14
2.2.3 Boundary Conditions	15
2.2.4 Turbulence Modelling of UA Flow	16
2.2.5 Similarities of the Findings in UA Flow Modelling	18
2.3 Experimental Validation	19
2.3.1 Simple Physical UA Models in an Early Stage.....	19
2.3.2 Geometrically-accurate UA Models	20
2.4 Fluid–structure Interaction	23
2.5 Study Significance and Summary	25
Chapter 3: Research Methodology	27
3.1 Introduction	27
3.2 Study Case.....	29
3.3 Reconstruction of UA Geometry	31
3.4 The Computational Grid	34
3.5 Advection Scheme	38
3.6 Governing Equation of CFD Models	38
3.7 Boundary Conditions	42
3.8 The Solution Process.....	43
3.9 Experimental Validation of the CFD Model.....	43
3.9.1 The Rigid Experimental UA Model.....	43
3.9.2 Supply and Regulate the Flow	44

3.9.3 Acquire Pressure Profile	45
3.10 Modelling the Flexible UA Model: The FSI Method	47
3.10.1 Study Case.....	47
3.10.2 Defining Geometries of the FSI Model.....	48
3.10.3 Computational Grid for the FSI Model.....	51
3.10.4 Governing Equations for FSI	52
3.10.5 Boundary Conditions for FSI Models	54
3.10.6 FSI Coupling and Solving the FSI Model.....	55
3.11 Experiment Method to validate the FSI Result	56
3.12 Design of the Flexible Experimental UA Model	56
3.12.1 Measuring the Material Property of the Flexible Experimental UA Model.....	57
3.12.2 Experimental Setup	58
3.12.2.1 <i>Flow Supply and Regulation</i>	58
3.12.2.2 <i>Measurement of the Wall Deformation</i>	59
3.13 Summary	60
Chapter 4: Results: Pressure and Velocity Field	62
4.1 Introduction	62
4.2 Validation of the CFD Results	62
4.2.1 Comparison Experiments with CFD	62
4.2.2 The Uncertainty in Experimental Results	64
4.2.2.1 <i>Pitot-static Tube Errors</i>	64
4.2.2.2 <i>Manometer Errors</i>	65
4.2.2.3 <i>Time Averaging</i>	65
4.2.2.4 <i>Geometry Tolerance</i>	66
4.2.2.5 <i>Overall Error</i>	66
4.3 Geometrical Changes before and after MAS Treatment.....	67
4.3.1 Restriction in the UA	67
4.3.2 The Changes of UA Geometry by MAS	72
4.4 The Multi-case CFD Result: Flow Patterns	75
4.5 UA Pressure Profiles of Responder-1	80
4.6 UA Quantitative Pressure Profile in All Cases	82
4.7 Relationship with Treatment Outcome	84
4.8 Summary	87
Chapter 5: Fluid Structure Interaction Results of Collapsible UA Models	88
5.1 Introduction	88
5.2 Validation of UA Deformations.....	88
5.2.1 Comparison of Wall Deformation in the Experimental and FSI Models	88
5.2.2 The Uncertainty in Experimental Results	90
5.3 FSI Results of Responder.....	91
5.3.1 Deformation of the UA Wall	91
5.3.2 Velocity Profile	92
5.3.3 Pressure Distribution.....	94
5.4 FSI Result of a Failure Case.....	96
5.4.1 Wall Deformation and Velocity Vector	96
5.4.2 Pressure Distribution.....	98
5.4.3 UA Wall Oscillation.....	100
5.5 Comparison of CFD with FSI	102
5.6 Summary	109

Chapter 6: Conclusion and Discussion.....	110
6.1 Introduction	110
6.2 Conclusions	110
6.3 Discussion and Recommendations for Future Research	112
References	115
Appendix A: The Computational Code for Structural Analysis of UA Wall.....	120
Appendix B: The Study Case Data Sheet.....	121
Appendix C: Engineering Drawings	122

List of Figures

Figure 1: Anatomy of the Human UA [21].....	3
Figure 2: A Regular PSG Record [36].....	5
Figure 3: A Custom-made MAS	7
Figure 4: 1:1 Scale Human UA Medical School Teaching Model [48].....	9
Figure 5: The ‘Weibel A’ Idealised Human UA Model [49].....	10
Figure 6: Defined Boundaries for the Pharynx in the Study by Huynh et al. [28].....	12
Figure 7: Velocity Streamlines in the Pharynx Model [28]	12
Figure 8: Velocity Streamline in the Nasal Model [52].....	13
Figure 9: Velocity Streamline in Pharynx Model [25]	14
Figure 10: Typical Pharynx Jet in Simulation Results [48].....	19
Figure 11: Physical Respiratory Experiment Setup by Heenan et al. [45].....	20
Figure 12: Experiment Procedure and Equipment of Xu et al. [51]	21
Figure 13: Experiment in Mylavaram et al.’s Validation Process [60].....	22
Figure 14: Deformable Wall Effects Indicated by Xu et al. [51].....	23
Figure 15: Initial Position (Grids) and Displacement Distribution of Soft Palate Presented in Wang et al. [63]	25
Figure 16: Study Flow Chart of CFD, FSI and Experiment	29
Figure 17: The Custom-made Two-piece MAS.....	30
Figure 18: Definition of Upper and Lower Boundaries of UA Model in this Thesis	31
Figure 19: UA Lumen Marked in a Transverse MRI Scan of an OSA Patient.....	32
Figure 20: Reconstruction of the UA Geometry in Amira 5.....	33
Figure 21: UA Geometrical Changes (a) Before and (b) After Smooth Function in Amira 5. (c) Comparison between Unsmoothed (Green) and Smoothed (Red) UA Boundary Line.....	34
Figure 22: STL Surface Model Exported from Amira 5.0 to Meshing Software ICEM.....	35
Figure 23: Unstructured Surface Grid for UA Geometry	36
Figure 24: Hybrid Mesh for Complex UA Geometry	37
Figure 25: Plot of Axial Velocity along a Vertical Line (Showing from the Right) from the Inlet to the Wall of the Larynx with Different Mesh Densities.....	38

Figure 26: Comparison Study of UA Pressure Distribution by Experiment and Turbulence Models along the UA at a Flow Rate of 10 L/min (166 ml/s)	42
Figure 27: Rigid UA Model Fabricated with the Rapid Prototyping Method	44
Figure 28: Equipment Setup for Pressure Measurement	45
Figure 29: (a) Inlet and (b) Outlet Connection Design to Provide a Smooth Flow Transition by Transferring the Irregular UA Boundary to the Circular Pipe Profile.....	45
Figure 30: Vertical Velocity Profile of Airflow in the Connecting Pipe	46
Figure 31: Reconstruction of UA Geometries (a) Before and (b) After MAS Treatment	47
Figure 32: Procedures of Establishing Engineering Airway Model in Pro/E	49
Figure 33: Comparison of the CFD Result of the Unsmoothed UA Geometry Used in CFD and the Smoothed Geometry used in FSI Simulation.	49
Figure 34: Geometries of the (a) Fluid and (b) Solid Domain of Responder-1 in Pre-treatment Condition.....	50
Figure 35: Geometries of the (a) Fluid and (b) Solid Domain of Responder-1 in Post-treatment Condition	51
Figure 36: Computational Grids for (a) Fluid and (b) Solid Domains.....	51
Figure 37: Plot of the Displacement as a Function of Time of a Point Located at the Tongue Base Position 55 mm from the Inlet for Different Numbers of Mesh Points in the Solid Wall.....	52
Figure 38: Sinusoidal Flow Profile of the Inspiratory Flow	55
Figure 39: Flowchart of Using MFX to Perform a Transient FSI Simulation.....	56
Figure 40: 1:1 STL Model of the Pre-treatment UA Geometry.....	57
Figure 41: Photographs of the Instron 5543 Mechanical Testing Machine Used to Perform Tensile Tests of the Material Properties of the SLA Resin.....	58
Figure 42: Experimental Setup for Validating the FSI Analysis	59
Figure 43: Image of the Collapse Recorded by High-speed Camera: (a) UA Model Un-deformed and (b) UA Model Fully Deformed.....	59
Figure 44: Velocity Vector on the Mid-sagittal Plane of the CFD Result.....	63
Figure 45: Validation of CFD Method by Comparing the Wall Pressure Distribution ..	64
Figure 46: Time Variation of Pressure Readings in Manometers—Single Result Set ...	66
Figure 47: Amira Reconstructed 3D Images of the UA Geometry of Seven Patient Cases before and after MAS Treatment	71

Figure 48: Correlation between the Percentage Changes in the UA Volume ($\Delta\text{Volume}\%$) and AHI ($\Delta\text{AHI}\%$) before and after MAS Treatment	72
Figure 49: Correlation between the Percentage Changes in the Minimum Cross-sectional area ($\Delta\text{CSArea}\%$) and AHI ($\Delta\text{AHI}\%$) before and after MAS Treatment	73
Figure 50: Maximum Turbulence Kinetic Energy Profile of Non-responder Post-treatment Case	74
Figure 51: UA Flow Streamline of All Patient Cases Pre- and Post-treatment	78
Figure 52: UA Flow Vector Plot at the Vertical Mid-plane of UA	80
Figure 53: 2D Pressure Contours on the Mid-plane of the UA Model of Responder-1, before and after MAS Treatment	81
Figure 54: Pressure Represented by Horizontal Slices in the UA Model of Responder-1 before MAS Treatment	82
Figure 55: Minimum Pressure (Pa) Value along Each UA Model (WO = Without MAS, W = with MAS)	84
Figure 56: Relationship between $\Delta\sqrt{\Delta P_{\text{Max}}}\%$ and $\Delta\text{AHI}\%$	85
Figure 57: Comparison of Wall Boundary of FSI and Experimental Models	89
Figure 58: Comparison of the Wall Displacement 50 mm from the Outlet between FSI and Experiment Results	90
Figure 59: Geometry Displacement of the UA Wall of Responder-1 (Left) before and (Right) after MAS Fitted, at Three Time Points During the Cycle	91
Figure 60: UA Wall Deformation of Responder-1 before Treatment at 0.0s, 0.3s and 0.56s	92
Figure 61: Velocity Vectors at the Longitudinal Cross-sections of UA of Responder-1 (a) before and (b) after MAS Fitted	94
Figure 62: Time Variation of Pressure Distribution along UA with (Top) Pre-treatment and (Bottom) Post-treatment Conditions	95
Figure 63: Velocity Vectors at the Longitudinal Cross-sections of UA of Failure-2 (a) before and (b) after MAS Fitted	97
Figure 64: Time Variation of Pressure Distribution along UA with (Top) Pre-treatment and (Bottom) Post-treatment Conditions	99
Figure 65: UA Wall Oscillation of Pre- (f-wo) and Post- (f-w) Treatment Failure Case	102

Figure 66: Velocity Vector Profile of Pre-treatment (without MAS).....	103
Figure 67: Velocity Vector Profile of Post-treatment (with MAS).....	104
Figure 68: Pressure Contours of Pre-treatment (without MAS)	105
Figure 69: Pressure Contours of Post-treatment (with MAS).....	105
Figure 70: Pressure Profiles of (a) Pre-treatment and (b) Post-treatment Models of Responder-1	107
Figure 71: Pressure Profiles of (a) Pre-treatment and (b) Post-treatment Models of Failure-2	108

List of Tables

Table 1: Respiratory Airflow Rate in Previous Studies	16
Table 2: General Characteristics of the Seven Patients in this Thesis (WO = without MAS, W = with MAS).....	30
Table 3: Summary of UA Geometrical Changes with MAS	68

Nomenclature

Abbreviations

2D	Two-dimensional
3D	Three-dimensional
ADC	Analog-digital Converter
AHI	Apnea-hypopnea Index
BMI	Body Mass Index
CFD	Computational Fluid Dynamics
CPAP	Continuous Positive Airway Pressure
CT	Computed Tomography
DNS	Direct Numerical Simulation
FE	Finite Element
FOV	Field of View
FSI	Fluid–Structure Interaction
LES	Large Eddy Simulation
LRN	Low Reynolds Number
LVDT	Linear Variable Differential Transformer
MAS	Mandibular Advancement Splint
MMA	Maxillomandibular Advancement
MRI	Magnetic Resonance Imaging
OSA	Obstructive Sleep Apnea
PSG	Polysomnography
RAN	Reynolds-averaged Navier–Stokes
SST	Shear Stress Transport
STL	Stereolithography
SLA	Stereolithography apparatus
UA	Upper Airway
UPPP	Uvulopalato-pharyngoplasty
US	United States

Numerical Terms

L	Litre
F_1	Blending functions 1
F_2	Blending functions 2
k- ϵ	k- ϵ turbulence model
k- ω	k- ω turbulence model
i, j, k	Cartesian coordinates
s	Second
t	Time
P	Fluid pressure
u	Flow velocity
ρ	Density
ϕ	Constant
ϕ_1	Constant for the original k- ω model
ϕ_2	Constant for the transferred k- ϵ model
φ_{ip}	Integration point value
φ_{up}	Value at the upwind node
\vec{r}	Vector from upwind node to the integration point
β	Blend factor varied from 0 to 1
v	Mean velocity
D	Hydraulic diameter
μ	Dynamic viscosity of the fluid
δ_{ij}	Kronecker delta
μ_t	Turbulent viscosity
k	Turbulent kinetic energy
σ_{ij}^f	Fluid domain stress tensor
σ_{ij}^s	Solid domain stress tensor
ϵ_{ij}	Rate of the strain tensor
\mathcal{E}_l	Transverse strain

\mathcal{E}_t	Longitudinal or axial strain
F_i	Body force
D_i	Structural displacement
E	Young's modulus
ν	Poisson's ratio
C_r	Courant number
Δl	Dimension of the grid
\bar{v}	Average linear velocity at that location
\dot{V}	Flow rate
$\Delta \text{AHI}\%$	Percentage change in AHI
$\Delta \text{CSArea}\%$	Percentage change in minimum cross-sectional area
Δt	Maximum time step size
ΔP_{Max}	Maximum pressure drop in UA
$\sqrt{\Delta P_{\text{Max}}}$	Square root of the maximum UA pressure drop
$\Delta \sqrt{\Delta P_{\text{Max}}}\%$	Percentage change in the square root of the maximum UA pressure drop

Chapter 1: Introduction

Apnea is defined as a suspension of breathing that lasts no fewer than 10 seconds. Hypopneas can be defined as 69% to 26% restriction of a normal breath flow, or a 4% or greater drop in the oxygen level in the blood [1]. Obstructive sleep apnea (OSA) syndrome is a common sleep disorder among both adults and children, which is characterised by recurrent episodes of apnea during sleep. Since the 1960s, there has been increasing evidence provided by clinical researchers that increased OSA can cause risk of highly adverse outcomes, such as extreme daytime fatigue and even cardiovascular disease [2]. In parallel, demographic studies have indicated that the population affected by OSA is immense [1, 3-6]. After clinical trials with significant time expense, certain types of surgery and conservative treatments have been implemented, such as continuous positive airway pressure (CPAP) and mandibular advancement splints (MAS). Some of these treatments are painful and cure rates are unsatisfactory. Thus, the mechanism of OSA must be better understood to improve existing treatments or develop more effective treatment methods. However, before beginning this investigation of OSA treatments, it is first worth discussing the background of OSA.

1.1 History of Obstructive Sleep Apnea

Early in 1966, Gastaut et al. [7] reported a type of sleep-induced breathing disorder in patients who had Pickwickian syndrome, and this discovery created a new era in sleep disorder research [8]. Gastaut et al. began observing this Pickwickian syndrome from a sleep perspective in 1965. A repetitive breathing cessation was recorded and reported, which drew the attention of clinical sleep and respiratory specialists. They changed their direction of investigation from patients with cardiorespiratory problems to patients with sleep disorders [7]. Duron et al., Lugaresi et al. and Kuhlo et al. [9-11] focused their research on sleep-induced intermittent respiration among non-obese patients. As clinical evidence similar to Gastaut et al.'s was found, this syndrome was widely accepted.

In 1972, the first symposium of sleep-related periodic breathing was held in Italy. By then, the concept of 'sleep-induced apnea' had emerged. The apnea syndrome was divided into three types: obstructive apnea that occurs when airways collapse, yet

1 respiratory effort continues; central apnea that occurs when there are functional
2 problems of the neurological feedback mechanism and respiratory effort is absent; and
3 mixed apnea, which occurs during the developing process from central apnea to
4 obstructive apnea [12].

5 **1.2 Consequences and Clinical Symptoms of Obstructive Sleep Apnea** 6 **Syndrome**

7 OSA patients' airway can be partially or completely collapsed. A frequent reduction of
8 ventilation in the airway can result in fragmented sleep, inadequate oxygen saturation,
9 and the increase of carbon dioxide in the blood. Further consequences can also
10 materialise, such as daytime fatigue and sleepiness, and lower concentration levels. If
11 the frequency of apnea reaches five times per hour, the patient may be in danger of
12 hypertension and atherosclerosis, which could eventually cause cardiovascular diseases,
13 such as coronary artery disease, stroke and congestive heart failure [13]. This largely
14 increases the mortality of patients aged 65 or more [6].

15 **1.3 Demographic Studies**

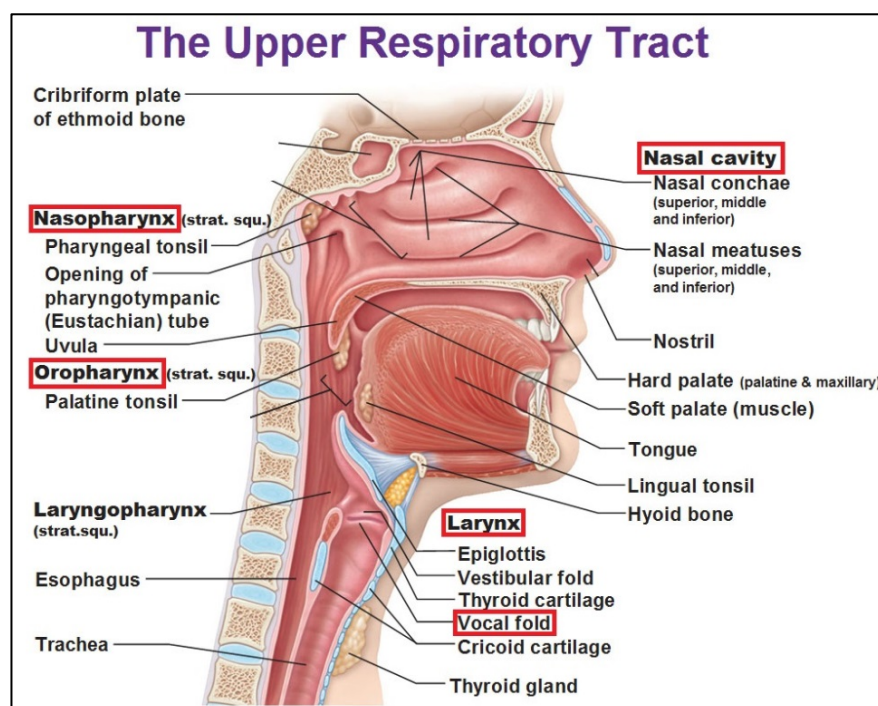
16 Young et al. [3] in 1993, first estimated an unexpected prevalence of mild to severe
17 OSA in middle-aged working adults, comprising 2% of women and 4% of men in North
18 America. Additionally, Ali et al. and Redline et al. [4, 5] reported that 2% of children
19 might be affected by OSA syndrome. Later, Young et al. in 2004, continued research on
20 adults' OSA risk factors, and found a large increase in occurrence of OSA in North
21 America. Almost 20% of adults had at least mild OSA and one-third had moderate to
22 severe OSA. The gender ratio of diagnosed OSA patient was 1:8 (female to male), with
23 nearly one in three males aged over 65 years suffering from OSA. Worse, more than 75%
24 of OSA cases that could receive medical treatment were remaining undiagnosed
25 because of low clinical recognition [14].

26 Another vital factor is the difference among varied ethnic groups, as the occurrence of
27 OSA may be a function of ethnicity due to its dependence on anatomical structure.
28 Researchers such as Redline et al., Coltman et al. and Cakirer et al. [15-17] proved this
29 hypothesis and found that the relationship between OSA and body mass index (BMI)
30 and other factors could be different for African-Americans, Caucasians and Polynesians.

1 However, BMI is always the strongest predictor. According to their conclusions,
2 Eastern-Asian countries should have fewer OSA sufferers because, on average, the
3 population has a low BMI. However, data show the opposite. In 2001, Ip et al. [18]
4 completed a demographic study of people with OSA in Hong Kong, which indicated
5 that 5% of the total population in Hong Kong could be considered OSA sufferers. It is
6 predicted that a similar situation exists in Mainland China, where at least 60 million
7 people suffer from OSA. In 2002, a more comprehensive demographic study was
8 undertaken that indicated a rapid increase in prevalence of OSA in the American,
9 European, Asian and Australian populations [19]. A following study in 2003 showed
10 that approximately 17% of adults have at least mild OSA in the United States (US) [20].
11 Given that OSA is so prevalent and has known health implications, better treatment
12 procedures are required.

13 **1.4 Anatomical Study of Human Upper Airway**

14 To ensure a better understanding of airway flow and collapse, it is essential to
15 understand the upper airway (UA) anatomy. As can be seen in the pharynx sagittal
16 section displayed in Figure 1, the UA is the region from the end of the nasal cavity to
17 the vocal cords. It connects the nasal cavity and oral cavity, and passes air into or out of
18 the trachea. This complex structure plays a critical role in respiratory activities.



19
20

Figure 1: Anatomy of the Human UA [21]

1 Anatomically, the UA can be divided into three segments: the nasopharynx, oropharynx
2 and hypopharynx. The hard palate and soft palate separate the UA and nasal region
3 from the oral cavity; however, they shape the velopharynx as a restricted region. The
4 oropharynx has the smallest cross-sectional area and throttles airflow from the nasal
5 airway. The majority of studies [22-25] insist that OSA could be associated with airway
6 occlusion in this area, rather than the narrower nasal cavity. However, some studies—
7 such as Schwab et al. [26] and Chouly et al. [27]—believe that the major airway
8 obstructions occur between the base of the tongue and soft tissue of the posterior airway
9 wall during expiration. The combination of both ideas above is found in the work of
10 Huynh et al. [28] and Hoffstein et al. [29], who suggested that there could be ‘multiple
11 sites’ of obstruction. Although opinions differ, previous results all indicate features of
12 the airway structure that directly predispose the UA to collapse. Compared with non-
13 patients, apnoeic patients normally have an enlarged and ‘retropositioned’ tongue,
14 extended soft palate, swelling on the palatine uvula and pharyngeal tonsils, an excessive
15 growing in the parapharyngeal fat pads, flabby tissue on the airway wall and a
16 retrognathic mandible or receding jaw [28]. These features can greatly shrink the UA,
17 complicate the airflow and result in increased airflow resistance.

18 **1.5 Risk Factors**

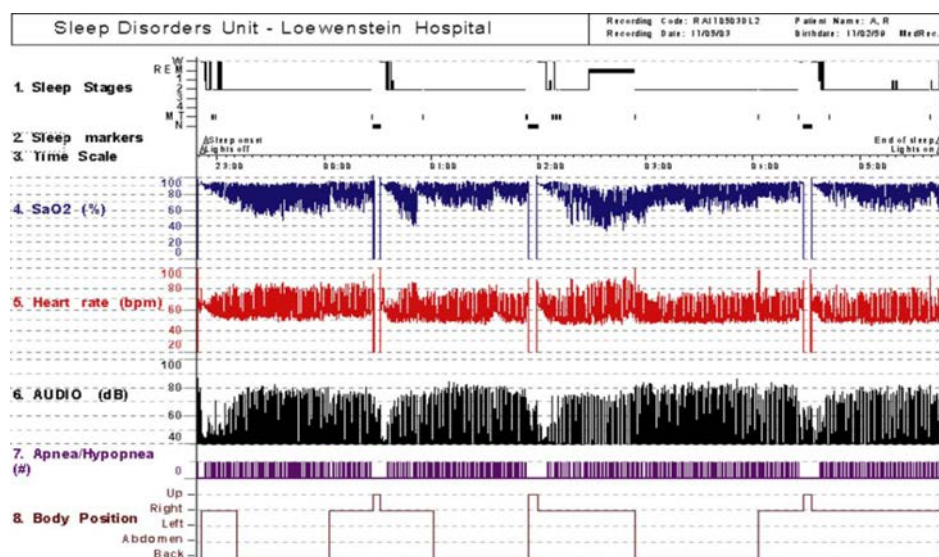
19 Obesity is the most influential factor contributing to OSA. Vgontzas et al. [30]
20 compared obese and non-obese OSA patients and found that the severity of OSA was
21 much greater for people with a higher BMI. Tangugsorn et al. [31] completed a
22 comprehensive cephalometric analysis (a study of the dental and skeletal relationships
23 in the head) and a high prevalence of OSA (of almost 50%) was found among morbidly
24 obese people. A similar result was attained in Rajala et al.’s earlier study [32].
25 Moreover, Busetto et al. [33] observed the severity of OSA to be alleviated through
26 weight loss, which meant less fatty tissue and a significant increase in the pharynx
27 cross-sectional area. Nevertheless, Young et al. clearly indicated that weight loss does
28 not always lead to OSA reduction. The increasing population of non-obese OSA
29 patients shows that people with normal weights can still have OSA. Thus, Yong et al.
30 [14] suggested classifying obesity as a ‘causal’ factor.

31 Smoking and alcohol are also believed to be common risk factors for OSA [14]. As a
32 result of smoking, the inflamed soft tissues narrow the pharynx. Excessive alcohol

1 consumption can deeply relax the muscles and lead to airway occlusion. Other factors—
2 such as respiratory depressing drugs, nasal congestion snoring and an increased neck
3 circumference—can all be direct factors in OSA [34, 35].

4 **1.6 Obstructive Sleep Apnea Diagnosing Methodologies and Medical** 5 **Treatments**

6 Full cardiorespiratory polysomnography (PSG) is the most common sleep study for
7 diagnosing sleep apnea. It involves a multi-parametric test through no less than 11
8 signal channels (22 wires) attached to the patient. Common parameters are brain signals
9 (electroencephalography), eye movements (electrooculography), muscle activation
10 (electromyography), heart rhythm (electrocardiography), airflow, chin movements and
11 oxygen saturation. During overnight monitoring and data collecting, a comprehensive
12 profile of patient's sleep conditions is saved (Figure 2) [36]. The frequency of apnea
13 and hypopnea (partly airway occlusion, such as snoring) are important parameters that
14 indicate the overall severity of OSA. Commonly, these two frequencies are combined
15 into a single factor—the apnea-hypopnea index (AHI). The AHI denotes the number of
16 apneas and hypopneas that occur per hour. It refers to three OSA severity levels: mild
17 (five to 15 events/hour), moderate (15 to 30 events/hour) and severe (> 30/events/hour)
18 [37].



19

20

Figure 2: A Regular PSG Record [36]

1 Different medical treatments are advised for each OSA severity level. CPAP method is
2 the most common nonsurgical treatment for moderate to severe OSA patients. In this
3 method, patients are required to wear a mask that connects to an air generator. This
4 adjusts the air pressure in the airway to keep it open and avoid collapse. Although
5 CPAP has a high efficiency in treatment, long-term compliance is poor because of low
6 acceptance among patients [38]. The main reason for this low acceptance is the
7 discomfort associated with wearing a mask during the night. Other side effects include a
8 dry or stuffy nose, irritated skin on the face, sore eyes and headaches. Some patients
9 who cannot tolerate CPAP switch to surgery.

10 Before the 1980s, tonsillectomy, adenoidectomy, nasal surgery and tracheostomy were
11 the main surgical treatments for OSA. Later, surgeries with higher effectiveness—such
12 as uvulopalatopharyngoplasty (UPPP) and maxillomandibular advancement (MMA)—
13 became available. UPPP is an operation to remove the uvula and part of the soft palate,
14 with an overall efficacy of 40.7%. However, risks such as internal bleeding and
15 infection can occur after the operation [39]. MMA is another highly efficient surgery for
16 severe OSA, which has a success rate of 97% [40]. This treatment surgically moves the
17 maxilla and mandible forward. The anterior pharyngeal tissues that attach to them can
18 also pull forward, which causes a considerable increase in the pharyngeal volume [41].
19 Facial changes are inevitable after MMA and patients usually experience pain and
20 swelling, and must consume a liquid diet for over one month. However, compared with
21 the lifelong suffering of CPAP, many patients still believe MMA surgery is worthwhile
22 [41].

23 In order to free patients from the torment of CPAP and surgeries, an alternative for mild
24 and moderate OSA sufferers is a conservative and non-invasive device called an MAS
25 (Figure 3). As an oral appliance therapy, MAS treatment requires patients to use a
26 custom-made frame in the mouth that protrudes the mandibular forward slightly. This
27 movement can prevent collapse of the airway during sleep. Despite relatively low
28 efficiency compared with CPAP, MAS is gaining popularity due to its user-friendliness
29 and fewer side effects [42].



1

2

Figure 3: A Custom-made MAS

3 PSG is used to indicate the AHI, while other methods are used to observe the anatomic
4 structure in the airway, with technologies such as computed tomography (CT) and
5 magnetic resonance imaging (MRI) the most common. CT uses x-rays for imaging,
6 while MRI creates an image via nuclear magnetisation and radio frequency detection.
7 MRI imaging largely relies on the different distribution of hydrogen in the human body.
8 Grover [43] compared the effectiveness of CT and MRI imaging for diseases in several
9 classifications. MRI was superior in detailing the soft tissues, while both methods had
10 almost equivalent results for bones. MRI consumed more time and required higher cost
11 than CT, yet had a lower radioactive hazard for patients. Overall, Grover suggested that
12 the use of CT or MRI really depends on the situation. Generally, MRI is a better choice
13 in airway imaging due to having a better response with soft tissues.

14 Medical scientists previously argued that the progress of developing OSA treatment has
15 been limited by a lack of understanding of fluid flow effects on the human UA anatomy
16 [8, 44]. This requirement was quickly responded to by numerous physical and
17 numerical fluid dynamic studies that aimed to trace the correlation between the human
18 UA structure and airflow pattern. Advanced modelling methodologies were used to
19 reproduce the UA structure and respiratory airflow. However, until now, the
20 mechanisms of OSA pathogenesis remain unclear [8].

21 **1.7 Aim of this Thesis**

22 The aim of this research is to reveal the influence of fluid dynamics in the UA on the
23 mechanism of OSA by modelling UA collapse, and to indicate a possible solution to
24 predict the treatment response of the MAS treatment. This research hypothesises that

1 there are relationships between the UA flow characteristics and AHI changes before and
2 after MAS treatment. In addition, by modelling the UA wall movement, this thesis aims
3 to quantify the improvement on the UA structure achieved by MAS.

4 **1.8 Structure of the Thesis**

5 The next chapter will discuss previous literature that presented studies on the
6 computational modelling of OSA. By assessing previous studies, this research is able to
7 develop an appropriate methodology to model the UA flow and UA wall movement
8 regarding OSA. Chapter 3 will present a multiple case study of OSA respiratory flow by
9 using computational fluid dynamics. It will also demonstrate a possible predicting
10 method of MAS treatment by using a model of AHI–UA pressure correlation. Chapter 4
11 will model the UA wall movement together with the UA flow under the FSI method. It
12 will also reproduce the collapse of the UA wall in computational modelling. The final
13 chapter will conclude this thesis and discuss the possibility of applying this study’s
14 computational modelling method in the clinical routine of MAS treatment.

15

Chapter 2: Literature Review

2.1 Introduction

This section is a review of previous OSA syndrome studies from a CFD perspective. This review will detail previous CFD technology associated with OSA cases, and discuss related experimental validating processes to indicate the competency of CFD analysis. Computational FSI is anticipated to be a possible methodology to model UA occlusion to explain the mechanism of OSA pathology.

2.2 Computational Fluid Dynamics Simulation

Before using CFD, research into OSA syndrome was limited to statistical studies and clinical trials [40, 45, 46]. However, the mechanism of OSA could not be fully understood without knowledge of flow dynamics. Thus, during the last decade, CFD analysis was introduced to model UA flow, which gave the ability to theoretically explain OSA.

2.2.1 Modelling and 3D Reconstruction of Human UA

In the early stage of the UA computational modelling, only simplified UA geometries were available for performing CFD. Yu et al. [47] established their CFD model based on a 1:1 scale medical school teaching model (Figure 4).

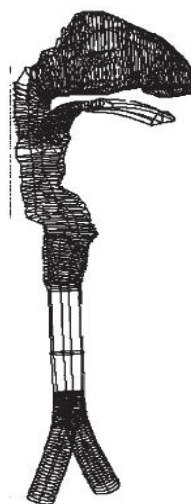
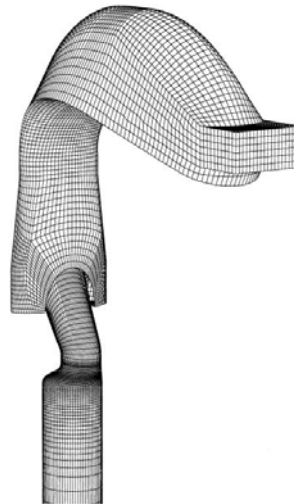


Figure 4: 1:1 Scale Human UA Medical School Teaching Model [48]

1 The UA model was made of silicone rubber and then scanned using CT. The UA flow
2 was defined as 15 L/min to match an adult’s sedentary breath. A similar yet more
3 detailed study was undertaken by Martonen et al. [48]. The UA flow conditions of ‘a
4 peaceful breath’ and ‘in light physical activities’ were modelled using different flow
5 rates. As expected, the results of these two studies were very close. Although the
6 rationality of their modelling method was unproven, Yu et al. and Martonen et al. [47,
7 48] demonstrated the possibility of using CFD to model UA flow. Later, in 2003,
8 Heenan et al. [49] completed a CFD simulation based on an idealised human
9 oropharynx model named ‘Weibel A’ (Figure 5). Weibel A was designed by averaging
10 the geometries of a large number of airway casts. However, Heenan et al. explained that
11 this model withheld all the basic anatomical features of a realistic airway geometry, so
12 was still unable to accurately capture the complex flow details of realistic UA flow.



13
14

Figure 5: The ‘Weibel A’ Idealised Human UA Model [49]

15 Collins et al. [50] compared flow profiles in Weibel A and a geometrically accurate UA
16 model by running three-dimensional (3D) CFD analysis. The realistic model was
17 sourced from MRI images of a typical 21-year-old male student. The comparison
18 indicated that the two flow structures were not similar. There were a great number of
19 flow recirculating regions appearing in the Weibel A model, while the realistic model
20 had a smooth flow pattern with less turbulence. In addition, a significant larynx jet
21 observed in Weibel A was absent in the realistic model. Collins et al. explained that, in
22 Weibel A, recirculation flows were generated by sharp edges or steps in the geometry.
23 When flow passed a sharp object, such as the epiglottis, in the model, the boundary
24 layer flow would encounter a flow field with increasing pressure—referred to as

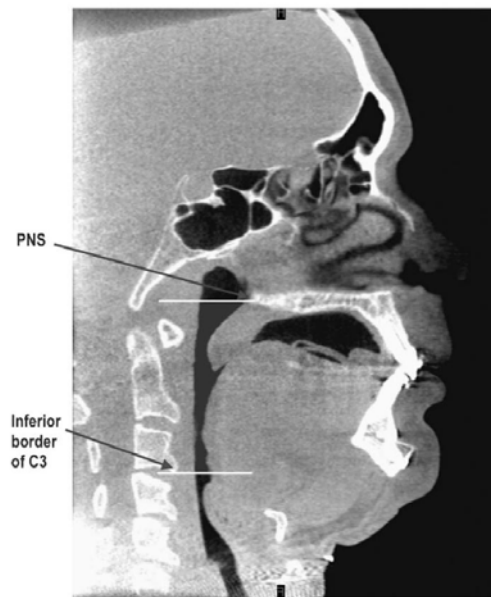
1 'adverse pressure'. As such, the velocity gradient of the boundary layer flow was
2 reduced by the adverse pressure gradient. The boundary layer flow would leave the
3 model surface once the velocity gradient at the wall reduced to zero and, in this
4 circumstance, flow separation occurred. This flow separation would occur from a low-
5 pressure region with vortex and backward flow—also called 'flow recirculation'. The
6 larynx jet was formed at the restricted region around the epiglottis. The sudden
7 expansion or contraction of the airway cross-sectional area raised the pressure gradient
8 and induced the jet flow and flow separation. In comparison, the smooth-curved
9 structure in the MRI geometry helped the airflow attach to the wall; thus, flow
10 separation and recirculation were prevented. Thus, the flow structure in the idealised
11 UA failed to predict correct UA flow.

12 In recent studies of UA flow, anatomically correct UA models were commonly used.
13 These geometries were reconstructed based on 3D MRI or CT data. Xu et al. [51]
14 modelled three cases of children aged three to five years old, who had an AHI from 1.8
15 to 7.4. The MRI data had a resolution of 192×256 pixels with a 200×240 mm field of
16 view (FOV). 3DVIEWNIX software was used to align MRI slices, with manual
17 selection of airway pixels and semi-automatic mask connection. A fuzzy geometry of
18 the UA was generated and then imported into Amira 3.0 for the smoothing process. The
19 applied smoothing algorithm transferred the small facets into large continuous
20 surfaces—otherwise, the raw model would be too complicated for meshing and flow
21 simulation. It is also worth noting that some important details of actual UA geometry
22 were removed through geometry smoothing, particularly for the complex nasal cavity
23 and velopharynx structure.

24 In most of the UA CFD modelling studies using MRI data, the oral pharynx and nasal
25 cavity were excluded on the UA model—not only because of the difficulty in clearly
26 defining the wall boundary, but also because these regions were believed to have less
27 effect on UA flow features. In the study by Collins et al. [51], four sets of MRI scans
28 with different image resolutions were used in CFD modelling. The scan with the highest
29 resolution had a pixel size of 1.17 mm, which was similar to the scan quality in the
30 study by Xu et al (1.07 mm). However, Collins et al. [50] found that the MRI
31 resolutions of all investigated scans were insufficient to identify the nasal and oral

1 cavities. Thus, only half of the nasal passages were able to be reconstructed and the oral
2 cavities and sinuses were neglected.

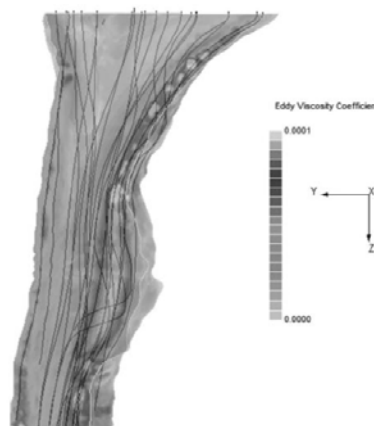
3 Huynh et al. [28] attempted to use pharyngeal flow features to evaluate the treatment
4 response of MMA surgery. The inlet and discharge boundaries of UA were defined
5 from the posterior nasal spine to the third cervical vertebra (Figure 6).



6

7 **Figure 6: Defined Boundaries for the Pharynx in the Study by Huynh et al. [28]**

8 An inspiratory flow was defined as 340 to 460 ml/s uniform airflow at the posterior
9 nasal spine. The outlet boundary had a static pressure of 0 Pa. Figure 7 shows the
10 velocity streamlines. The airflow was found to have a large velocity at the anterior wall
11 of the pharynx, which resulted in an increased turbulence of flow around the oral cavity.

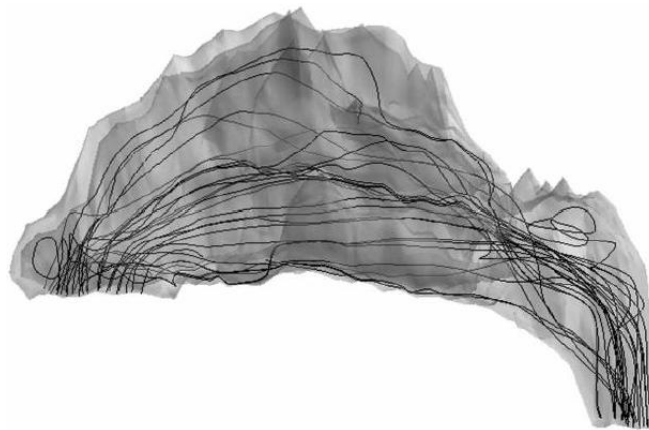


12

13

Figure 7: Velocity Streamlines in the Pharynx Model [28]

1 Schroeter et al. [52] analysed the inspiration airflow in the nasal cavity by using a 3D
2 MRI model. The geometry was defined from the nostril to the nasopharynx. According
3 to the results shown as velocity streamlines (Figure 8), inlet airflow was dispersed into
4 several flow streams in the nasal cavity, and then merged back at the posterior wall of
5 the pharynx. The main stream of the nasal airflow travelled in an approximately
6 horizontal direction. The geometry of the nasal pharynx anatomy forced the flow to
7 change directions, attach to the posterior wall of velopharynx and travel down to the
8 oropharynx.



9

10

Figure 8: Velocity Streamline in the Nasal Model [52]

11 More complex geometrical details can be found in studies that used CT data, as the scan
12 resolution is normally higher than MRI. Vos et al. [23] created a 3D airway model for
13 CFD simulation under a set of high-definition 3D CT images with a resolution of 0.4
14 mm pixels. The inter-slice distance was 0.5 mm. Mimics (version 9.1) was used for
15 image post-processing. The Hounsfield (a value of radio-density for different substances)
16 values for air and bone were defined as -1,024 and 1,000, respectively. The study
17 suggested using a volume compensation algorithm after surface smoothing, which
18 allowed the model to have continuous surfaces while preserving most of the realistic
19 geometry details.

20 Wang at al. [25] undertook a study of pharyngeal flow in a complete UA geometry. This
21 study used anatomically-accurate nasal and pharynx models with idealised larynx and
22 trachea models to perform inspiratory flow analysis (Figure 9). The velocity cross-
23 sectional contours indicated that the airflow was concentrated along the back wall of the
24 velopharynx and oropharynx, while a pharynx jet was also found at the posterior
25 pharyngeal airway.

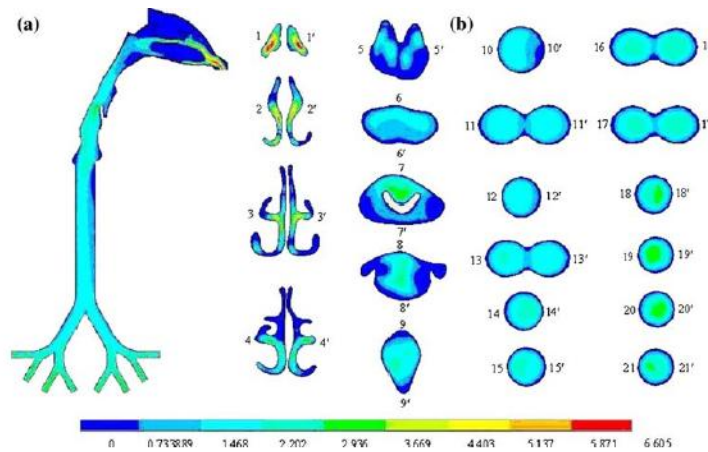


Figure 9: Velocity Streamline in Pharynx Model [25]

Above all, CT scans or high-definition MRI have the advantage of showing a clearer UA boundary, which enables reconstruction of a complete UA geometry. However, the high-definition scan increases the level of radioactive exposure to patients, while a significant effort is required to accurately calculate the flow in the nasal cavity. However, there is no evidence that indicating the nasal cavity can significantly vary the pharyngeal flow parameters, such as minimum pressure or maximum velocity. If the nasal cavity is excluded in the model, the inlet flow profile at the nasopharynx should be assumed. In this thesis, the result show that an absent nasal cavity will not significantly vary the maximum pressure drop and flow velocity profiles in the UA. This finding aligns with the study by Persak et al. [53].

2.2.2 Meshing by Using Commercial Programs

Based on a review of over 20 CFD studies on UA flow, meshing methods and mesh quality can vary. Commercial meshing tools such as ANSYS ICEM, TGrid and Gambit are generally the first choice to mesh the UA geometry. Some medical image-processing programs—such as Amira, scan IP and Mimics—also provide basic meshing functions. Yu et al. [47] used Amira to generate volumetric elements in UA geometry. The surface mesh was converted from the faceted feature of the UA surface, and then the unstructured tetrahedral volume-element was automatically generated in UA lumen. There are very few meshing-control settings available in medical image-processing programs. The simple and only solution to increase the accuracy of the simulation is to increase the grid quantity in the computational models. Other control methods of grid quality—such as uniformity, aspect ratio and skewness—are not available. As a result,

1 the generated mesh is very high in grid density, which increases the computational
2 expanse, yet is unable to accurately predict the complex UA flow structure.

3 The structured hexahedral element has the advantage of computational efficiency. As it
4 is based on Cartesian grid geometry, the nodes can be easily identified and accessed.
5 Structured grids are found mostly in CFD studies of regular shape fluid domains. As
6 shown in Figure 5, a well-presented structured hexahedral volume mesh was created
7 based on the Weibel A model. Most meshing tools have no algorithm to create a
8 structured mesh on irregular geometries, such as the UA. The ANSYS ICEM provides a
9 ‘block’ function that can cut the geometry with Cartesian planes; however, a large effort
10 is required for grid refinement and, even so, the grid along the UA wall boundary is
11 highly distorted. The unstructured mesh can perfectly fit to irregular geometries.
12 Therefore, the tetrahedral mesh has been widely adopted in UA CFD studies. There are
13 also algorithms available for automatic grid refining. A cell adaptation technique was
14 adopted in the work of Wen et al. [54], which was able to split the oversized elements
15 and refine the near-wall elements. Jeong et al. [22] used an inflation function to create
16 two layers of elements at the inlet boundary to increase the stability in calculation.

17 **2.2.3 Boundary Conditions**

18 Boundary conditions in UA CFD modelling should be defined to mimic the human
19 respiratory flow condition. The UA inspiratory flow comes from the nasal cavity and
20 exits at the trachea. Ideally, ambient static pressure should be defined at the nostrils and,
21 correspondingly, discharge airflow defined at the lower larynx. By reviewing previous
22 studies, various definitions of human inspiratory airflow rate were attained (Table 1).
23 Some studies specified a time-dependent flow to mimic the respiratory cycle, while
24 others defined a mean airflow rate. All the presented values in Table 1 are the mean
25 flow rates, which show a wide data range of 133 ml/s to 1,000 ml/s.

26

1

Table 1: Respiratory Airflow Rate in Previous Studies

Author	Year	Defined respiratory airflow rate	Airflow rate by ml/s	Evidence
Martonen et al.	2002	17–34 L/min	283–566	Based on human subject Inhalation exposures in other papers
Xu et al.	2006	$(0.019 \cdot \text{age} + 0.014)$ L/s (for child)	204 (age = 10)	Based on literature of infant respiratory functions
Yu et al.	2009	500 ml/3.75s	133	Assumed
Wang et al.	2009	400–600 ml/3s	133–200	Based on literature of biomechanics textbook
Collins et al.	2007	1 L/s	1,000	Based on lung expansion measurement in other papers
Hopkins et al.	2000	125 ml/s for both nasal airway	250	Assumed
Kim et al.	2004	125 ml/s for both nasal airway	250	Assumed
Sun et al.	2007	500 ml/3s	166	Based on literature of biomechanics textbook
Chouly et al.	2006	10 L/min	166	From other researcher's PSG study
Sittivornwong et al.	2009	5–7 mL/kg/second	400–560 (weight = 80 kg)	From medical text book

- 2 1. Defined respiratory airflow rates are the figure or expressions given by authors.
- 3 2. Airflow rate by ml/s means the mean respiratory airflow per one second.
- 4 3. Evidence refers to the sources of these airflow figures.

5 It is unsurprising that there is large variety among these figures, as they were obtained
6 via different methods. None of these studies used patient-specified respiratory flow data
7 and the key flow parameters—such as velocity, pressure drop and shear force—are
8 connect to flow rates, which vary among patients. The assumed UA flow rate may lead
9 to mistakes in predicting patient-specific flow features however this thesis will
10 introduce a useful method to avoid the defects of using assumed flow rate. Other
11 boundary conditions were standard settings for all the reviewed studies, such as a
12 smooth and non-slip wall and 5% turbulence intensity of inlet flow.

13 **2.2.4 Turbulence Modelling of UA Flow**

14 In early UA CFD studies, UA flow was believed to be laminar. For example, Martonen
15 et al. [48] chose the laminar flow regime to calculate the Re from velocity

1 measurements at different parts of the airway. A Reynolds number of 1,200 was
2 calculated at the trachea based on inhalation flow rate and an averaged trachea diameter.
3 The experimental results from Hahn et al., Schroter et al. and Zhao et al. [55-57]
4 indicated that the flow in the nasal cavity and tracheobronchial airways was also
5 predominantly laminar under quiet breathing conditions. Hirtum et al. [58] compared
6 experimental and numerical data that indicated the UA to be in the transitional flow
7 regime. It was later indicated by Chouly et al. [27] that a laminar regime approximation
8 was still considered to be most appropriate.

9 In recent studies, evidence shows that the UA flow associated with an OSA occlusion is
10 in the transitional regime. De Backer et al. [59] found that, in OSA cases, the narrowed
11 UA could raise the Reynolds number to 6,000. A transitional regime should be more
12 precise than the assumption of laminar flow at these regions. For a solution of
13 transitional flow, Reynolds-averaged Navier–Stokes (RAN) equations may be sufficient,
14 despite being simple. Collins et al. [50] agreed with De Backer et al. and indicated that a
15 two-equation $k-\omega$ turbulence model with transition-specific, low Reynolds number
16 (LRN) modifications could potentially cope well with the transitional UA flow. Later,
17 Jeong et al. [22] introduced the LRN $k-\epsilon$ model to OSA CFD modelling. This model
18 was then compared with the standard $k-\epsilon$ model, large eddy simulation (LES) and
19 experimental results. Due to the absence of data in a geometrically-correct physical
20 airway model, the experiment was implemented in an axisymmetric tube with a
21 sinusoidal construction. This tube was believed to be geometrically similar to the
22 pharynx structure, and believed to be able to produce transitional flow. Comparing the
23 velocity profiles around the centreline, LRN $k-\epsilon$ obtained a better result than the other
24 two results. Another group of figures depicted that LRN $k-\epsilon$ could precisely represent
25 the physical turbulence intensity. As a result, Jeong et al. [22] believed LRN $k-\epsilon$ could
26 be the best turbulence model for transitional flow. However, the grid number they
27 constructed in this axisymmetric tube CFD model was only 360,000, which may be
28 insufficient for a standard LES simulation. The 12 channels along the centreline for data
29 acquisition were insufficient to capture the complete flow profile, which may be one of
30 the reasons that there was a significantly large divergence between the experimental and
31 LES results.

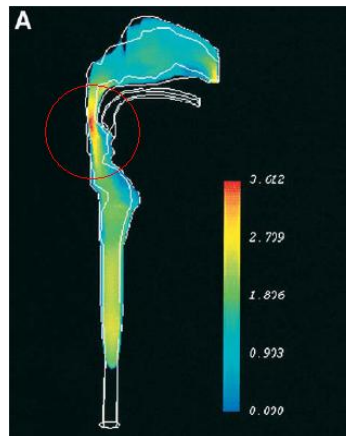
1 Recently, in 2009, Mylavarapu et al. [60] demonstrated a comparison study of five
2 different turbulence models (LES, $k-\epsilon$, $k-\omega$, $k-\omega$ shear stress transport [SST] and one-
3 equation Spalart–Allmaras model) with experimental results on a patient-specific UA
4 model. They used 16-channel pressure monitoring ports along the length of the model,
5 four of which were placed at Cartesian directions of the velopharynx to better observe
6 flow distribution in the UA cross-sectional area. The results indicated that the $k-\omega$
7 model obtained the closest result to the experimental data. The standard $k-\epsilon$ model over-
8 predicted the wall pressure at almost all positions, while the situation was opposite in
9 the LES, SST and Spalart–Allmaras models. Similar results were found at the
10 oropharynx cross-sectional area. The one-equation Spalart–Allmaras model largely
11 under-predicted the value, while LES, $k-\epsilon$ and SST overall had a 30% error in
12 comparison with the experimental data. The standard $k-\omega$ model maintained an overall
13 10% difference to experimental results, and was subsequently considered the best
14 turbulence model in this case. The LES and SST models should have a higher accuracy
15 than the other methods. Mylavarapu et al. [60] explained this discrepancy based on the
16 low resolution of the grid near the boundaries for SST and the relatively coarse grid for
17 LES inducing the error.

18 In engineering modelling studies, the current convention for transitional flow is mainly
19 unsteady LES and direct numerical simulation (DNS) methods [70-77]. The high-order
20 accuracy in LES and DNS requires higher mesh quality and higher computing expense.
21 It can be conjectured that an anatomically-correct model is sufficiently complex to
22 result in a high computational load. Thus, creating a high-quality grid mesh to
23 implement DNS and LES methods on this complex model seemed impractical and
24 unnecessary for the purpose of the current OSA modelling study. Rather, more practical
25 methods should be employed for clinical usage, where information is required quickly.

26 **2.2.5 Similarities of the Findings in UA Flow Modelling**

27 The velocity profile of a large number of studies demonstrated a fast air stream at the
28 smallest cross-sectional area in the velopharynx. This flow feature was identified as the
29 ‘pharyngeal jet’ (Figure 10) [22, 47, 48, 50, 59, 60]. Sun et al. and Wang et al. observed
30 a less strong jet flow in the velopharynx than in the nasopharynx [24, 25]. Collins et al.
31 [50] could only find this jet flow feature in the idealised UA model, rather than the
32 anatomically-accurate model. Thus, it can be concluded that interpersonal difference in

1 UA anatomy is significantly large to generate different UA flow patterns.



2

3

Figure 10: Typical Pharynx Jet in Simulation Results [48]

4 A couple of studies compared the flow profiles for both inhale and exhale conditions
5 [25, 47, 50, 51, 61]. An averaged 30% greater pressure loss and higher flow velocity
6 were observed in inspiration compared with expiration. This referred to a UA flow with
7 higher turbulent kinetic energy and lower total pressure, which increased the possibility
8 of UA collapse. It is also worth mentioning that the simplified oral cavity in most of the
9 studies could vary the flow feature in the oropharynx. The oral cavity was excluded
10 from the airway flow region, which could change the flow patterns in the oropharynx—
11 a region with high risk in occlusion. In summary, the common finding of all these
12 previous studies was that narrowing in the UA increased the regional flow velocity and
13 reduced the local pressure. This low-pressure feature might be related to the severity of
14 OSA, since a high-pressure gradient across the wall boundary would collapse the UA
15 structure.

16 **2.3 Experimental Validation**

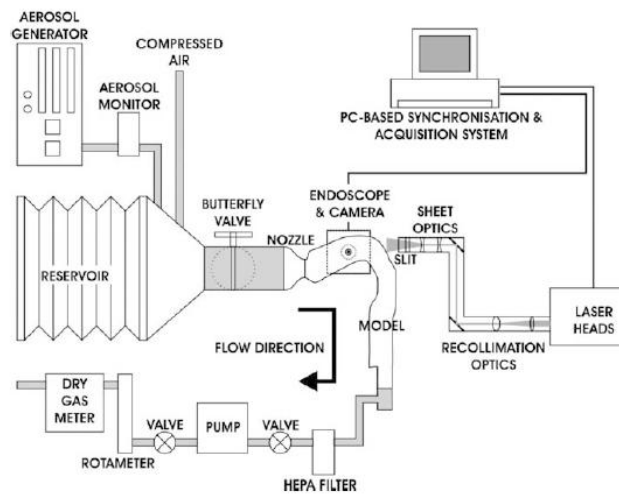
17 There is limited information in previous studies about in-vivo measurements of UA
18 airflow. Instead, a physical model of the UA is normally fabricated to experimentally
19 validate the CFD methods. The key point of the current experiment is to correctly
20 imitate the physiological characteristics of UA flow.

21 **2.3.1 Simple Physical UA Models in an Early Stage of UA modelling**

22 In 2003, Heenan et al. [49] modified the Weibel A model to be a 2:1 scale of real UA
23 geometry for experimental measurements. Two halves of a 3D UA computer model

1 were created using Pro-Engineer and Desk Artes 3 Data Expert software. Slots were
2 punched for laser devices, and appendages were added to bind the two halves of the UA
3 model, which were produced with a Stratasys FDM 8000 rapid prototyping system. The
4 material was ABS plastic. Figure 11 demonstrates the experiment setup of Heenan et al.
5 They indicated that the double-sized model could be easier to set up the measuring
6 equipment. To obtain the same flow conditions (same Re) in the CFD analysis, the
7 volumetric flow rates were also doubled.

8 The study indicated that CFD might over-predict the flow recirculation, since the
9 diameters of the eddies found in the CFD result were significantly larger than that in the
10 experiment. In addition, the flow velocities in the physical model were more sensitive to
11 changes in the inlet flow rate than they were in the CFD. Heenan et al. [49] explained
12 that these discrepancies were due to the physical model, oversimplified boundary
13 conditions and an insufficient turbulence model in the CFD analysis. Even very small
14 leakage on the model could change the flow pattern.



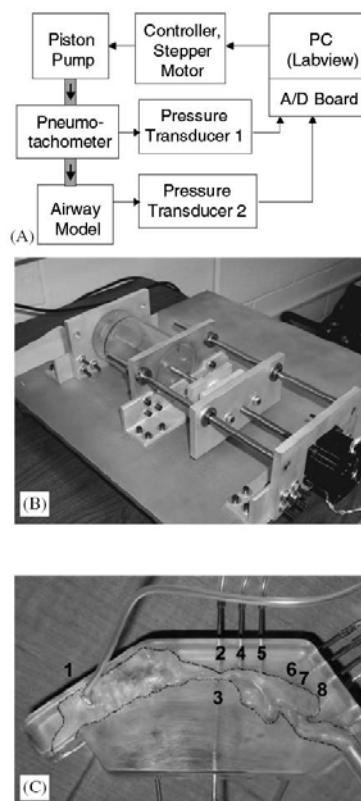
15

16 **Figure 11: Physical Respiratory Experiment Setup by Heenan et al. [45]**

17 **2.3.2 Geometrically-accurate UA Models**

18 Xu et al. [51] built a patient-specific 85% scaled model to validate their CFD results
19 (Figure 12). This model was based on a 3D reconstruction of MRI scans. A
20 stereolithography (STL) file was exported from Amira to Pro-Engineer for modelling,
21 which was designed as subtracting the airway geometry from a rigid block (Figure12-C).
22 The model was then manufactured using rapid prototyping method. Figure 12-A
23 presents the experiment procedure of Xu et al., with eight pressure taps placed along the

1 back of the model to capture the static pressure. The flow was generated from a
 2 digitally-controlled air pump that could produce a pulsatile airflow. Additionally, this
 3 inlet flow was monitored by a pneumotachometer. A pair of low-pressured transducers
 4 (DP45-14, Validyne) could capture pressure values in those pressure taps and the
 5 pneumotachometer. All analog signals were transferred into digital data for further
 6 computer processing. The physical UA model had a scale of only 85% of the real
 7 airway geometry. Therefore, the inlet flow rate was reduced to maintain the same
 8 Reynolds number as in the CFD analysis ($Re = 970$). However, the reason for using this
 9 downsizing-scaled model was not mentioned. The results showed that the pressure
 10 results could be matched with an averaged difference of 2 Pa. However, the maximum
 11 pressure drop that CFD predicted was 20 Pa higher than the experiment. An interesting
 12 finding was that both the simulation and experiment results indicated the possibility that
 13 there was not enough effort for the pharynx to remain open during expiration. The flow
 14 from the narrowed pharynx diffused quickly to the nasal cavity, and resulted in a
 15 significant negative pressure in oropharynx, which could drive the base of tongue to
 16 collapse to the posterior UA wall [51].

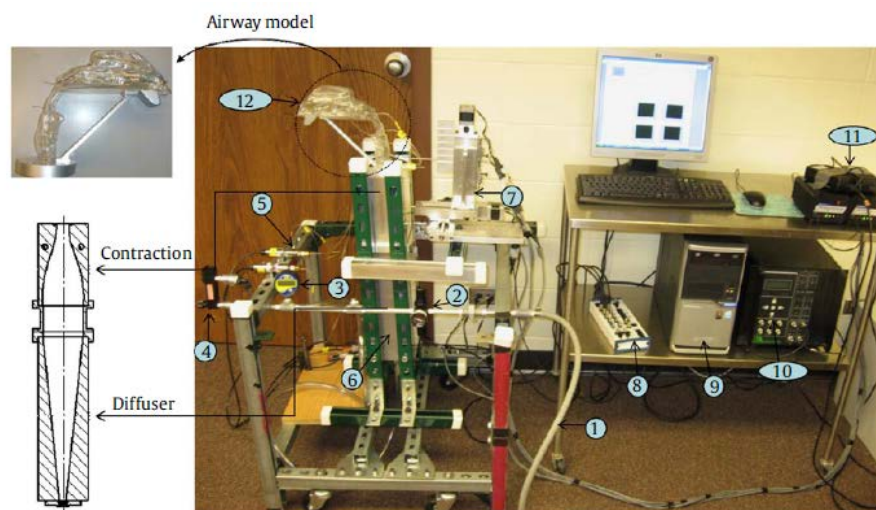


17

18 **Figure 12: Experiment Procedure and Equipment of Xu et al. [51]**

19 Later, in 2009, Mylavarapu et al. [60] performed an experiment of expiratory flow with

1 an anatomically-accurate model. They fabricated a thin-wall UA model with a
 2 uniformed thickness (Figure 13), and connected a flow conditioner to the inlet of the
 3 model. This flow conditioner had a six-degree diffuser and smooth nozzle with an area
 4 reduction of 12 to 1. It was designed to eliminate turbulence, while producing a laminar
 5 inlet flow to the UA model. Four pressure taps were set in the anterior-posterior and
 6 lateral directions at the velopharynx. The cross-sectional distribution of pressure could
 7 be plotted. A comparison of wall static pressure was attained between the experiment
 8 and CFD results by using a different turbulence model. The wall static pressure result of
 9 the RAN $k-\omega$ model obtained the closest match to the experimental result, with a
 10 maximum discrepancy of 10%. However, all the turbulence models failed to predict the
 11 flow pressure at the oropharynx. The complex structure in the oropharynx induced an
 12 unsteady flow separation. The time-averaged algorithms of the $k-\omega$ model could not
 13 capture the complete flow details [60].



Experimental setup for pressure and velocity measurements in the airway model. (1) Air Supply; (2) Pressure Regulator; (3) Digital Pressure meter; (4) Flow meter with control valve; (5) Pressure transducers; (6) Diffuser & Contraction Assembly; (7) Traverse; (8) NI DAQ board; (9) Computer; (10) Anemometry System; (11) Traverse motor controller; (12) Airway model.

14

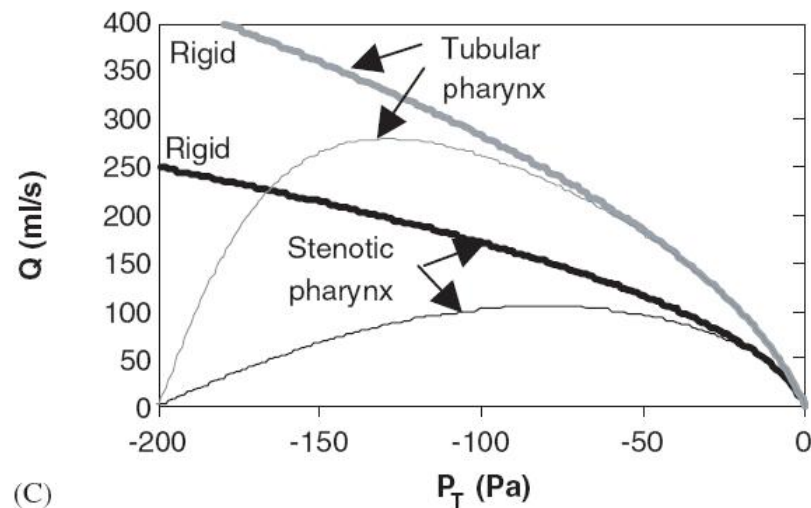
15

Figure 13: Experiment in Mylavarapu et al.'s Validation Process [60]

16 The above studies indicated that the RAN turbulence models generally performed well
 17 in solving the UA flow. However, the assumptions made in RANS result in an over-
 18 prediction of flow turbulence at the velopharynx and oropharynx, and these regions are
 19 dominated by transitional flows. Thus, if possible, it would be ideal to employ a hybrid
 20 solver that uses a high-accuracy model (DNS or LES) at important regions and low-
 21 accuracy model (RANS) at less vital regions.

1 2.4 Fluid–structure Interaction

2 In 2006, Xu et al. [51] indicated the possibility that UA flow could be affected by the
3 low pressure–induced pharynx narrowing. This phenomenon is a cycle that eventually
4 leads to UA occlusion. Xu et al. proved this assumption by using a mathematical model
5 (Figure 14). When considering wall deformation, pressure drop and flow rate will have
6 nonlinear relationship. The flow rate can decrease to zero if the pressure drop is large
7 enough. A sufficiently reduced cross-sectional area can limit the flow rate, yet increase
8 flow velocity, which reduces the pressure. The obstruction of UA will be driven by this
9 low pharyngeal pressure.



10
11 **Figure 14: Deformable Wall Effects Indicated by Xu et al. [51]**

12 Jeong et al. and Wang et al. [22, 54] referred to the assumption of Xu et al., yet
13 indicated that UA flow and wall movement could be simulated in the recently
14 introduced method of FSI. FSI is normally applied to solve the situation in which the
15 deformable or removable geometry interacts with the flow. Particularly for problems
16 related to oscillation, FSI is an effective method to analyse the robustness of the
17 structure and its material within flow effects. It is possible to introduce FSI to solve UA
18 occlusion if both the fluid domain and structural domain are available for numerical
19 modelling. The literature indicates that FSI study for UA is still in a very early stage.

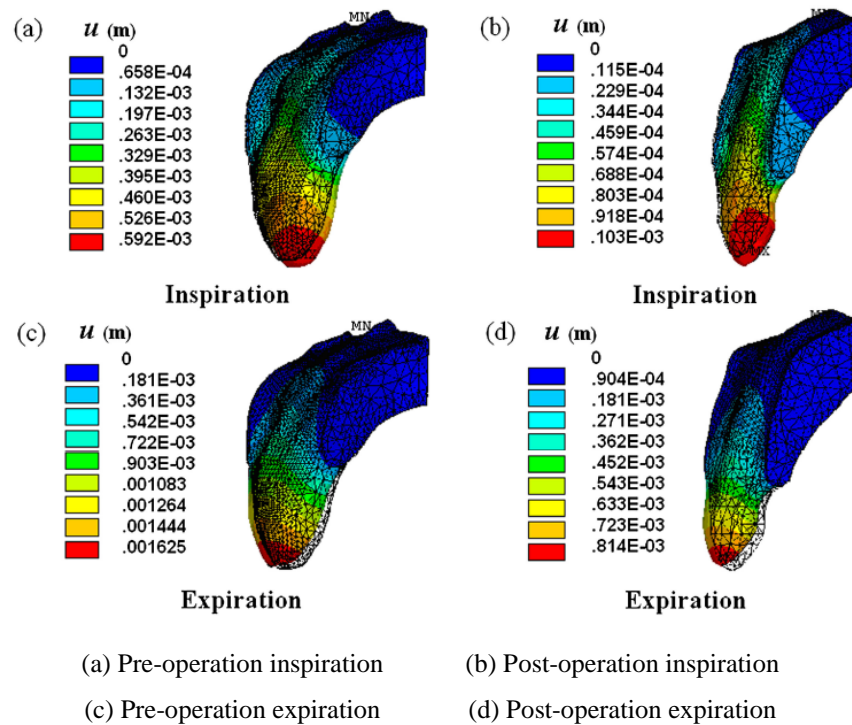
20 In 2006, Chouly et al. [27] performed an FSI study of two pre- and post-surgery OSA
21 patients by using a two-dimensional (2D) tongue model. The aim of the study was to
22 develop a low computational cost FSI method to predict the outcome of MMA surgery

1 for clinical applications. Using a desktop computer, the target simulation time was
2 within one hour. The geometry of the tongue was obtained from sagittal radiographies
3 before and after surgery. The posterior pharynx wall was assumed to be a straight and
4 rigid wall. Chouly et al. believed that a quasi-steady model was appropriate to describe
5 the tongue occlusion. The tissue of the tongue was considered a homogeneous, isotropic
6 and linear material, while the flow was assumed to be incompressible, laminar and
7 stationary in this case. A 2D finite element (FE) method was applied to solve the
8 structure deforming. The displacement of nodes was determined by nodal forces and a
9 stiffness matrix. In the solver for fluid domain, the Navier–Stokes/Prandtl equations
10 were used. The UA tissue was assumed to have a Young’s modulus of 6 kPa, with a
11 Poisson’s ratio of 0.499. The UA wall tissue was defined with a density of $1,000 \text{ kg.m}^{-3}$,
12 which was based on the consideration that there was a large proportion of water in the
13 tissue. The simulation could be finished within 20 minutes on a regular PC. The results
14 of the pre-surgical model successfully depicted a collapsed tongue structure. The UA
15 pressure drop was 300 Pa, and the flow restriction on the post-surgical model was
16 greatly alleviated by the airway enlargement. The flow-induced deformation was
17 reported as minimal. Thus, this study indicated the possibility of applying FSI analysis
18 in daily clinical usage. Later, in 2008, Chouly et al. [62] upgraded the previous 2D
19 model into a 3D cylinder-like tongue model. Good agreement was achieved between the
20 FSI and experimental results; however, the tongue geometry was too simple and could
21 not reproduce the complex 3D UA flow in a real situation.

22 In 2007, a 3D FSI study of soft palate displacement was undertaken by Sun et al. [24].
23 This study employed a geometrically-correct UA model with more realistic boundary
24 conditions. The UA volume consisted of the nasal cavity and velopharynx. The soft
25 palate was the only non-rigid part of the model. The results indicated a large
26 deformation of the soft palate, particularly uvula movement, in OSA patients. The
27 deformation induced a higher flow velocity and lower flow pressure around the soft
28 palate; however, occlusion of the airway did not occur. This study was limited by
29 assuming the UA wall tissue to be rigid; thus, the results could change if the tongue or
30 posterior wall was modelled to be flexible.

31 In 2012, Ying Wang et al. [63] performed a comprehensive FSI study on a patient-
32 specific 3D UA model to study the effect of nasal surgery on OSA. The geometries of

1 pre- and post-surgical UA were reconstructed from high-resolution (0.5 mm interval)
 2 CT data. The UA model started from the nasal cavity and ended at the larynx. The soft
 3 palate was described as the only flexible component. Linear elastic material properties
 4 were defined for the soft palate and palatal muscles. The mesh convergence studies of
 5 both the solid and fluid domain were conducted. Similar to the finding of Sun et al. [24],
 6 significant reduction in the movement of soft palate was observed in this study for both
 7 inhalation and exhalation flow condition (Figure 15). However, UA occlusion was still
 8 undiscovered and the OSA phenomenon was not present. In addition, some doubt exists
 9 regarding the modelling methods of Sun et al. and Wang et al., since experimental
 10 validation was absent for both studies. Wang et al. stated that the invasive measurement
 11 of UA flow conditions and UA material properties was underdeveloped. Thus, current
 12 UA FSI modelling work can only give insight to the OSA mechanism, and there is still
 13 a long way to go to achieve a completely valid UA model for clinical usage.



14
 15
 16

17 **Figure 15: Initial Position (Grids) and Displacement Distribution of Soft Palate**
 18 **Presented in Wang et al. [63]**

19 **2.5 Study Significance and Summary**

20 Predicting treatment outcomes has been a long sought-after goal in oral appliance
 21 research. Mild OSA and supine-dependent airway collapse have been associated with

1 better treatment outcomes, although this is not always the case. More intensive
2 monitoring of UA behaviour during sleep has been investigated for specific
3 relationships with treatment outcomes, and measuring the site of UA collapse during
4 sleep has been shown to be a good indicator of response [64]. A primary collapse in the
5 oropharynx (rather than the velopharynx) can indicate a better response. However, such
6 invasive overnight assessments, although informative, are unlikely to be suitable for
7 routine clinical practice, which limits their applicability. Thus, a shift towards more
8 practical awake prediction factors or tests has arisen, although no definitive model has
9 yet been derived or prospectively validated.

10 Various imaging assessments to investigate craniofacial and UA structure in relation to
11 MAS treatment outcome have been conducted. There is some association between
12 various craniofacial skeletal morphologies and better treatment outcomes, although
13 these are not consistent and generally only weakly predictive [65]. Previous studies
14 have indicated the possibility of using computational modelling methods, such as CFD
15 and FSI, to investigate human medical problems, such as OSA. However, the
16 mechanism of airway collapse is still uncertain and there is no appropriate method to
17 overcome the low efficacy of treatments such as MAS. Computational modelling is an
18 attractive possibility to understand treatment outcomes in individual patients before
19 treatment is initiated. Based on valid CFD and FSI results, existing treatments for OSA
20 (such as MAS) are able to be estimated theoretically. With multiple case studies, it is
21 possible to develop a method to predict treatment outcomes in order to assist clinicians
22 to accurately select potential positive-responding patients.

23

Chapter 3: Research Methodology

3.1 Introduction

Computational technologies and biomechanical theories have recently been applied to study UA mechanics in OSA. CFD has been used to model the UA flow field, originally based on simplified airway models [49], but progressing to using patient-specific geometrical characteristics obtained from medical imaging, which provides a more accurate assessment of airflow characteristics [9]. CFD has now been used to assess the effects of OSA treatment interventions that alter UA anatomical structure. For example, CFD analysis has been combined with UA geometries obtained before and after pharyngeal surgeries to determine the effects on parameters such as pressure drop and flow resistance [10, 11]. Similarly, CFD has been proposed as a tool to determine treatment response to MAS therapy using patient-specific airway geometries obtained from CT scans, with and without MAS [7]. UA flow parameters—such as relative pressure, velocity and flow 3D structure—can be calculated in the computational model. An effective UA enlargement that benefits from MAS treatment can result in a change in the flow parameters. Thus, this change in UA flow can be represented and analysed in the computational UA model.

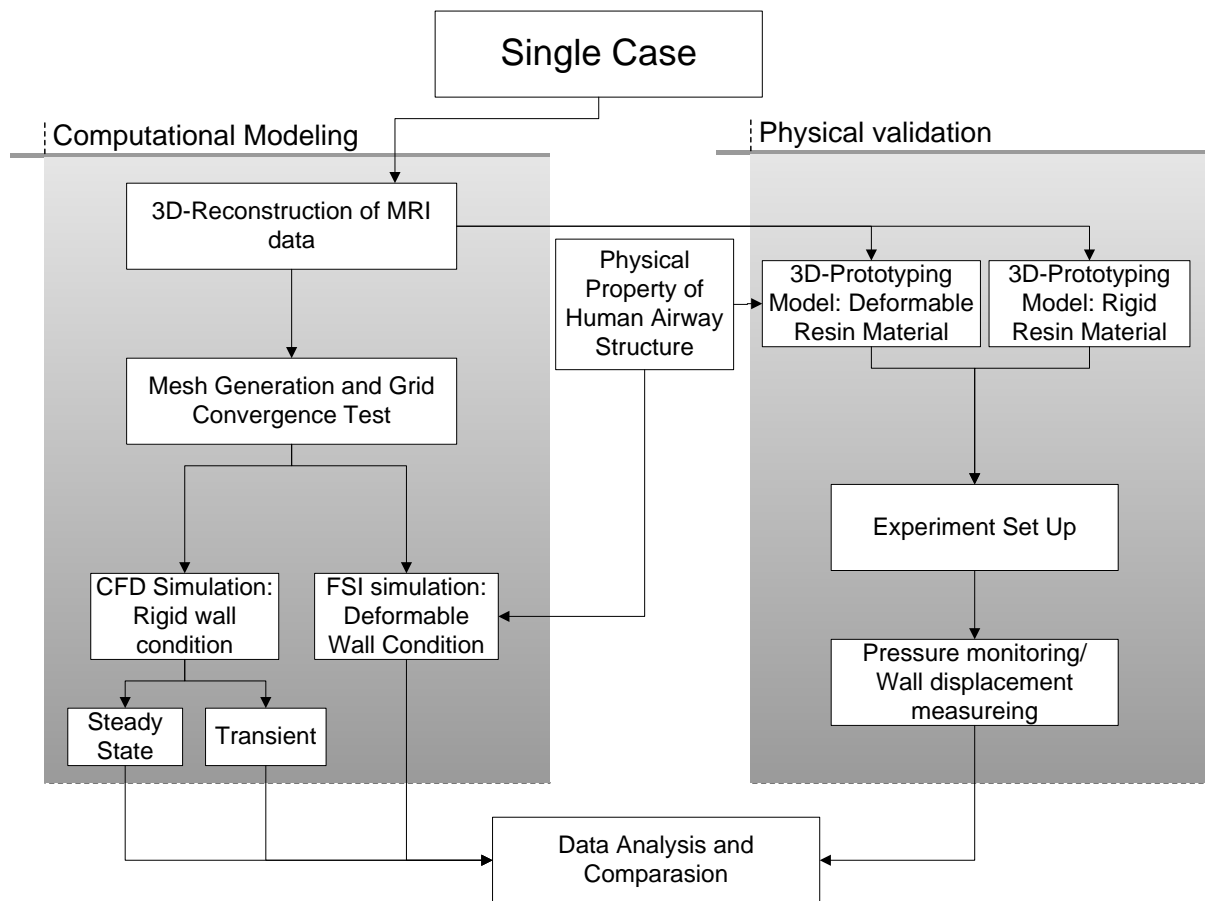
Therefore, CFD is an attractive method to model likely treatment outcomes with MAS in patient-specific airway geometries, before implementing the device. In this original work [7], the UA response to MAS therapy was modelled using patient-specific flow rates and pressures obtained during split-night sleep studies, with and without the device. Although this is likely to provide greater model accuracy, obtaining such patient-specific boundary conditions via intensive overnight monitoring is likely to limit the clinical application of this type of prediction strategy.

The current thesis sought to expand on this original concept study by using a typical human UA flow on patient-specific geometries that only included the pharyngeal section. A single flow rate was used on different patients to calculate the UA velocity and pressure distribution. The results were also used to predict the outcome of MAS treatment. This method simplified the previous treatment-predictive procedure by eliminating the overnight sleep study. The method in this thesis only required a set of

1 medical image before and after treatment provides encouragement of the possibility of a
2 CFD approach applicable to clinical practice.

3 CFD models' rigid wall boundary assumption limits these models' results by not taking
4 into account the interaction between UA flow and UA wall movement that occurs in
5 OSA patients [22, 25, 51, 66]. There have been a limited number of studies (particularly
6 with experimental validation) using FSI in OSA research, with one of the first being an
7 idealised 2D tongue model in 2007 [62], which later developed into a 3D tongue model
8 in 2011 [67]. Early studies also used FSI to model soft palate movement within a
9 realistic UA geometry [24]. These studies indicated the possibility of modelling the
10 flow and structure interaction in UA. Therefore, the current study devoted additional
11 effort to studying the dynamic of UA wall deformation. Patient-specific FSI models
12 were developed from proposed CFD models to incorporate UA collapse. The entire UA
13 structure was simulated to be fully coupled with the flow field. This thesis sought to
14 simulate UA occlusion in OSA and the effect of MAS therapy in a patient responsive to
15 this form of therapy. Additionally, our method was validated experimentally with a
16 physical model.

17 Based on the aim of this thesis, the research methodology concentrated on modelling
18 the mechanism of OSA syndrome and providing feasible methods to predict the
19 treatment outcome. Figure 16 demonstrates the flow chart for modelling a single OSA
20 patient. The patient-specific UA geometries were reconstructed from MRI scans with
21 and without an MAS fitted. A mesh convergence study was performed to optimise the
22 grid. By comparing the CFD results, the difference in UA flow parameters was used to
23 analyse the flow changes that occurred with MAS treatments. The computationally-
24 expensive FSI simulation complemented the CFD simulations by adding the structure
25 movement that caused the hydraulic force, reproducing the UA occlusion. Experimental
26 validation methods were undertaken for the CFD and FSI simulations using fabricated
27 rigid and flexible UA models with accurate patient-specific geometries. The pressure
28 profile in the rigid UA model and the UA wall movement in the flexible UA model
29 were obtained experimentally and compared with the computational results. Multiple
30 OSA cases from a group study to predict the treatment response of MAS were used to
31 determine a relationship between the CFD results and OSA severity (measured in AHI).
32 This relationship could form the basis of a treatment prediction model.



1

3

Figure 16: Study Flow Chart of CFD, FSI and Experiment

4

3.2 Study Case

5

This study selected seven OSA patients with a range of treatment responses to MAS.

6

Table 2 presents the patients' characteristics. The treatment response was determined by

7

the AHI recorded via standard PSG at the baseline (without MAS) and with MAS. Four

8

different types of treatment responses were defined: 'responder' (post-treatment AHI <

9

5/hr or no OSA), 'partial responder' ($\geq 50\%$ AHI reduction from baseline, but AHI >

10

5/hr), 'non-responder' (< 50% AHI reduction) and 'failure' (post-treatment AHI

11

increased). All patients used a set of commercially-available custom-made two-piece

12

MAS (Figure 17, SomnoDentMAS; SomnoMed Ltd, Crows Nest, Australia) [68]. The

13

study was conducted after an acclimatisation period (six to eight weeks), during which

14

the device was titrated to the patients' maximal comfortable limit. Written informed

15

consent was acquired from all patients [69].

16

1
2

Table 2: General Characteristics of the Seven Patients in this Thesis (WO = without MAS, W = with MAS)

Patient	Age	BMI	AHI (WO)	AHI (W)
Responder1	52	29.41	41.5	2.1
Responder2	24	34.68	22	0
Responder3	43	26.73	14.2	4.1
Partial responder	31	24.26	28.4	13.9
Non-responder	49	36.65	29.2	23.6
Failure1	65	25.1	19.5	25
Failure2	57	28.34	16.0	31.7

3



4
5

Figure 17: The Custom-made Two-piece MAS

6

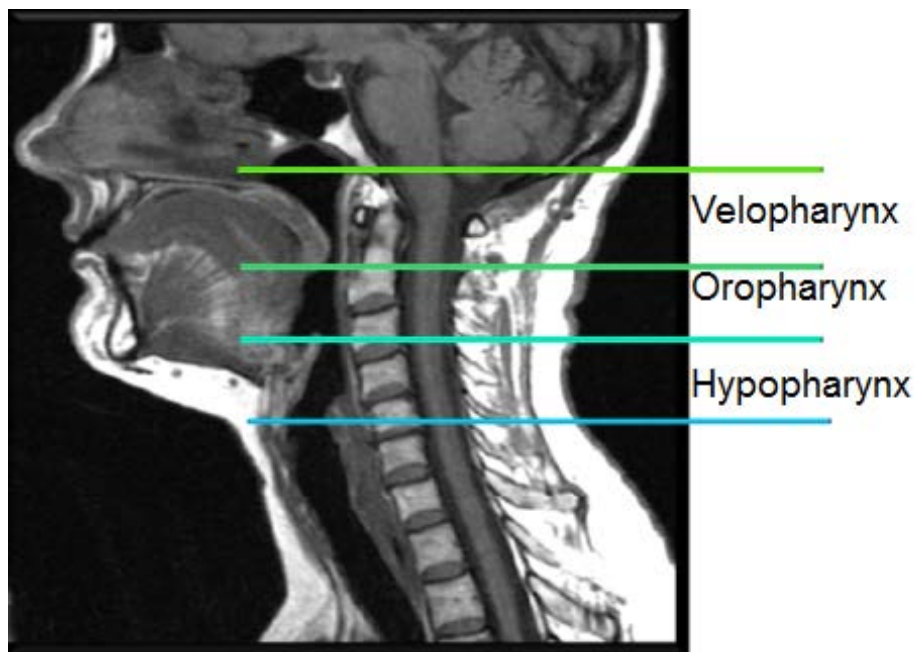
(SomnoDentMAS, SomnoMed Ltd, Crows Nest, Australia)

7 UA MRI was performed using a Philips INTERA 1.5T scanner (Philip Electronics, The
8 Netherlands) with the patient awake and in the supine position. Normal respiration was
9 allowed through the patients' nose and they were instructed to refrain from swallowing.
10 Patients were also instructed to keep their mouth closed and to maintain a relaxed bite,
11 with the tongue touching the front teeth. Axial image slices from the nasopharynx to the

1 vocal cords were obtained with and without the MAS (50 slices, 3 mm thickness, 224 ×
2 512 matrix, FOV 250 mm) [69].

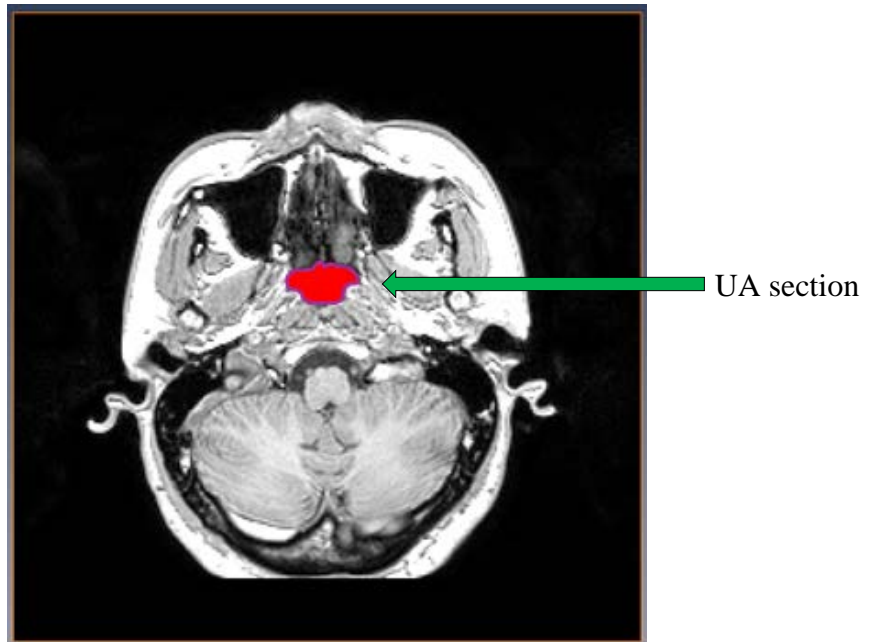
3 **3.3 Reconstruction of UA Geometry**

4 The MRI data (DICOM image) were processed in Amira 5 (Visage Imaging, US). Due
5 to the variation of hydrogen distribution, the skin, fat and skeleton normally have a
6 bright colour, while the body fluid and void space present as dark. The grey region in
7 the scan is soft tissue. In this thesis, the geometry of the UA was defined from the axial
8 cross-section of the hard palate down to the vocal cords (Figure 18), which covered 39
9 to 40 scans. The UA lumen was segmented out on each scan, as shown in Figure 19. A
10 ‘mask’ (group of selected pixels) can be created manually on the scan based on clinical
11 experience. Since breathing was allowed during the scan, the UA boundary line could
12 be blurry due to the movement of the UA wall, which increased the difficulty in
13 segmentation.



14

15 **Figure 18: Definition of Upper and Lower Boundaries of UA Model in this Thesis**



1

2

Figure 19: UA Lumen Marked in a Transverse MRI Scan of an OSA Patient

3

In Amira 5, the wall boundary of the segmented area on each scan can be connected by

4

interpolating the interval geometry between them (Figure 20). In this study, the wall of

5

the airway was created as a surface model. The surface model at this stage was rough

6

and bumpy and did not reflect the UA geometry in reality, since this rough surface was

7

caused by the missing transition between two transverse MRI images. Therefore, in the

8

next stage, a smoothing function was applied to approximate the actual UA geometry.

9

The vertices on the surface model were shifted according to the average position of their

10

neighbour vertices (Figure 21). Since boundary vertices can only shift with adjacent

11

surface vertices, the anatomical characters of particular patients were conserved. The

12

maximum discrepancy between the smooth and unsmoothed surface vertices was less

13

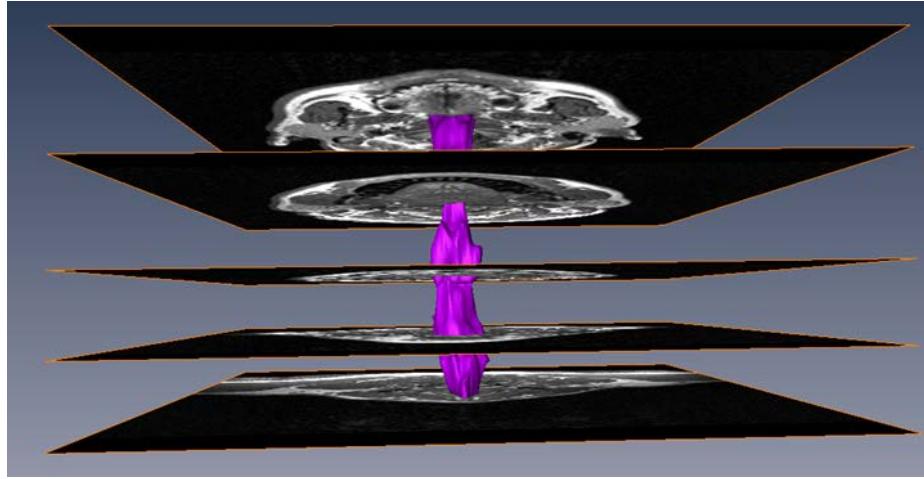
than a single pixel, which would be about 2% of the UA cross-sectional dimension

14

(Figure 21-c). The UA surface model was finally exported as an STL file into ANSYS

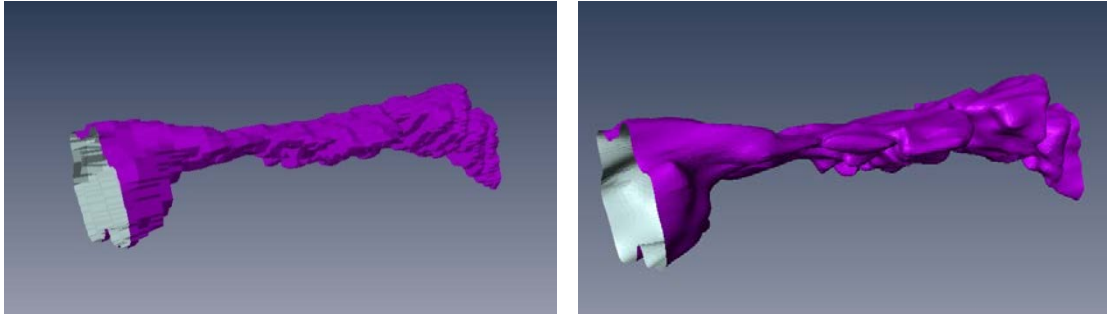
15

ICEM CFD (ANSYS 13.0) to generate discrete volume cells.



1
2

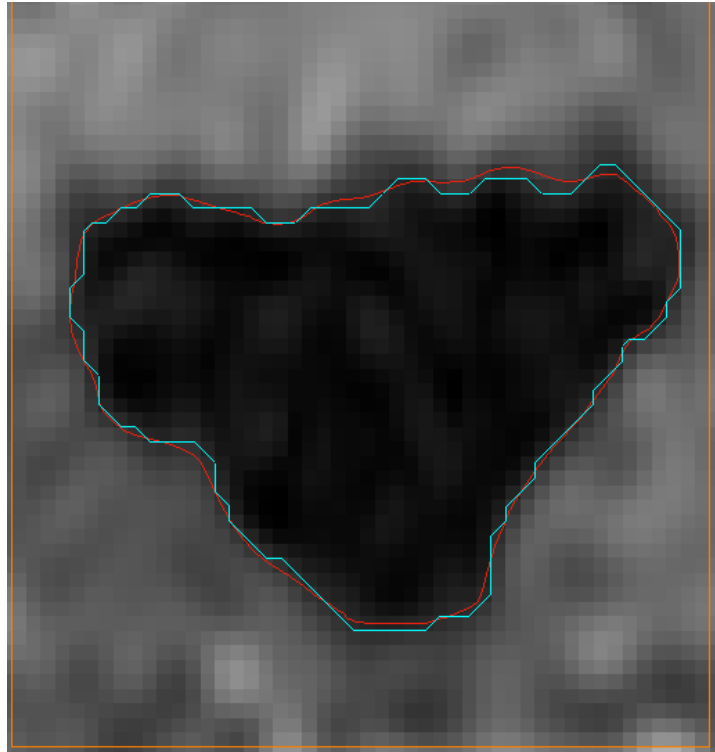
Figure 20: Reconstruction of the UA Geometry in Amira 5



1
2

21-a

21-b



3
4

21-c

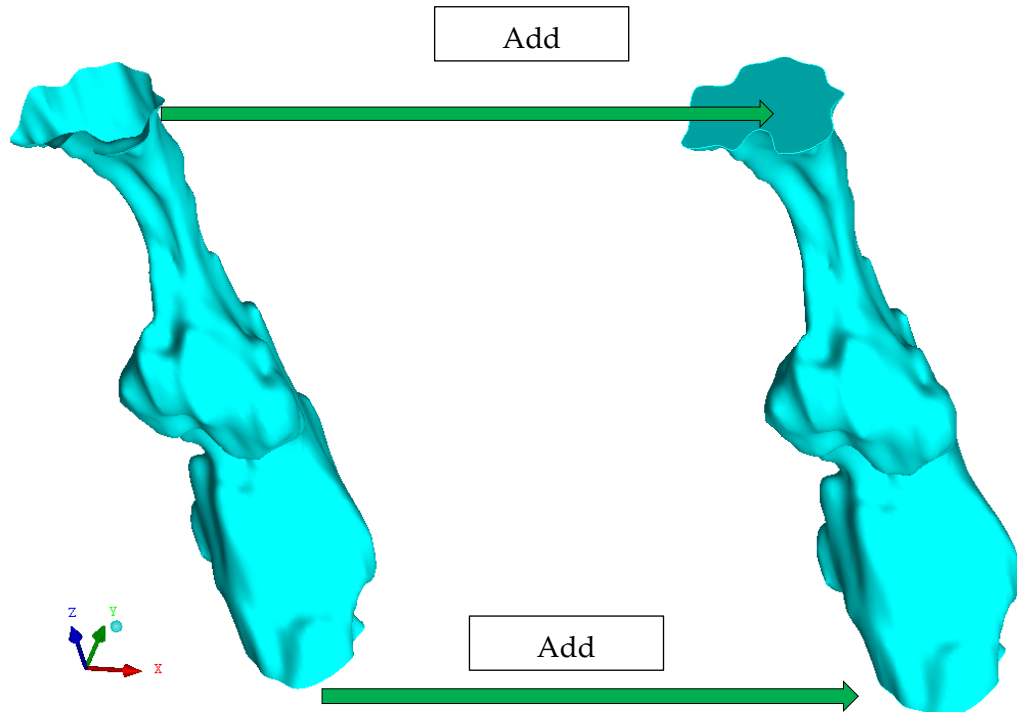
5 **Figure 21: UA Geometrical Changes (a) Before and (b) After Smooth Function in**
6 **Amira 5. (c) Comparison between Unsmoothed (Green) and Smoothed (Red) UA**
7 **Boundary Line**

8 **3.4 The Computational Grid**

9 The STL UA surface model from Amira 5 was a hollow thin-wall model with open inlet
10 and outlet at the nasopharynx and vocal cords, respectively. Surfaces are required at
11 these openings to close the geometry for mesh generation (Figure 21).

12

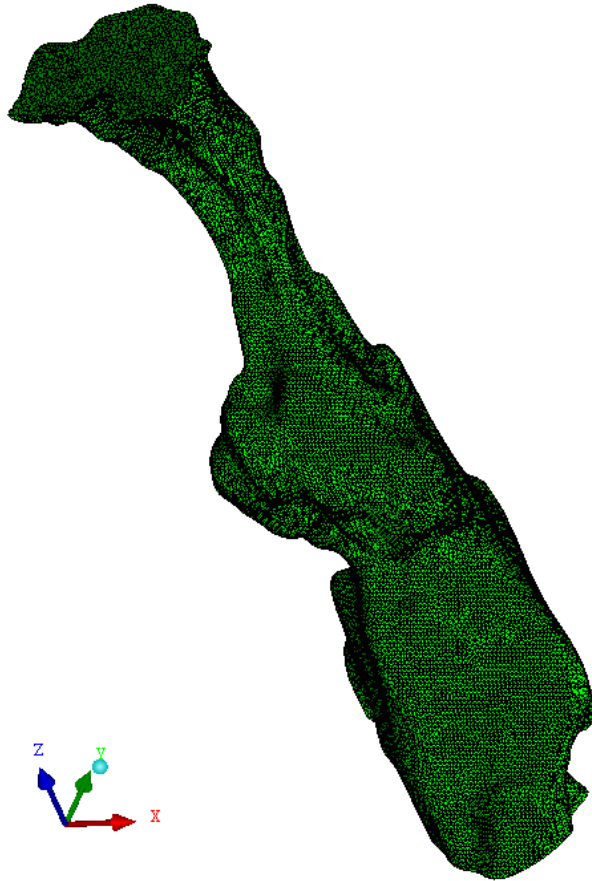
1



2

3 **Figure 22: STL Surface Model Exported from Amira 5.0 to Meshing Software**
4 **ICEM**

5 A structured mesh has advantages in computational efficiency over an unstructured
6 mesh. However, for complex irregular geometries like the UA, a body fitted non-
7 orthogonal structural mesh method is inappropriate. The solution domain cannot be
8 readily mapped into rectangular parallel internal or surface grids, since highly skewed
9 grid lines and unnecessary grid concentrations become inevitable near those small
10 geometry features. In this study, a refined unstructured hybrid meshing method was
11 implemented for the UA flow domain. The unstructured mesh has a simple topology
12 and can be easily applied to complex geometries [70]. The unstructured tetrahedron
13 surface mesh is shown in Figure 22.

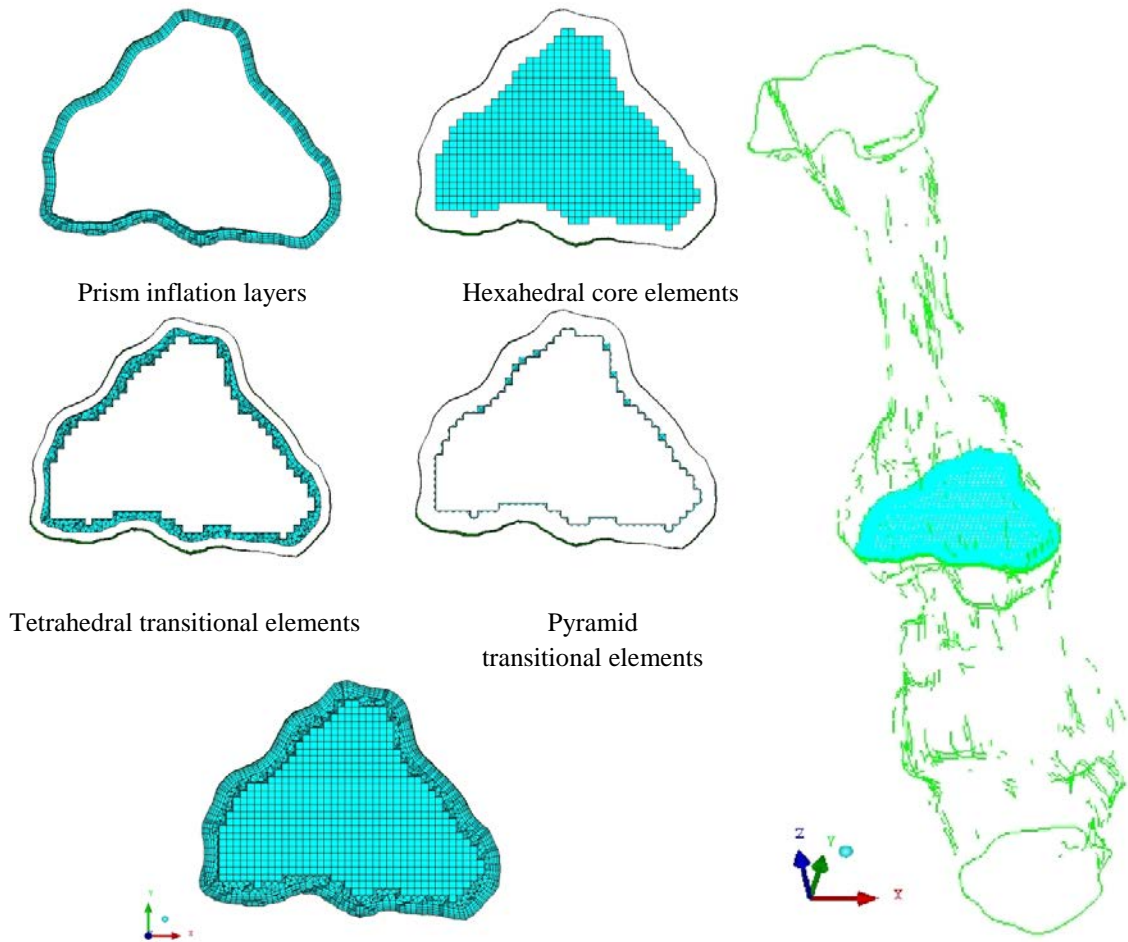


1
2
3

Case: Responder-1 pre-treatment model. Grid quantity: 1.3 million.

Figure 23: Unstructured Surface Grid for UA Geometry

4 To capture the viscous flow features near the wall, five layers of inflation prism grids
5 were placed along the wall boundary. At the core of the UA volume, structured
6 hexahedral elements were generated to achieve maximum grid efficiency. The gap
7 between the hexahedral core and prism inflation boundary was filled with a tetrahedral
8 and pyramid element for a smooth transition (Figure 23). The main disadvantage of
9 unstructured mesh is that it can easily have high aspect ratio and high skewness
10 elements at regions close to sharp geometries, particularly next to the boundary layer
11 grids. False diffusion error can occur in discretisation, as the direction of the flow vector
12 does not align with the calculation path of the discretisation method. Thus, in this study,
13 care was taken in meshing to increase the uniformity of elements.



1

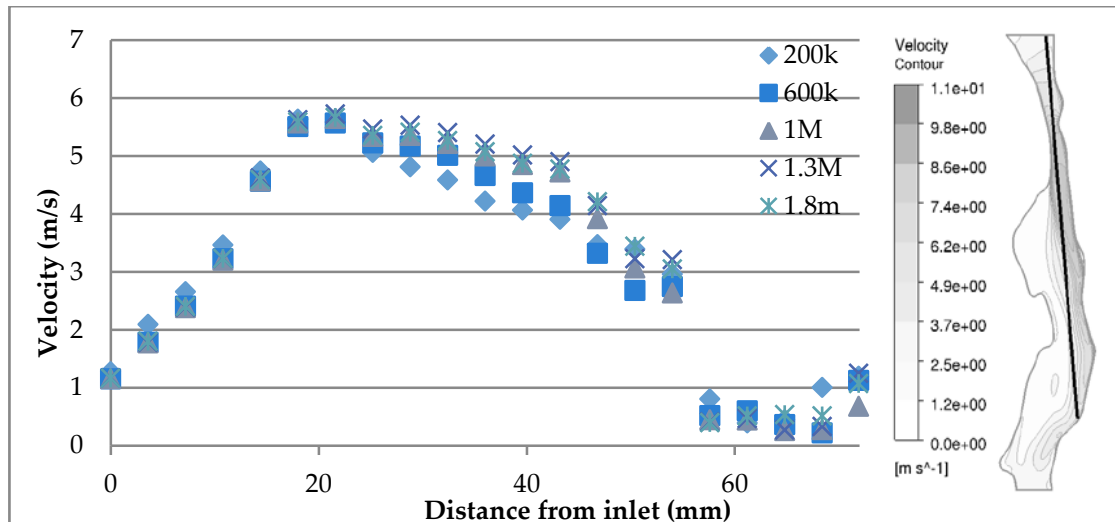
2

Case: Responder-1 pre-treatment model. Grid quantity: 1.3 million.

3

Figure 24: Hybrid Mesh for Complex UA Geometry

4 The quality of this hybrid mesh was assessed with the automatic check function in
 5 ANSYS ICEM. The elements of high aspect ratio and skewness were filtered and
 6 improved with grid smoothing. Another feature that can indicate the quality of the mesh
 7 is the number of grid points. In terms of computational efficiency, it is desirable to have
 8 a mesh that has fewer elements, yet achieves reasonable performance. A mesh
 9 convergence study was performed on models using different grid scales. This study
 10 chose the 1.3 million-mesh size (maximum grid edge length: 0.5 mm) because it had
 11 acceptable accuracy as the result only had a maximum variation of 2.5% to the result of
 12 1.8 million-mesh. However, it saved over 30% computational time compared to those
 13 meshes with more elements (Figure 24).



1

2 **Figure 25: Plot of Axial Velocity along a Vertical Line (Showing from the Right)**
 3 **from the Inlet to the Wall of the Larynx with Different Mesh Densities**

4 **3.5 Advection Scheme**

5 Advection is the numerical mechanism of transporting a quantity (such as velocity or
 6 temperature) through the solution domain. The integration point value is approximated
 7 from the nodal values (Equation 3-1). The advection schemes in CFX can be illustrated
 8 as:

9
$$\varphi_{ip} = \varphi_{up} + \beta \nabla \varphi \cdot \Delta \vec{r}$$
 3-1

10 where φ_{ip} is the integration point value, φ_{up} is the value at the upwind node, \vec{r} is the
 11 vector from the upwind node to the integration point, and β is a blend factor that varies
 12 from zero to one and shifts the advection scheme between the first and second order.
 13 The second-order scheme is more accurate in predicting steep spatial gradients. The
 14 high-resolution scheme (CFX solver) was chosen in this study. This is a special upwind
 15 scheme of up to second-order accuracy. It has the advantage of capturing the flow in the
 16 discontinued structures and narrow structures of the UA.

17 **3.6 Governing Equation of CFD Models**

18 Turbulence simulation can be the most important yet controversial component in CFD
 19 studies. The proper use of turbulence models can markedly reduce computing expense,
 20 while still retaining accuracy. According to recent findings, UA flow can be classified

1 as a complex transitional type of flow, which indicates that neither a laminar equation
 2 nor a standard two-equation turbulence model may be sufficient to fully describe the
 3 flow characters [22, 27, 58-60]. A good understanding of the fundamentals in fluid
 4 mechanics is essential.

5 The Reynolds number is as follows:

$$6 \quad \text{Re} = \frac{\rho v D}{\mu}, \quad 3-2$$

7 where ρ is the fluid density, v is the mean velocity, D is the hydraulic diameter and μ is
 8 the dynamic viscosity of the fluid. This is widely used to characterise the flow regimes,
 9 which are laminar, transitional and turbulent. For an imprecise engineering convention,
 10 the flow in a round pipe is laminar if $\text{Re} < 2,300$, turbulent if $\text{Re} > 4000$, and transitional
 11 if Re lies between those values and flow may randomly switch between laminar and
 12 turbulent conditions [71].

13 The time-dependent 3D Navier–Stokes equations include the time-dependent continuity
 14 equation for conservation of mass, three time-dependent conservation of momentum
 15 equations, and a time-dependent conservation of energy equation. The Navier–Stokes
 16 equations were developed from Cauchy’s equation of motion and the constitutive
 17 equation, while can resolved all the characters of the flow [71, 72]. The Navier–Stokes
 18 equations are as follows:

$$19 \quad \rho \frac{Du_i}{Dt} \delta_j = \{ \rho f_j - \frac{\partial p}{\partial x_j} + \frac{\partial}{\partial x_j} (\lambda \frac{\partial u_i}{\partial x_i}) + \frac{\partial}{\partial x_i} [\mu (\frac{\partial u_i}{\partial x_j} + \frac{\partial u_j}{\partial x_i})] \} \delta_j \quad 3-3$$

20 In this study, the UA flow was considered an incompressible, steady-state and constant
 21 viscosity flow [22]. The Navier–Stokes equations can be simplified as:

$$22 \quad \frac{\partial}{\partial x_i} (u_i) = 0 \quad 3-4$$

$$23 \quad \rho \frac{\partial}{\partial x_j} (u_j u_i) = - \frac{\partial p}{\partial x_i} + 2 \frac{\partial}{\partial x_j} [\mu \frac{1}{2} (\frac{\partial u_i}{\partial x_j} + \frac{\partial u_j}{\partial x_i})] + \rho f_i \quad 3-5$$

1 This incompressible flow assumption still works well in dealing with a compressible
 2 fluid at low Mach numbers (lower than Mach 0.3), such as flow in the UA due to
 3 normal breathing of air at room temperature [72].

4 Directly solving the Navier–Stokes equations is computationally expensive. To simulate
 5 steady flows, a widely used approximation made to the Navier–Stokes equations is
 6 Reynolds averaging (RAN). The flow variable is decomposed into a mean component
 7 and a fluctuating component. By applying time-averaging to the Navier–Stokes
 8 equations, Equations 3-4 and 3-5 can be presented as:

$$9 \quad \frac{\partial}{\partial x_i}(U_i) = 0 \quad 3-6$$

$$10 \quad \rho U_j \frac{\partial U_i}{\partial x_j} = \rho \bar{f}_i + \frac{\partial}{\partial x_j} [-\bar{p} \delta_{ij} + \mu (\frac{\partial U_i}{\partial x_j} + \frac{\partial U_j}{\partial x_i}) - \overline{\rho u'_i u'_j}] \quad 3-7$$

11 The term $(-\overline{\rho u'_i u'_j})$ is called the Reynolds stress tensor, which refers to six unknown
 12 quantities that are determined by closure equations. The Boussinesq hypothesis
 13 postulates the Reynolds stress tensor to have a linear relationship with the mean strain
 14 rate tensor, $(\frac{\partial U_i}{\partial x_j})$:

$$15 \quad -\overline{\rho u'_i u'_j} = \mu_t (\frac{\partial U_i}{\partial x_j} + \frac{\partial U_j}{\partial x_i}) - \frac{2}{3} \rho k \delta_{ij} \quad 3-8$$

16 where μ_t is the turbulent viscosity, which is assumed to be isotropic; k is the turbulent
 17 kinetic energy ($k = \frac{1}{2} (\overline{u'^2} + \overline{v'^2} + \overline{w'^2})$); and δ_{ij} is the Kronecker delta [73]. Two extra
 18 transport equations are required to solve μ_t and k . This is known as the two-equation
 19 turbulence model. In this study, the turbulence model applied to solve the UA flow
 20 domain was the SST $k-\omega$ model with optimised performance. This sophisticated model
 21 was first introduced by Menter et al. in 2003 [74]. The k equation is the same as in the
 22 $k-\omega$ model:

$$23 \quad \frac{\partial(\rho k)}{\partial t} + \frac{\partial(\rho k u_i)}{\partial x_i} = \mu_t \left[\frac{\partial u_j}{\partial x_i} + \frac{\partial u_i}{\partial x_j} \right] \frac{\partial u_j}{\partial x_i} + \frac{\partial}{\partial x_i} \left[\left(\frac{\mu_t}{\sigma_k} + \mu \right) \frac{\partial k}{\partial x_i} \right] - \beta^* \rho k \omega \quad 3-9$$

1 The ε equation is transformed into a ω equation by substituting $\varepsilon = k-\omega$:

$$\begin{aligned}
 & \rho \frac{\partial \omega}{\partial t} + \rho u_i \frac{\partial \omega}{\partial x_i} = \rho \gamma_2 \left[\frac{\partial u_j}{\partial x_i} + \frac{\partial u_i}{\partial x_j} \right] \frac{\partial u_j}{\partial x_i} + \frac{\partial}{\partial x_i} \left[\left(\frac{\mu_t}{\sigma_\omega} + \mu \right) \frac{\partial \omega}{\partial x_i} \right] - \beta \rho \omega^2 + \\
 & 2\rho(1-F_1)\sigma_{\omega^2} \frac{1}{\omega} \frac{\partial k}{\partial x_i} \frac{\partial \omega}{\partial x_i}
 \end{aligned}
 \tag{3-10}$$

3 where $\alpha = 0.553$, $\beta = 0.075$, $\beta^* = 0.09$, $\sigma_\omega = 2.0$, $\sigma_{\omega^2} = 0.856$ and $\sigma_k = 2.0$ [74].

4 In addition, the limitations is added to the eddy viscosity, μ_t , to prevent the generation
 5 of turbulence in the stagnation region, while improving the performance in wake
 6 regions:

$$\mu_t = \frac{\rho \alpha_1 k}{\max(\alpha_1 \omega, SF_2)}
 \tag{3-11}$$

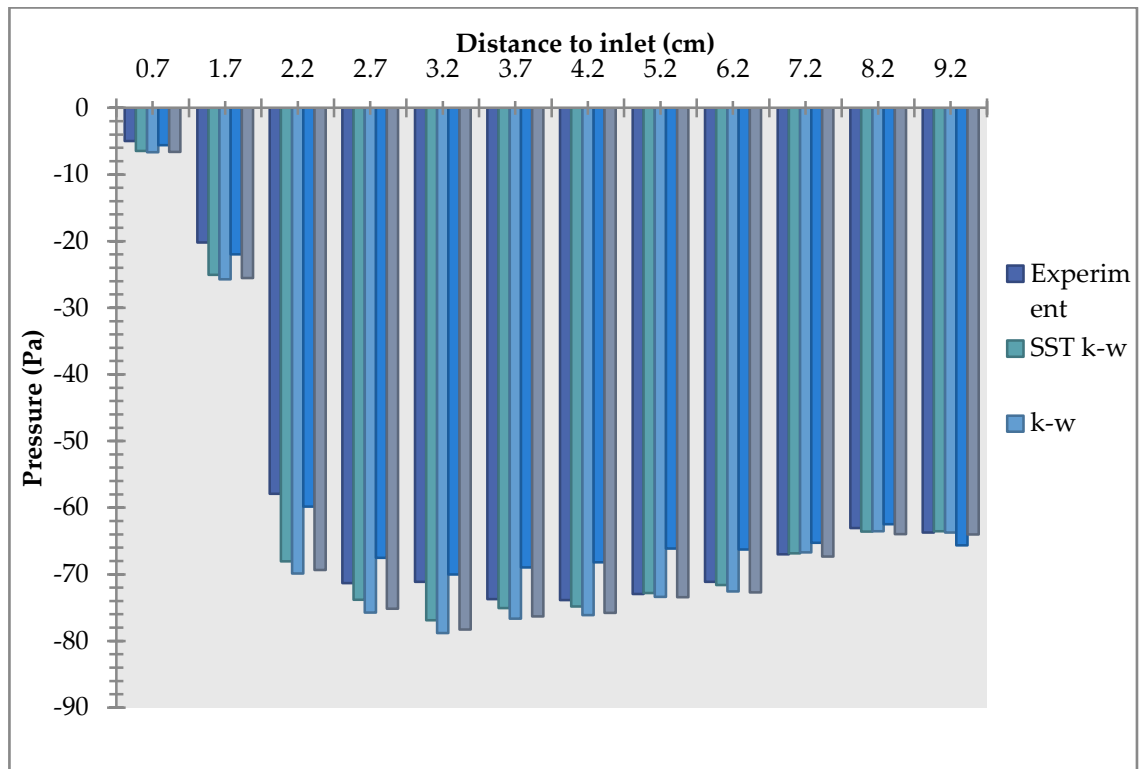
8 where $\alpha_1 = 0.56$ and F_1 and F_2 in are blending functions that blend each constant (ϕ)
 9 from the original k- ω model (ϕ_1) to the transferred k- ε model (ϕ_2) of Menter et al:

$$\phi = F_1 \phi_1 + (1 - F_1) \phi_2
 \tag{3-12}$$

11 The SST $k-\omega$ model has superior performance in adverse pressure gradient and
 12 separating flow. However, it is suggested that SST $k-\omega$ over-predicts turbulence in zero
 13 stagnation and strong acceleration regions [74].

14 As the UA geometry is complex, the best way to find the most suitable turbulence model
 15 is to conduct a comparison study. This research employed the laminar, k- ε , k- ω and SST
 16 k- ω models to simulate the patient case of Responder-1 at pre-treatment. Identical mesh
 17 and boundary conditions were used in all simulations. The mesh contained 1.34 million
 18 unstructured elements. The discharge flow rate was specified as 10 L/s (166 ml/s) at the
 19 vocal cord, and the environmental pressure condition was specified at the nasopharynx
 20 to mimic an inspiratory flow. The experimental data were included as a benchmark.
 21 Chapter 4 will present the details of this experimental study, while Figure 25 depicts the
 22 results of this comparison study. At the upstream of the restriction region in the
 23 velopharynx, the UA flow generally had a low Reynolds number ($Re < 1,500$). The
 24 laminar model gave the closest pressure value to the experimental readings. However,

1 the flow accelerated and became turbulent in the velopharynx ($Re > 2,500$), while the
 2 flow separation and swirling occurred in the oropharynx and larynx. The two-equation
 3 RAN models generally performed well compared to the laminar model. The pressure
 4 results were similar among the RANS models; however, the SST model was slightly
 5 closer to the benchmark. Thus, the SST $k-\omega$ model was used for the rest of this thesis to
 6 model the UA flow.



Case: Responder-1 without MAS. Flow rate: 10L/min (166ml/s).

Figure 26: Comparison Study of UA Pressure Distribution by Experiment and Turbulence Models along the UA at a Flow Rate of 10 L/min (166 ml/s)

3.7 Boundary Conditions of CFD Model

12 The inspiratory UA flow was modelled over all patient cases, as inspiration is associated
 13 with negative pressures that cause airway collapse in OSA and greater airflow pressure
 14 and velocity gradients. The inlet boundary was located at the horizontal cross-section of
 15 the nasopharynx, while the outlet boundary was set at the vocal cord (Figure 18). Based
 16 on the literature, a steady outlet volume flow rate of 166 ml/s (10 L/min) was used in the
 17 simulations [27], as patient-specific flow rates were not measured. The turbulence
 18 intensity was set as 10% to mimic real conditions [60] and an average gauge pressure of

1 0 Pascal was defined at the inlet. For the standard CFD simulations, the wall of the UA
2 was specified as rigid, smooth and non-slip.

3 **3.8 The Solution Process**

4 The solver ANSYS CFX (CFX-5, ANSYS 13.0) adopted in this study uses a coupled
5 solver to compute the fluid flow field. The solution was solved implicitly at all the time
6 steps. Here, we solve the UA flow as a steady-state problem; a false time step will be
7 given as to under-relaxing the equations in the iterations. The iteration calculation was
8 solved as in a ‘guess-and-correct’ mechanism. The residual is the imbalance as in the
9 linear system of the discretise equations. The criterion of convergence was specified as
10 a residual target of 1×10^{-6} . The simulation took an eight-core 3.0 Hz desktop PC to
11 finish in 10 hours.

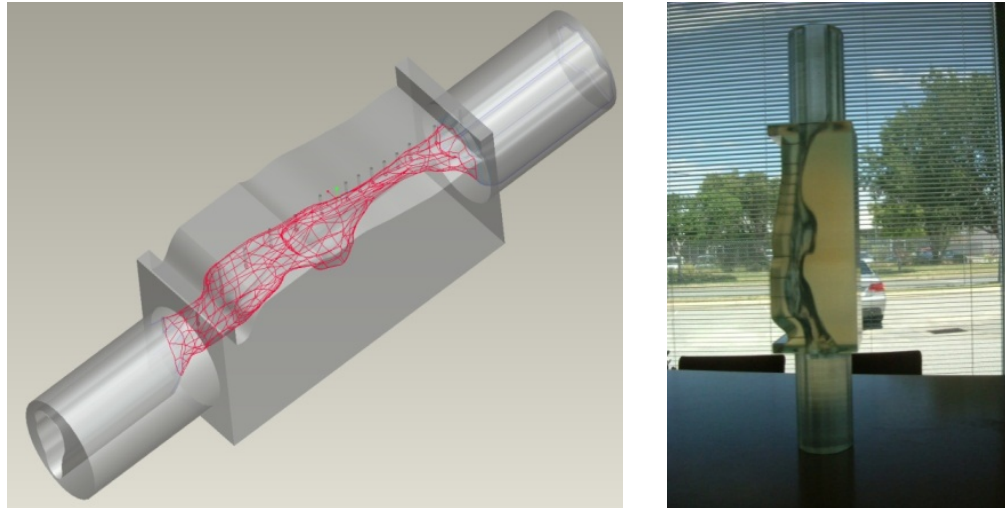
12 **3.9 Experimental Validation of the CFD Model**

13 The objective of this experiment was to validate the CFD simulations by producing the
14 steady flow in a model of the UA of a specified OSA patient (case: responder). The
15 model was fabricated to be identical to that used in the CFD simulations, with a series
16 of pressure tapings to measure the pressure profile, as discussed below.

17 **3.9.1 The Rigid Experimental UA Model**

18 The airway model was developed from the MRI images of the patient case responder.
19 The STL file of airway geometry was imported into the CAD Pro/Engineer 4.0 software
20 (also named Creo Elements/Pro, version 4.0, Parametric Technology Corporation). A
21 volume of the 1:1 UA lumen was subtracted from a solid block. Both the inlet and outlet
22 of the airway were extended as connectors to the external air supply system. The cross-
23 sections of these extensions were the same as the inlet and outlet profiles. In order to
24 avoid a sudden change in geometry, smooth transitions were placed between these
25 extensions and the airway volume. This CAD design was fabricated using rapid
26 prototyping (Figure 26). The material of this rapid prototyping model was a transparent
27 polymer (Watershed XC 11122, DSM Somos, US). This rapid prototyping material has
28 the best transparency; however, the model was not sufficiently optically transparent to
29 undertake particle imaging velocimetry. Along the top of the model, there were 15
30 pressure taps drilled vertically. Each hole had an inner diameter of 0.8 mm. A 1.5 mm

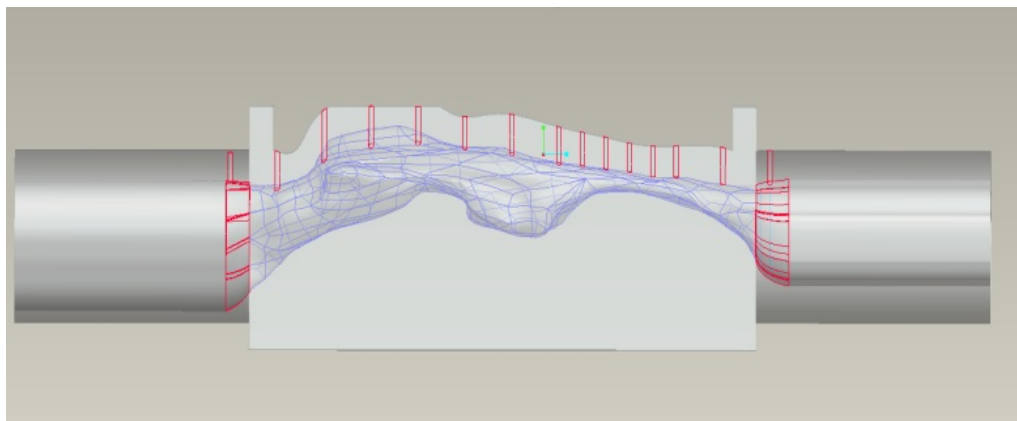
1 hole was drilled halfway through the smaller holes to fit the brass tubes. These brass
2 tubes were connected with the micro-manometer via several plastic tubes [75]. Section
3 4.2.1 will discuss the reason for designing the pressure tube at the posterior wall of the
4 UA.



5
6

(a)

(b)



7
8

(c)

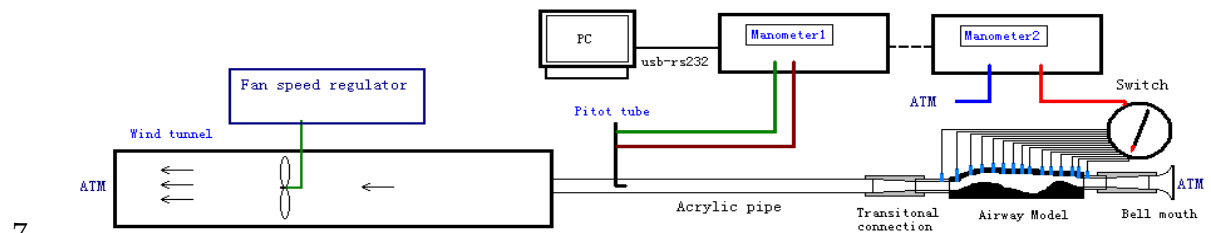
9 (a) The splines (in red) indicate that the UA structure was built as an internal void volume inside the
10 model; (b) The fabricated model; (c): Highlights (red splines) the extra transitional geometries at the inlet
11 and discharge of original UA geometry (blue splines), and the 15 pressure taps placed along the back of
12 the UA lumen.

13 **Figure 27: Rigid UA Model Fabricated with the Rapid Prototyping Method**

14 **3.9.2 Supply and Regulate the Flow**

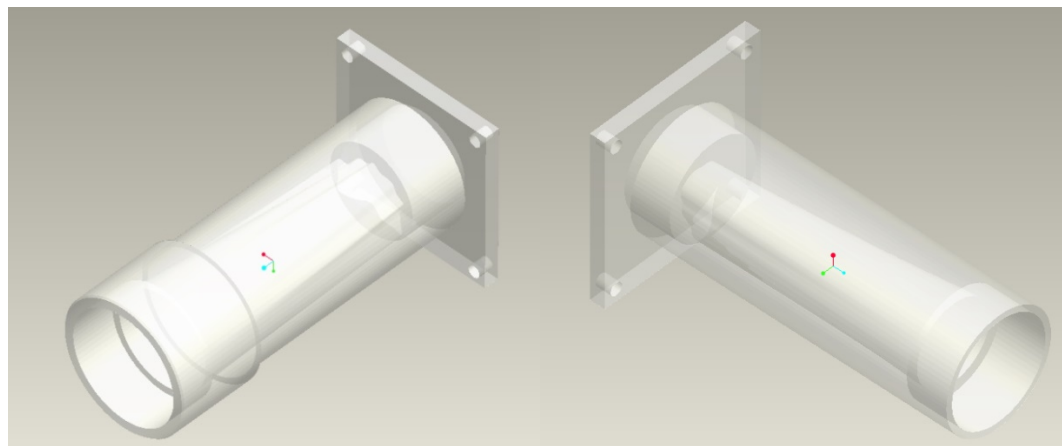
15 Figure 28 demonstrates the experimental setup to measure the wall static pressure in the
16 rigid airway model. A smooth suction airflow was generated with a fan in a small wind
17 tunnel that had a diameter of 640 mm. The fan speed was controlled by a digital fan
18 speed regulator. The wind tunnel and model were connected with a 1,200 mm long

1 acrylic pipe. The diameter of the pipe was 1 inch (25.6 mm+). The inlet flow was
 2 smoothed by an aluminium bell mouth. The bell mouth was designed following the ISA
 3 1932 Nozzle standard (ISO-5167-3). The throat and pipe diameters were 32 and 60 mm,
 4 respectively. To avoid a sudden change in geometry, two extra 80 mm long transitional
 5 connections were fabricated to gradually transform the geometry from the airway
 6 boundary profiles to the circular pipe profile (Figure 28).



7
8

Figure 28: Equipment Setup for Pressure Measurement



9
10

(a)

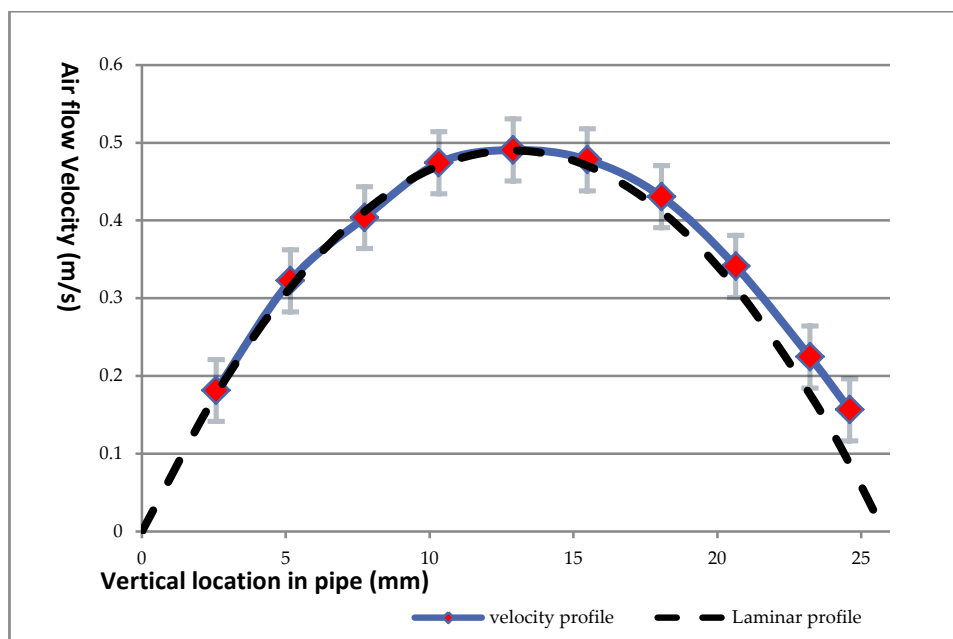
(b)

11 **Figure 29: (a) Inlet and (b) Outlet Connection Design to Provide a Smooth Flow**
 12 **Transition by Transferring the Irregular UA Boundary to the Circular Pipe**
 13 **Profile**

14 **3.9.3 Acquire Pressure Profile**

15 There were 15 pressure taps placed along the back of the airway model, six of which
 16 were located at the velopharynx area, with an interval of 5 mm. The rest were
 17 distributed at every 10 mm, with two located on the inlet and discharge of the model.
 18 The pressure taps had a small inner diameter of 0.6 mm, which enabled the taps to have
 19 negligible effect on the UA flow.

1 Each pressure tap could be selected to connect with digital manometer 2 (FCO510,
 2 Furness Controls, Full scale: $\pm 0\sim 200$ Pa/ $\pm 0\sim 2,000$ Pa) via a flow switch. The flow
 3 velocity was measured by using a Pitot-static tube at the downstream of the pipe flow.
 4 The Pitot tube had a small diameter of 2 mm so the effect on the flow was minimised.
 5 The probe of the Pitot tube traversed vertically along the centre of the pipe. The location
 6 of the probe was measured with a magnetic digital height gauge (Mituyoyo 192-661,
 7 600 mm full scale, 0.01 mm accuracy). The digital manometer 1 (FCO510, Furness
 8 Controls, full scale: $\pm 0\sim 20$ Pa/ $\pm 0\sim 200$ Pa) was used to measure the differential
 9 pressure in the Pitot tube and static pressure in the acrylic pipe at the position of 1,000
 10 mm from the outlet of the airway model. As a result, the velocity profile of the
 11 discharge pipe flow could be calculated along the vertical axis. Since the estimated
 12 Reynolds number in the pipe was 538, this distance (1,000 mm) allowed the discharge
 13 flow to be fully developed into a parabolic laminar flow profile. The resultant flow rate
 14 was calculated based on this parabolic profile (Figure 29) via Matlab (MathWorks, US).



15

16 The velocity value was acquired from 10 points on every 2.5 mm through the vertical radial direction of
 17 the duct.

18 **Figure 30: Vertical Velocity Profile of Airflow in the Connecting Pipe**

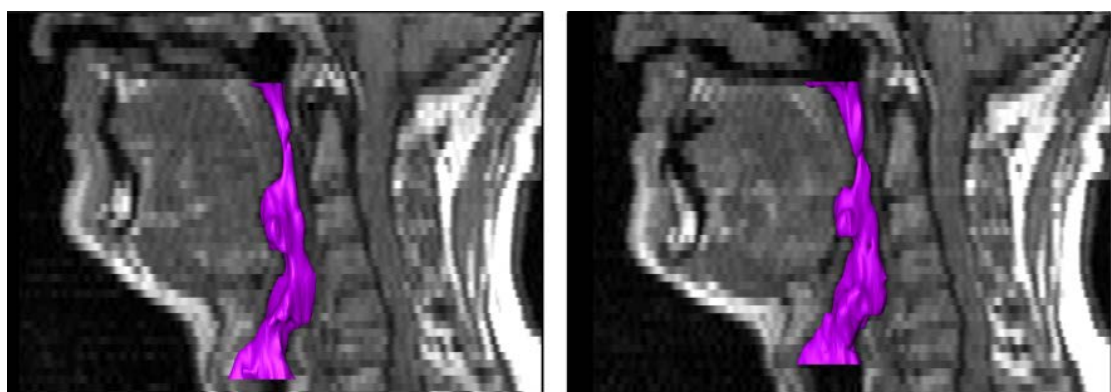
19 The pressure data of each manometer were recorded by a PC in real time through the
 20 RS232C connection. The sampling interval was 0.2 seconds. The pressure readings in
 21 both manometers were averaged over every 20 seconds under quadratic mean method.

1 **3.10 Modelling the Flexible UA Model: The FSI Method**

2 This study hypothesised that the UA structure could be treated as a collapsible tube [2].
3 The UA wall stays in place because of the balance of the dilating and collapsing forces.
4 The dilating forces consist of the UA muscle tone, mechanical structure of the UA wall
5 and positive intraluminal UA pressure. The collapsing forces include the surrounding
6 tissue force, negative intraluminal force and surface adhesive force. For OSA, the
7 narrowing of the UA lumen restricts the flow and increases the flow velocity.
8 According to Bernoulli's theory, the fast-moving airflow in the UA can enhance the
9 negative intraluminal pressure, which also increases the collapsing forces. The
10 imbalance in UA dilating and collapsing forces can finally induce UA collapse. Based
11 on this hypothesis, an FSI method was developed to model the collapse of the UA
12 structure before MAS treatment. The post-MAS treatment case was studied via the same
13 method to indicate the difference in UA wall movement.

14 **3.10.1 Study Case**

15 The OSA patient case Responder-1 (see Table 2) who had been classified as a typical
16 responder to MAS treatment (post-treatment AHI < 5/hr or no OSA) was selected for
17 this thesis. Section 3.3 reconstructed the UA geometries for before and after treatment
18 from the MRI images (Figure 31). In order to compare with the treatment response, this
19 study also selected the case Failure-2 for FSI modelling.



20 (a)

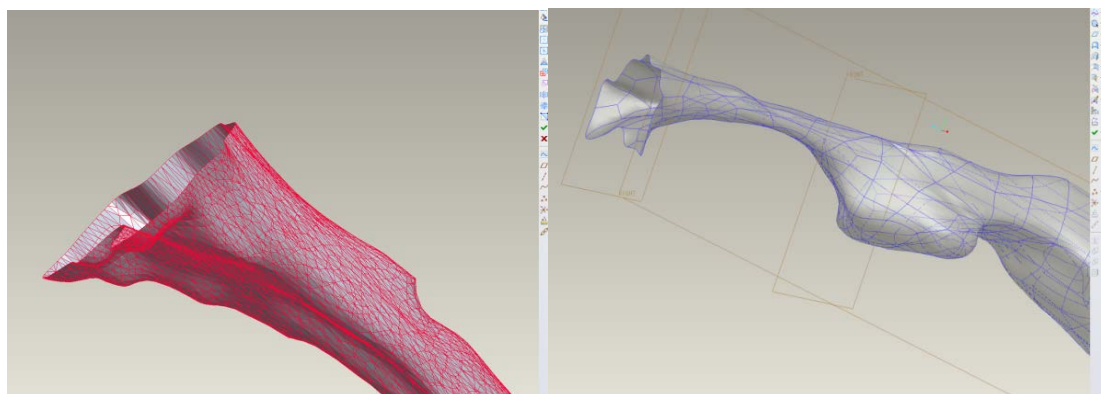
21 (b)

22 **Figure 31: Reconstruction of UA Geometries (a) Before and (b) After MAS**
23 **Treatment**

1 3.10.2 Defining Geometries of the FSI Model

2 The FSI UA model was defined to have a UA fluid domain and solid UA wall domain.
3 The geometries of these domains were created in Pro/Engineer 4.0 with the Reverse
4 Engineering module. The Reverse Engineering function was applied to convert the STL
5 data to engineering geometries that were available for modification and further
6 development. The UA geometry of the FSI model was identical to the CFD model. The
7 inlet boundary was located at the nasopharynx, while the outlet boundary was set at the
8 vocal cord. The UA fluid domain was the same as the CFD computational domain,
9 which represented the UA lumen. The solid wall of the UA was defined as a wall
10 structure with a uniform thickness of 2 mm.

11 The procedure is shown in Figure 32. Initially, the STL UA geometries (from Amira 5.0)
12 were imported as faceted wireframes. The boundaries of the surface were computed
13 based on geometrical characters, and the engineering surface was then computed from
14 these boundary lines. The quality of these boundary lines was not fully controlled by the
15 program. Without manual modification, the boundary lines could easily be too close to
16 each other or have a large curvature, which could cause problems such as folding,
17 overlapping and broken surfaces. Most of the problematic surfaces could be refined by
18 splitting the surface boundary lines (edges) or relocating the four vertices. The
19 engineering-correct surface was regenerated based on new edges and vertices. Although
20 this caused slight geometrical changes, the refined surface could be further developed
21 into 3D solid models of the UA wall and UA lumen.

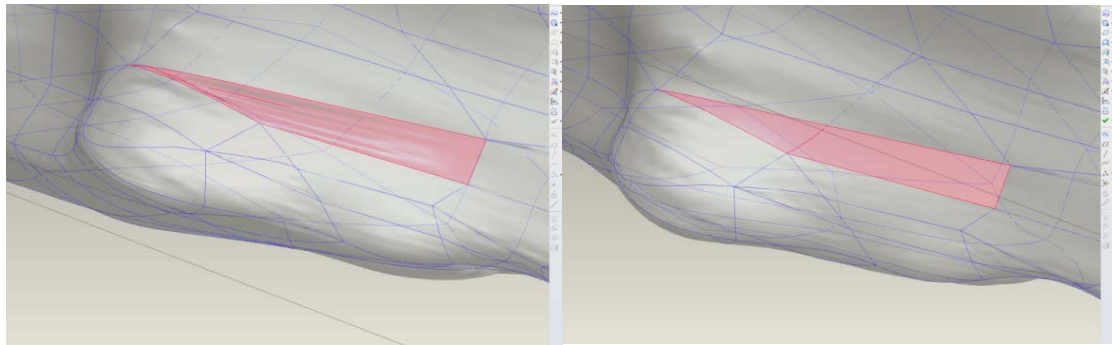


22

23

(a)

(b)



1

2

(c)

(d)

3

(a) Refine the faceted geometry, (b) Create the surface boundary lines, (c) The folded and overlapping surface, (d) The refined surface.

4

5

Figure 32: Procedures of Establishing Engineering Airway Model in Pro/E

6

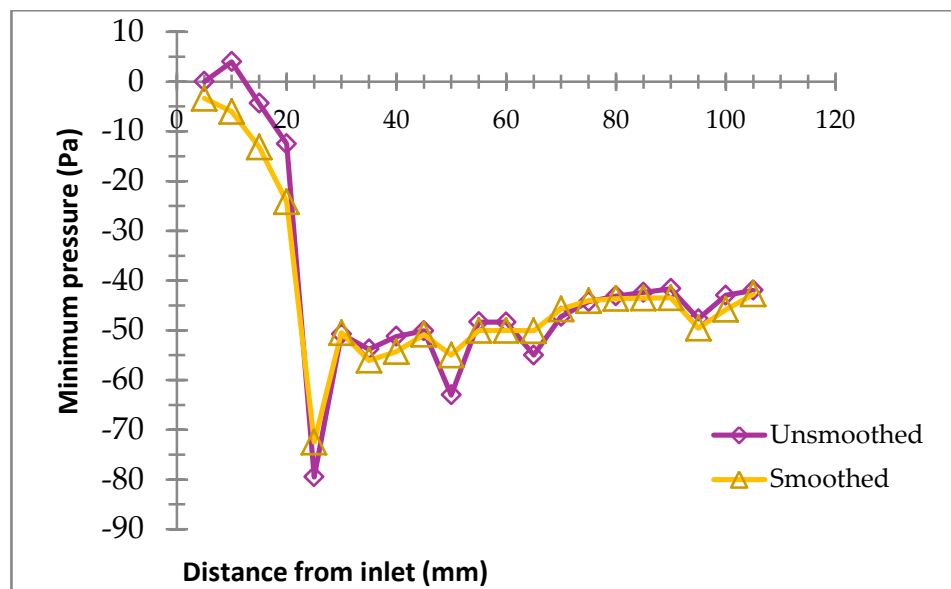
Extra geometry smoothing was required for surface generation, which reduced the chance of having low mesh quality or surface error (such as Figure 31-c). However, as the geometry changed, the flow profile would change as well. Thus, an extra CFD simulation based on this smoothed geometry was performed, and the result indicated that the change in flow pattern was insignificant.

7

8

9

10



11

12

Study case: Responder. Air flow rate: 166 ml/s.

13

Figure 33: Comparison of the CFD Result of the Unsmoothed UA Geometry Used in CFD and the Smoothed Geometry used in FSI Simulation.

14

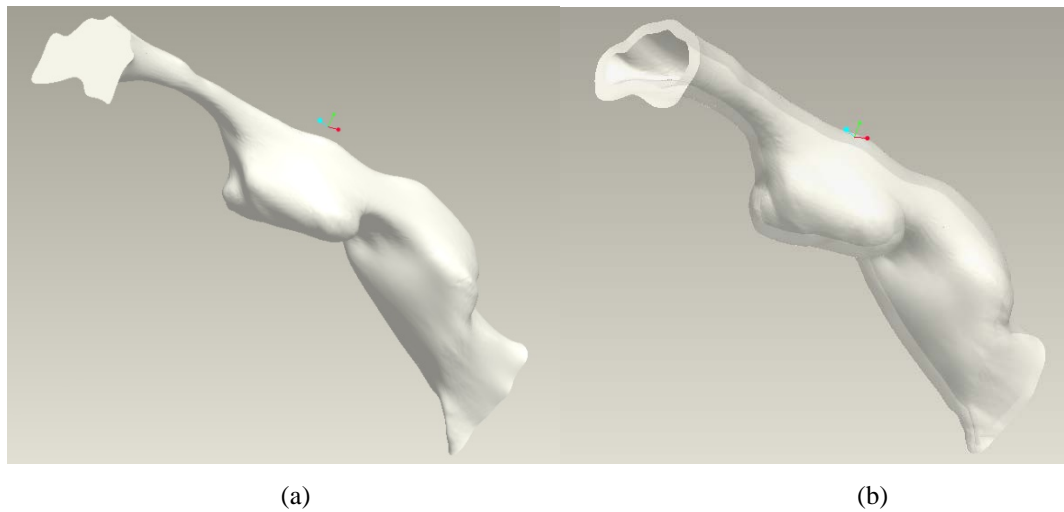
15

Figure 33 shows the comparison of the UA pressure drops of the smoothed and unsmoothed UA geometries under the same boundary condition and flow simulation

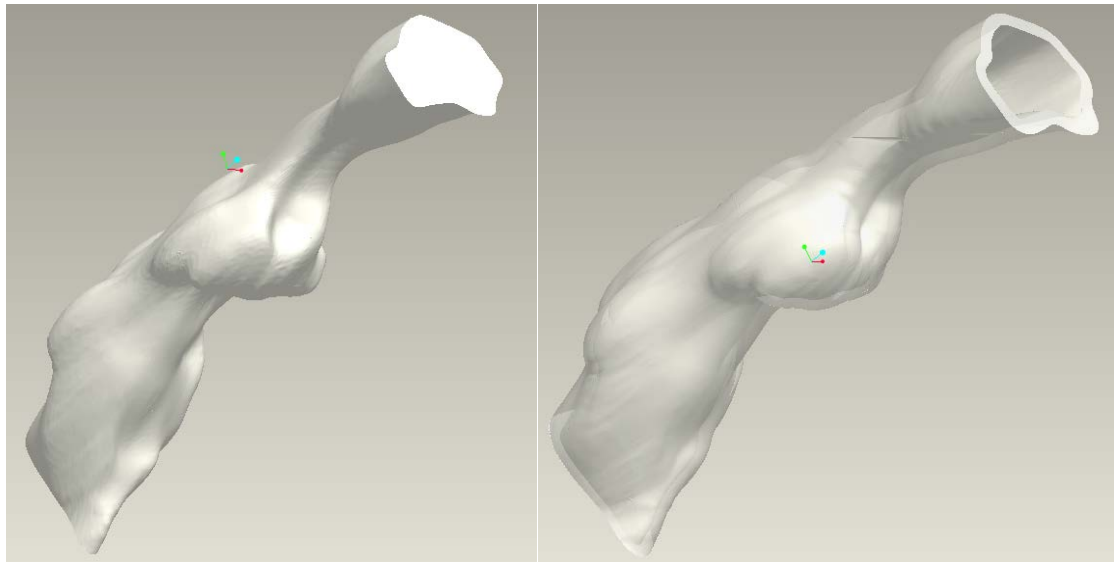
16

1 method. Although the pressure profile of the unsmoothed case appeared to fluctuate
2 more than the smoothed case, the patterns of the two pressure profiles were very similar.
3 Thus, the effect of this geometry smoothing on the structural deformation (the result of
4 FSI) should be acceptably minor.

5 For the fluid domains, the geometry was created as a solid volume of UA lumen. For
6 the UA wall domains, the outer surface of the model was generated by offsetting the
7 inner surface by 2 mm. Figures 34 and 35 present the final geometries of both domains
8 for pre- and post-treatment cases.



11 **Figure 34: Geometries of the (a) Fluid and (b) Solid Domain of Responder-1 in**
12 **Pre-treatment Condition**



1
2

(a)

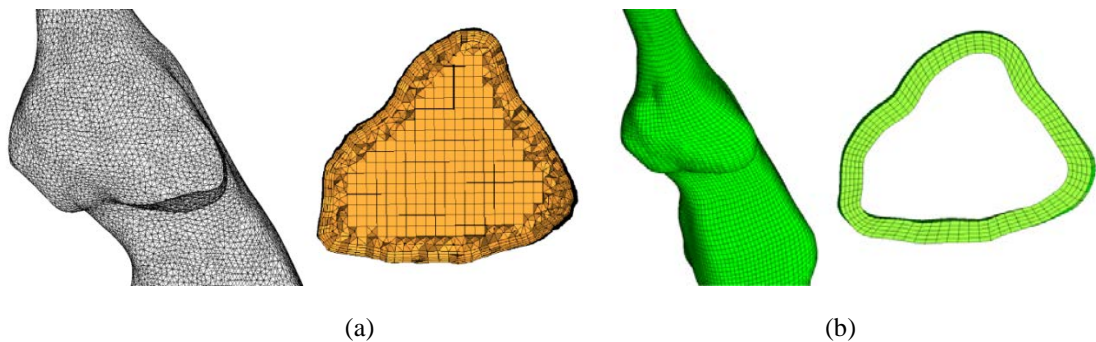
(b)

3 **Figure 35: Geometries of the (a) Fluid and (b) Solid Domain of Responder-1 in**
4 **Post-treatment Condition**

5 3.10.3 Computational Grid for the FSI Model

6 According to the mesh convergence study of the CFD model (Figure 25), a refined
7 unstructured hybrid volume mesh with 1.3 million elements was sufficient for the fluid
8 domain of the pre-treatment case. With the same method, a 1.6 million element
9 unstructured hybrid volume mesh was generated for the post-treatment fluid domain.

10 The structural domain of the UA was solved using FE method. According to a previous
11 study, the structured (mapped) elements have the advantages of better convergence and
12 computational efficiency when considering the FE method [76]. Thus, the UA solid
13 wall was constructed of structured hexahedral elements (Figure 36) in ICEM.



14
15

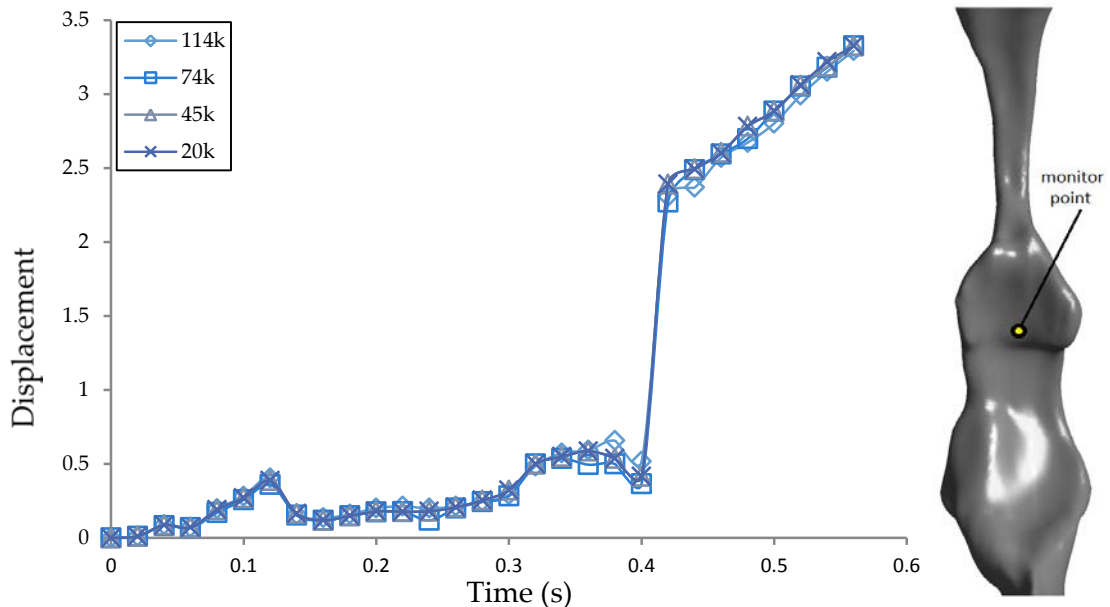
(a)

(b)

16 The cross-section views of each mesh are shown on the right.

17 **Figure 36: Computational Grids for (a) Fluid and (b) Solid Domains**

1 An additional grid convergence study was performed to determine the most efficient
 2 mesh density for the solid domain. The geometry of the pre-treatment case was selected
 3 and four meshes with increasing grid points from 20k to 114k were generated for it.
 4 Time-dependent FSI simulations were performed on these grids. The results indicated
 5 similar stress and strain distribution. To quantitatively compare the results, the
 6 displacement of a point located at the anterior wall of the oropharynx was plotted
 7 against the computational time steps (Figure 37). The results for all the meshes were
 8 very close, with the 20k mesh having an average deviation of 3.15% and a maximum
 9 deviation of 12.2% to the result of the finest 114k mesh. This indicated that the 20k
 10 hexahedral computational grid (solid 186, ANSYS) was adequate for the UA structural
 11 pre-treatment. Using the same method, a 27k hexahedral mesh (solid 186, ANSYS) was
 12 found to be sufficient for the post-treatment model.



13
 14 **Figure 37: Plot of the Displacement as a Function of Time of a Point Located at the**
 15 **Tongue Base Position 55 mm from the Inlet for Different Numbers of Mesh Points**
 16 **in the Solid Wall**

17 **3.10.4 Governing Equations for FSI**

18 As mentioned in Section 3.6, the estimated range of Re indicated UA to have a laminar
 19 or transitional flow. The k- ω SST model was proven to be appropriate to simulate the
 20 fluid domain [75]. The main governing equations of the fluid domain are expressed as:

$$\frac{\partial u_i}{\partial x_i} = 0 \quad 3-13$$

$$\rho u_i \frac{\partial u_j}{\partial x_i} = -\frac{\partial P}{\partial x_i} + \frac{\partial}{\partial x_i} \left[\mu \left(\frac{\partial u_i}{\partial x_j} + \frac{\partial u_j}{\partial x_i} \right) - \overline{\rho u'_i u'_j} \right] \quad 3-14$$

where u is the flow velocity, ρ is the fluid density, P is the fluid pressure, μ is the dynamic viscosity, and i and j represent the Cartesian coordinates. The fluid and solid domains were coupled through the stress tensor. The Cauchy stress tensor in an isotropic Newtonian fluid field was:

$$\sigma_{ij}^f = -p\delta_{ij} + 2\mu(\varepsilon_{ij} - \frac{1}{3}\varepsilon_{kk}\delta_{ij}) \quad 3-15$$

where σ_{ij}^f is the fluid stress tensor and ε_{ij} is the rate of the strain tensor, which is given by:

$$\varepsilon_{ij} = \frac{1}{2} \left(\frac{\partial u_i}{\partial x_j} + \frac{\partial u_j}{\partial x_i} \right) \quad 3-16$$

In the structural field, the governing equation of the linear elasticity is:

$$\frac{\partial \sigma_{ij}^s}{\partial x_j} + F_i = \rho \frac{\partial^2 D_i}{\partial t^2} \quad 3-17$$

where F_i is the body forces, D_i is the structural displacement, σ_{ij}^s is the solid stress tensor and t is time.

The Cauchy stress tensor in the structural field is defined as:

$$\sigma_{ij}^s = \frac{Ev}{(1+\nu)(1-2\nu)} \varepsilon_{kk}\delta_{ij} + \frac{E}{(1+\nu)} \varepsilon_{ij} \quad 3-18$$

where E is the Young's modulus, ν is the Poisson's ratio and ε_{ij} is the strain tensor (3-16).

1 The fluid and solid domain at the FSI boundary are matched by coupling the fluid
2 velocity and rate of structural displacement:

$$3 \quad u_i = \frac{\partial D_i}{\partial t} \quad 3-19$$

4 and the force equilibrium across the FSI interface:

$$5 \quad \sigma_{ij}^f \cdot n = -\sigma_{ij}^s \cdot n \quad 3-20$$

6 Both σ_{ij}^f and σ_{ij}^s are the stress tensors for the fluid and structural field, and n is the
7 normal vector outward of the FSI interface.

8 **3.10.5 Boundary Conditions for FSI Models**

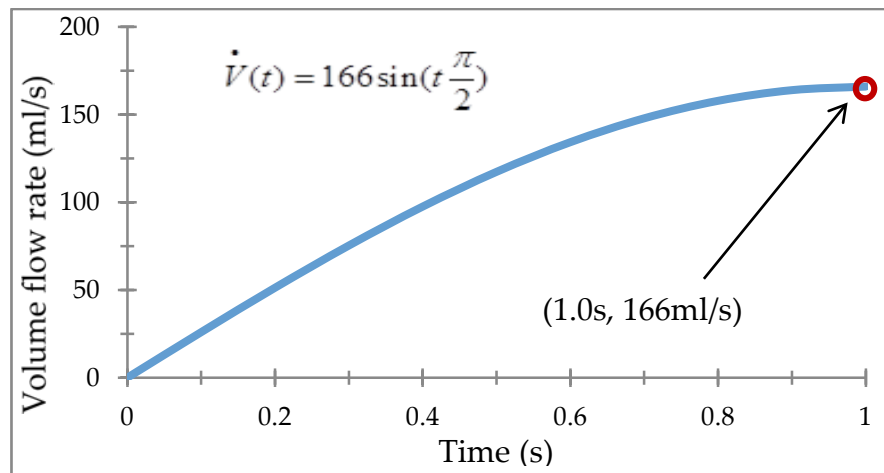
9 The fluid governing equations were solved in ANSYS CFX 13.0. The same boundary
10 conditions were used for cases with and without MAS fitted conditions. A time-
11 dependent inlet flow boundary was defined at the nasopharynx cross-section. The
12 inspiration flow was assumed to have a sinusoidal profile with a maximum flow rate of
13 166 ml/s (10 L/min) [27] occurring at one second (Figure 38). The time step was
14 determined from the Courant number. The Courant number, C_r , reflects the portion of a
15 mesh grid through which the fluid will traverse by advection in a single time step:

$$16 \quad C_r = \frac{\bar{v}\Delta t}{\Delta l} \quad 3-21$$

17 where Δl is the dimension of the grid, \bar{v} is the average linear velocity at that location
18 and Δt is the maximum time step size. A low C_r can avoid instabilities, improve
19 accuracy and reduce dispersion. The deforming mesh in the FSI simulations caused
20 difficulties in determining the C_r . The test run indicated that a $C_r \leq 10$ will lead to a
21 reasonable convergence performance. The maximum velocity in the UA fluid domain
22 was about 10 m/s. The range of grid edge length could vary from 0.41 mm minimum to
23 0.83 mm maximum. The average grid edge length was around 0.5 mm. The time step
24 was 5×10^{-4} s, which was calculated using Equation 3-21. The turbulence intensity was
25 specified as 10% and a static outlet pressure of 0 Pa was set at the vocal cord. The FSI
26 interface was a wall boundary with no-slip condition. The computational structural

1 solver ANSYS Mechanical 13.0 (ANSYS, US) was used to solve the UA structural
2 equations. The cross-sectional surface at the soft palate and vocal cord was fixed at all
3 degrees of freedom. An FSI boundary was defined at the inner surface of the UA wall
4 model.

5 In this study, the UA material was considered isotropic linear elastic, although human
6 soft tissues are normally described as nonlinear (hyper elastic). However, the
7 interpersonal variation of nonlinear tissue properties could result in great uncertainty in
8 the simulation result [77]. In addition, in-vivo measurement of the nonlinear material
9 data of UA tissue is still unavailable [78]. The simple and robust linear assumption of
10 UA material proved to have a remarkable level of accuracy in the UA structural analysis
11 during the validation of experimental data [62]. As a result, the UA tissue was defined
12 as a homogeneous elastic material that had a modulus of 7,540 Pa and Poisson's ratio of
13 0.45 [79].



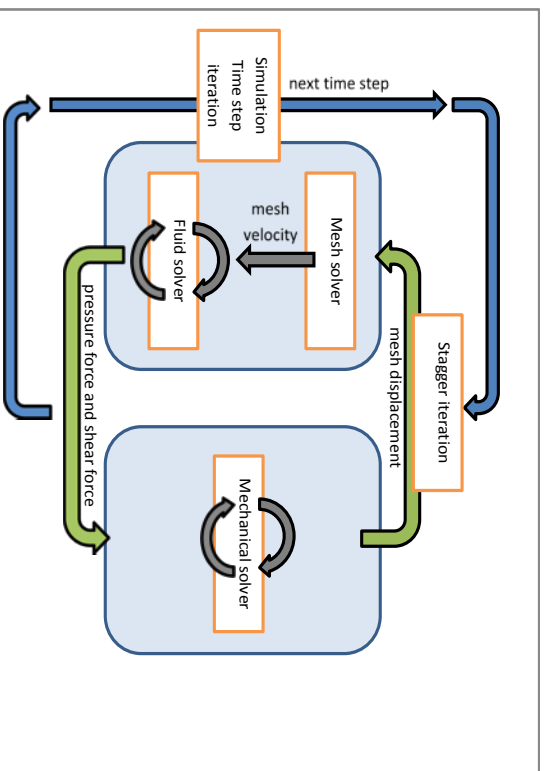
14
15

Figure 38: Sinusoidal Flow Profile of the Inspiratory Flow

16 3.10.6 FSI Coupling and Solving the FSI Model

17 With the use of an ANSYS Multi-field solver (MFX), three levels of iteration were
18 defined to couple the fluid and structural solvers (Figure 39). The convergence
19 iterations were individually established for two solvers, ensuring that the calculation of
20 both fields could reach the residual target in every iteration. To transfer the force and
21 structural deformation (heat transfer was not considered in this study), a staggered
22 iteration provided the interface to gather the data for distinct solvers. A time step-
23 controlled coefficient iteration developed the calculation progress based on the

1 simulation time. The FSI simulation of the pre- and post-treatment cases took about 20
2 days on a cluster computer that had 48 CPUs and 96 GB volume of random access
3 memory.



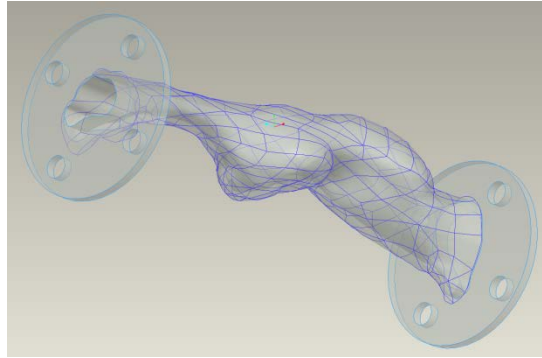
4
5 **Figure 39: Flowchart of Using MFX to Perform a Transient FSI Simulation**

6 **3.11 Experiment Method to validate the FSI Result**

7 In order to validate the FSI modelling method, physical experiments were conducted to
8 reproduce the UA collapse. The geometry, material properties and flow and structural
9 boundary conditions of the experiment UA model were chosen to match the FSI model.

10 **3.12 Design of the Flexible Experimental UA Model**

11 The flexible airway model was developed from the UA geometry of patient case
12 Responder-1 in pre-treatment condition. The model was designed using
13 Pro/Engineering 4.0. The geometry of the UA wall structure was identical to the solid
14 domain in the FSI simulation. Two soft flanges were added to the inlet and discharge to
15 connect the model with the external air supply system and seal the connection, like
16 gaskets. This CAD design was fabricated via STL apparatus (SLA) method with a
17 flexible resin. The most flexible SLA material available for rapid prototype was selected
18 for the UA model (Figure 40).



1

2

Figure 40: 1:1 STL Model of the Pre-treatment UA Geometry

3

3.12.1 Measuring the Material Property of the Flexible Experimental UA Model

4

Tensile tests were performed to determine the material properties of the SLA resin. The tensile stress was measured by using the Instron 5543 (LABEQ-300) (Figure 41), which is a small capacity universal testing machine particularly designed for biomaterials. It is a single column machine driven by one drive that is capable of testing in tension and compression up to ± 1 kN; however, in this study, a small yet precise load cell of ± 500 N was used. The test speed was kept to as low as 10 mm/min and the maximum test load was set to 400 N. The specimen shape was designed to comply with the Australian standard of tensile testing AS1397-2007. As the result, the Young's modulus (E) was calculated from the ratio of stress (σ) and strain (ϵ):

12

$$13 \quad E = \sigma / \epsilon \quad 3-22$$

14 and the Poisson's ratio (ν) of the SLA resin was determined from the transverse strain (ϵ_t) and longitudinal or axial strain (ϵ_l):

15

$$16 \quad \nu = \epsilon_t / \epsilon_l \quad 3-23$$

17

The tensile test was repeated 10 times, with a new specimen used each time. The final results of the material properties were averaged from these 10 measurements, and ended up being 325 kPa and 0.306 for the Young's modulus and Poisson's ratio, respectively.

18

19



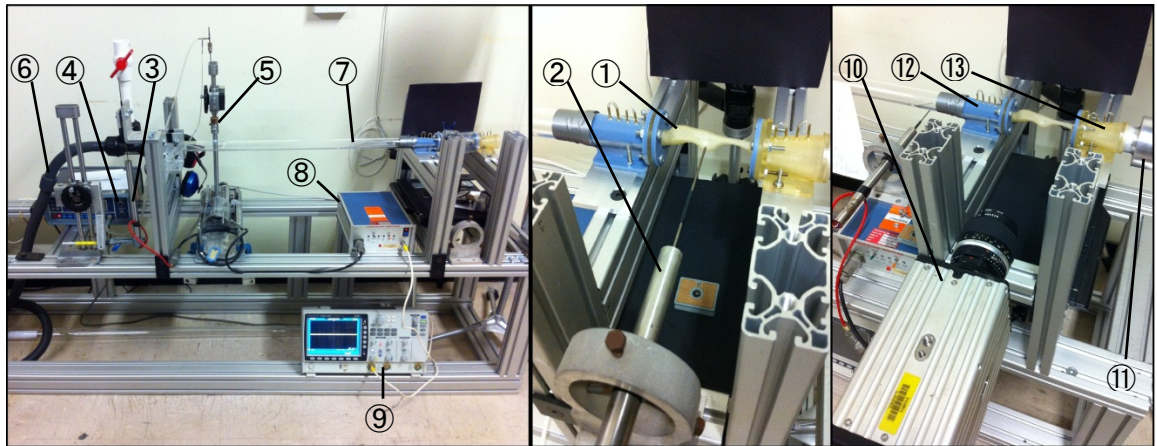
1

2 **Figure 41: Photographs of the Instron 5543 Mechanical Testing Machine Used to**
3 **Perform Tensile Tests of the Material Properties of the SLA Resin**

4 **3.12.2 Experimental Setup**

5 *3.12.2.1 Flow Supply and Regulation*

6 Figure 42 displays the experimental setup. The inlet and outlet transitional connections
7 were designed to minimise flow disturbance; thus, the uniform inlet flow boundary
8 condition in the CFD model could be reproduced. Pressure tapings were placed at each
9 connection to measure the static pressure of intake and discharge flow. A Pitot-static
10 tube was placed downstream 1,200 mm to the discharge connection to measure the flow
11 velocity in order to calculate the flow rate.



1

2 (1) SLA UA model, (2) LVDT sensor (Series 100, Trans-Tek Inc, US) attaches to the wall of the UA
 3 model, (3) The calibrating configuration of LVDT, (4) Digital manometer (FCO510, Furness Controls,
 4 UK), (5) Pitot-static tube, (6) Flow supply, (7) Flow developing pipe (1" × 1,400 mm), (8) Self-designed
 5 analog-digital converter (ADC), (9) Data storage oscilloscope (GDS-3000, GW Instek, Chinese Taipei),
 6 (10) Digital high-speed camera (XS-4, IDT, USA), (11) Aluminium alloy bell mouth, (12) Discharge
 7 transitional connection, (13) Intake transitional connection.

8

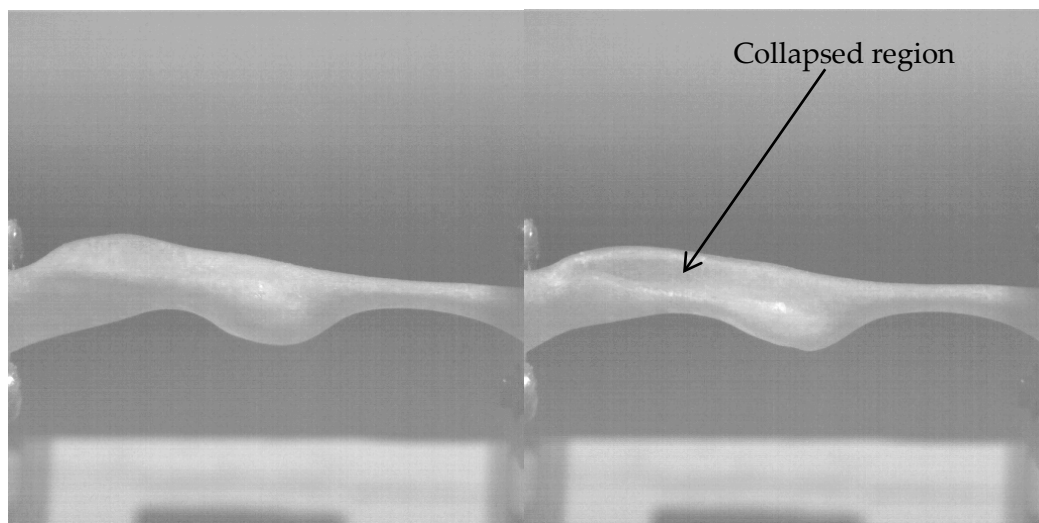
Figure 42: Experimental Setup for Validating the FSI Analysis

9

3.12.2.2 Measurement of the Wall Deformation

10

The motion of the airway wall was recorded with a high-speed camera (X-Stream 4,
 11 Integrated Device Technology, US). The sequence of the shuttering and image
 12 recording was digitally controlled by the software Motion Pro Studio (Integrated Device
 13 Technology, US) on a PC. The images were taken in the resolution of 512×512 pixels,
 14 with a recording speed of 100 frames per second (Figure 43).



15

16

Figure 43: Image of the Collapse Recorded by High-speed Camera: (a) UA Model

17

Un-deformed and (b) UA Model Fully Deformed

1 The upper and lower boundary of the UA wall could be extracted from the recorded
2 images via an imaging process function in Motion Pro Studio. These boundary lines
3 were useful indicators to demonstrate the collapsing process of the UA wall. By
4 matching the experimental and simulation results on these boundary lines, the ability of
5 the FSI to match with the experiments could be assessed.

6 The quantitative value of the UA deformation at a particular point was measured with a
7 linear variable differential transformer (LVDT) sensor (Trans Tech, US). The LVDT
8 sensor transferred the linear movement of the testing probe to analog voltage data. An
9 ADC was used to filter and convert the analog signal from the LVDT to digital data.
10 The digital data were then received and interpreted with a data storage oscilloscope
11 (GDS-3000, GW Instek, Chinese Taipei). The accuracy of the LVDT sensor was 0.5%
12 of the full scale (40 mm), which was 0.2 mm. It was calibrated by using a magnetic
13 digital height gauge (Mituyoyo 192-661, 600 mm full scale) that had a measuring
14 accuracy of 0.01 mm.

15 The LVDT was placed horizontally, pointing to the left side of UA model. The location
16 of the measuring point was the area that seemed to have the maximum deformation (left
17 side of the posterior oropharynx, 63 mm from the inlet). The probe head of the LVDT
18 had a diameter of 2.5 mm, which was unable to precisely measure the wall deformation
19 at a point. A needle with a diameter of 0.3 mm was attached to the head of the probe.

20 The material property of SLA resin was found to have a higher rigidity (325 kPa) than
21 human tissue (7.54 kPa), which was applied in the FSI modelling. Thus, in the
22 experiment, a much higher flow rate of 32 L/min was generated to produce the collapse
23 of the UA model. This meant that the experiment was unable to represent the exact
24 conditions of flow and solid structure in the FSI model. However, the aim of this
25 experiment was to validate the FSI modelling method. Thus, an additional FSI
26 simulation was performed with the same material and boundary conditions as the
27 experiment.

28 **3.13 Summary**

29 The methodology of this study was designed to model the UA flow and UA wall
30 deformation via computational modelling. It sought to analyse the mechanism of UA
31 collapse that affects UA flow. By performing multiple case CFD studies, this

1 methodology was able to establish a correlation between the flow properties and the
2 treatment result. Physical validation experiments were conducted to validate the CFD
3 and FSI modelling method. The next chapter will compare the pressure profile of the
4 UA flow and the pattern of wall deformation measured in the experiments with the
5 simulation results.

6

Chapter 4: Results: Pressure and Velocity Field

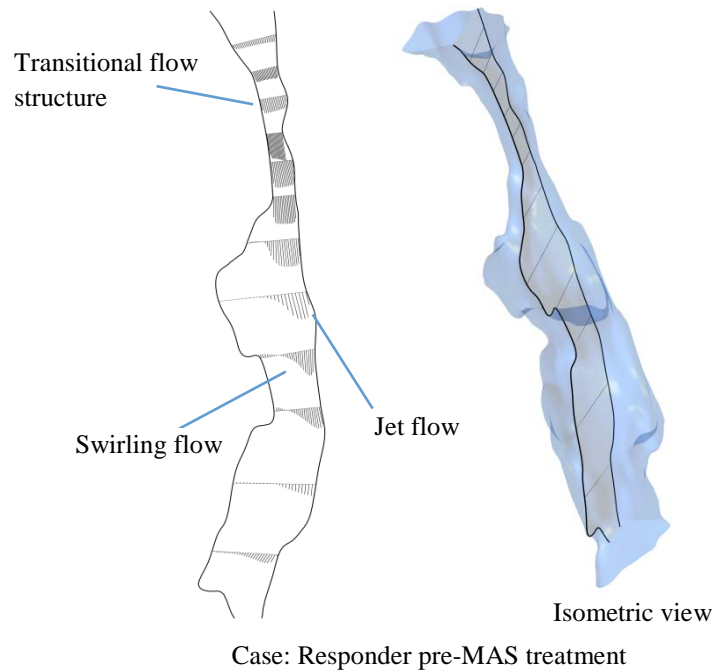
4.1 Introduction

This chapter presents the results of the CFD modelling of seven patients' airways. These CFD UA models were validated via a comparative study of numerical and experimental UA pressure profiles. Examining the group UA velocity and pressure profiles confirmed that the flow properties (such as pressure drop) correlated with the treatment response. A treatment prediction model was developed based on the percentage changes of the minimum pressure in UA and the AHI changes. Sections 4.4 to 4.7 have been published in the paper 'Computational Fluid Dynamics for Assessment of Upper Air Way Response to Oral Appliance Treatment in Obstructive Sleep Apnea' [75].

4.2 Validation of the CFD Results

4.2.1 Comparison Experiments with CFD

The experiment was performed on a 1:1 rigid UA model of the case Responder-1. The UA pressure profile was used in the comparison between the experimental and computational results, as it could be accurately obtained in the experiments. The UA flow profile was predicted by the CFD result shown in Figure 44. Similar types of flow were expected in the experimental model. The laminar to transitional flow dominated the velopharyngeal flow field. An unstable flow structure (such as 3D flow recirculation) was found in the anterior region of the oropharynx and hypopharynx. These flow recirculation regions would have significant pressure fluctuation, which increased the error in pressure reading. In the region close to the UA posterior wall, high-speed jet flow was constantly indicated. Therefore, the static pressure profile was measured along the back of the UA wall, and these readings were expected to be stable and accurate.

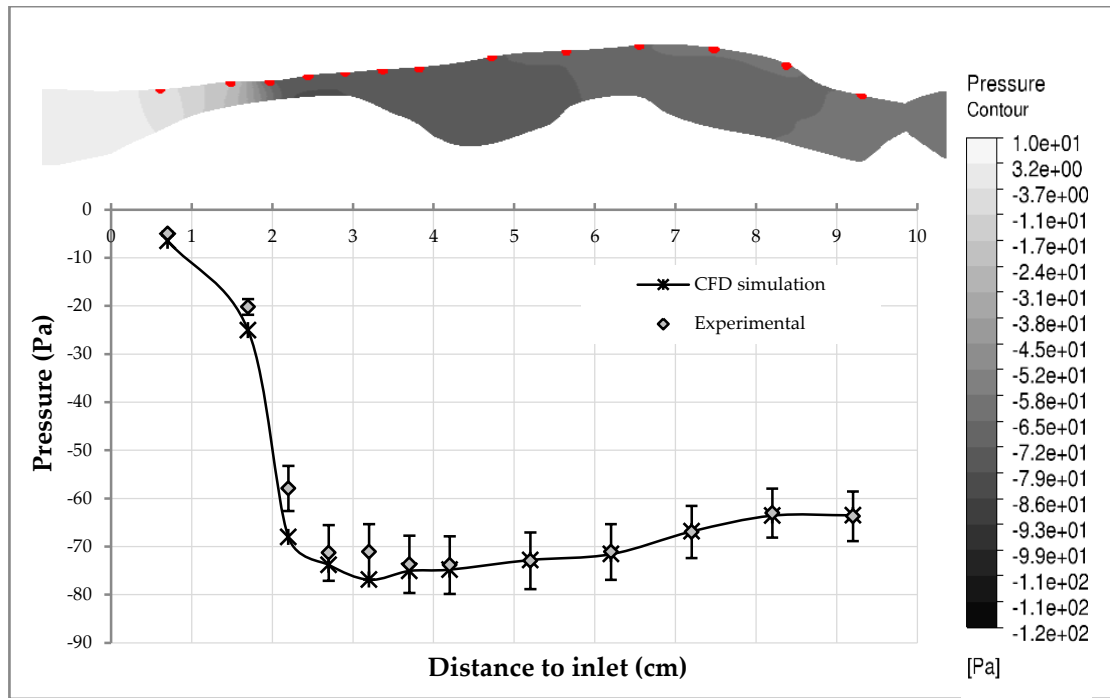


1
2

3

Figure 44: Velocity Vector on the Mid-sagittal Plane of the CFD Result

4 As can be seen in Figure 45, the CFD results were a close match to the experimental
 5 results. The highest discrepancy was located at the pressure port in the velopharynx, 22
 6 mm from the inlet. The CFD model over-predicted the UA negative pressure by 9 Pa,
 7 which was about 17% of the experimental pressure recording. The experimental
 8 pressure values fluctuated more in the velopharyngeal flow-restricted area. There was
 9 only about 5.8 Pa difference between the computational and experimental data on the
 10 lowest pressure in the airway model. In the oropharynx and larynx, the observed
 11 turbulent jet flow and unsteady swirling flow played a more important role than the
 12 transitional flow in the flow field. The CFD simulation could precisely predict the
 13 pressure profile. Although there was a minor over-prediction of pressure drop in the
 14 nasopharynx - velopharynx area, the applied SST turbulence model performed well at a
 15 complicated flow field in the oropharynx and larynx. Overall, the CFD result of the UA
 16 pressure profile was validated by the experimental pressure data.



1

2 Top figure shows the pressure contours plotted at plane $x = 7$ mm, which was the middle cross-section of
 3 the airway model. Graph shows the measured and simulated pressure along the length of the airway.

4 **Figure 45: Validation of CFD Method by Comparing the Wall Pressure**
 5 **Distribution**

6 **4.2.2 The Uncertainty in Experimental Results**

7 The uncertainty in the experimental results arose from equipment errors—including
 8 calibration of the Pitot-static tube and the digital manometers, and the geometrical error
 9 of the UA model—and human errors, such as reading errors and time-averaging error,
 10 and misalignment of the probe of the Pitot-static tube to the flow.

11 *4.2.2.1 Pitot-static Tube Errors*

12 The Pitot-static tube measured the stagnation pressure at the head of the probe and the
 13 static pressure at the side of the probe. In this study, the duct velocity had a maximum
 14 value of 0.52 m/s, with the error due to air compressibility neglected. Another
 15 uncertainty in the static pressure measurements was associated with the locations of the
 16 static tube tapings. The Pitot tube probe had a diameter of 2 mm (relative to a duct
 17 diameter of 25.4 mm), so the blockage effect of the tube to the duct flow could be
 18 ignored. Pressure readings can be affected by boundary flow if the Pitot tube is placed
 19 within a distance of 10 times the tube diameter. The tube was located at the centre of the

1 1 inch discharge pipe, which meant it was about 12 mm to the pipe wall. The estimated
2 error from boundary flow effect to pressure reading was less than 1%.

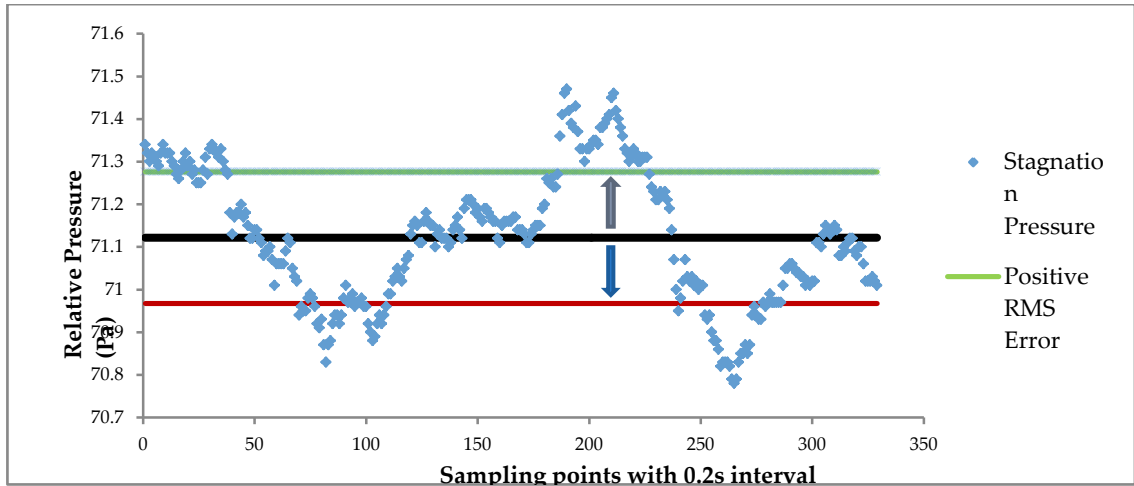
3 In addition, misalignment between the flow direction and probe head could also
4 introduce error in both the total pressure and static pressure readings. The maximum
5 possible yaw and pitch angle of probe head to flow direction was 3°. The combined
6 error due to yaw and pitch angle misalignment was less than 0.5% [80].

7 *4.2.2.2 Manometer Errors*

8 The same manometer was used in this experiment (FCO510, Furness Controls) to
9 measure the duct flow rate and UA static pressure, but different scales were selected.
10 The manometers were fully calibrated. The stated equipment measurement uncertainty
11 was 0.25% of the reading. This error would be higher when the reading was too close to
12 zero. Other effects could vary the readings, such as the fluctuation of room temperature
13 (0.05% of full measuring scale per 1°C from 0°C) and ambient pressure; however, their
14 effect was very small ($\varphi < 0.5\%$).

15 *4.2.2.3 Time Averaging*

16 Approximately $\pm 1.5\%$ fluctuation of the pressure reading was observed during steady
17 flow. In this experiment, every pressure reading was measured 10 times with a 40-
18 second duration for each time. Thus, the pressure readings were averaged first over 40
19 seconds, and then over 10 sets of the results. These averaged values represented the
20 average pressures, rather than the instantaneous pressures. The standard deviations on
21 the readings were taken as a part of the errors (see Figure 46).



1
2

RMS = root mean square, which is also the quadratic mean.

3 **Figure 46: Time Variation of Pressure Readings in Manometers—Single Result Set**

4 *4.2.2.4 Geometry Tolerance*

5 The high-definition rapid prototyping method has a tolerance from 0.02 to 0.085 mm.
 6 Here, the maximum error of 0.085 mm could result in a 4.4% change in the area if
 7 located in the minimum cross-section of UA, which had a hydraulic diameter of 4.6 mm.
 8 The average flow velocity would be changed by geometric error. Therefore, the
 9 maximum error on velocity was 3.7%. Based on Bernoulli's principle, the changes in
 10 pressure, Δp , and velocity, Δv , can have a relationship of $\Delta p \propto \Delta v^2$, with the
 11 assumption that the potential energy term remains the same. As a result, the 0.085 mm
 12 variation in geometry would finally result in a maximum 7.6% error in pressure.

13 *4.2.2.5 Overall Error*

14 As a result, the experiment errors can be listed as 1.5% error for the Pitot tube, 1.75%
 15 error for the manometer, 1.5% error for time averaging, and a maximum of 7.6% for
 16 geometry error. Since all the above errors are independent (uncorrelated), the overall
 17 error of pressure measuring was estimated as:

18
$$Error_{total} = \sqrt{\sum_{i=1}^n Error_i^2}$$

19 which becomes: $Error_{total} = 8.1\%$.

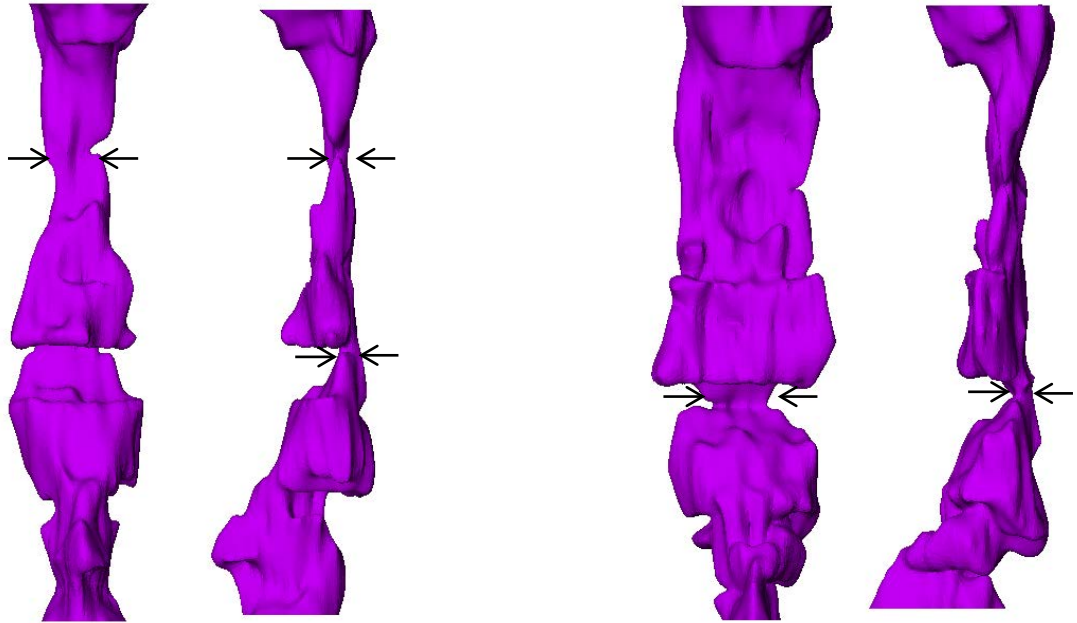
1 **4.3 Geometrical Changes before and after MAS Treatment**

2 The important features of the airway geometry were quantified by measuring the
3 volume, cross-sectional area and size in the lateral and anterior-posterior distances.
4 Table 3 lists the changes of these geometry features, which were induced by applying
5 the MAS. Since the original size of the airway was different for all patients, the table
6 gives the changes in airway dimensions as a percentage of patients treated with MAS,
7 relative to the untreated dimensions.

8 **4.3.1 Restriction in the UA**

9 The velopharynx is considered the most critical region along the whole UA structure in
10 terms of collapsibility [49, 81]. The soft palate, posterior wall of the UA and
11 surrounding tissues form a bottleneck in the air pathway. The location of UA restriction
12 may be able to indicate the site of UA collapse, since a low pharyngeal pressure is
13 formed in this area and high aerodynamic force could be generated on the surrounding
14 UA wall [22]. Henke et al. found that subjects who had oropharyngeal closure could
15 receive better treatment outcomes from MAS than subjects who had velopharyngeal
16 closure [82]. However, the geometry data in this study did not establish an obvious
17 linkage between the site of restriction and treatment success. Five of seven cases
18 appeared to have a velopharynx restricted significantly more than the oropharynx. The
19 partial responder and Failure-1 (Figure 47) had the minimum cross-sectional area at the
20 oropharynx.

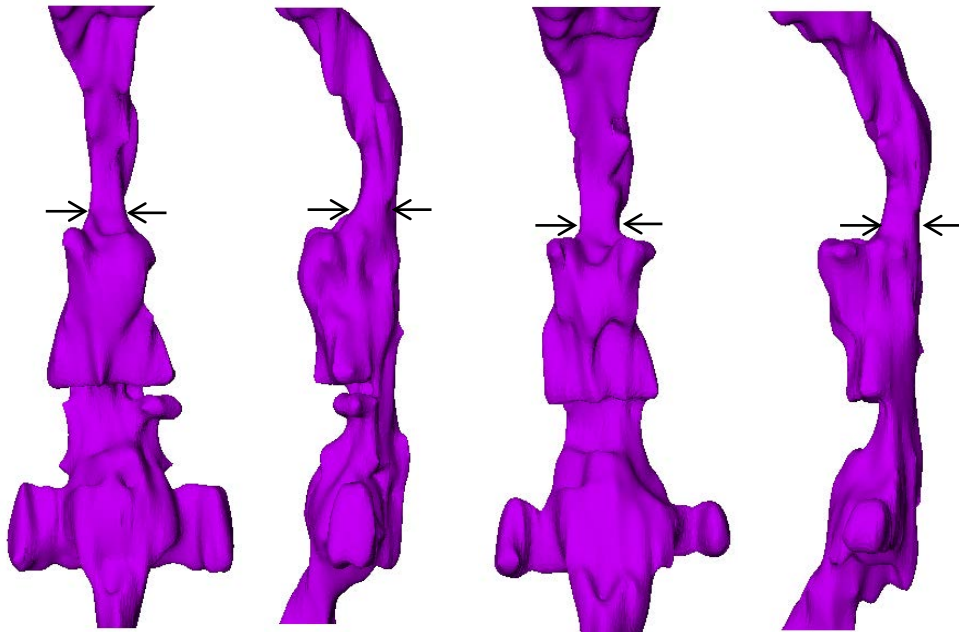
21



Pre-treatment

Post-treatment

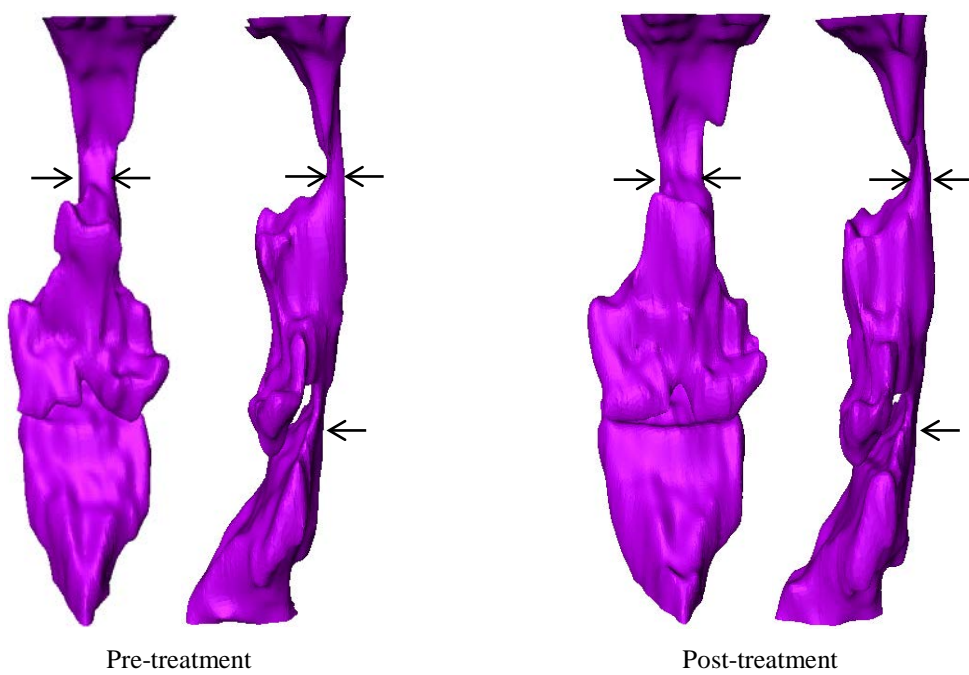
(b) Responder-2



Pre-treatment

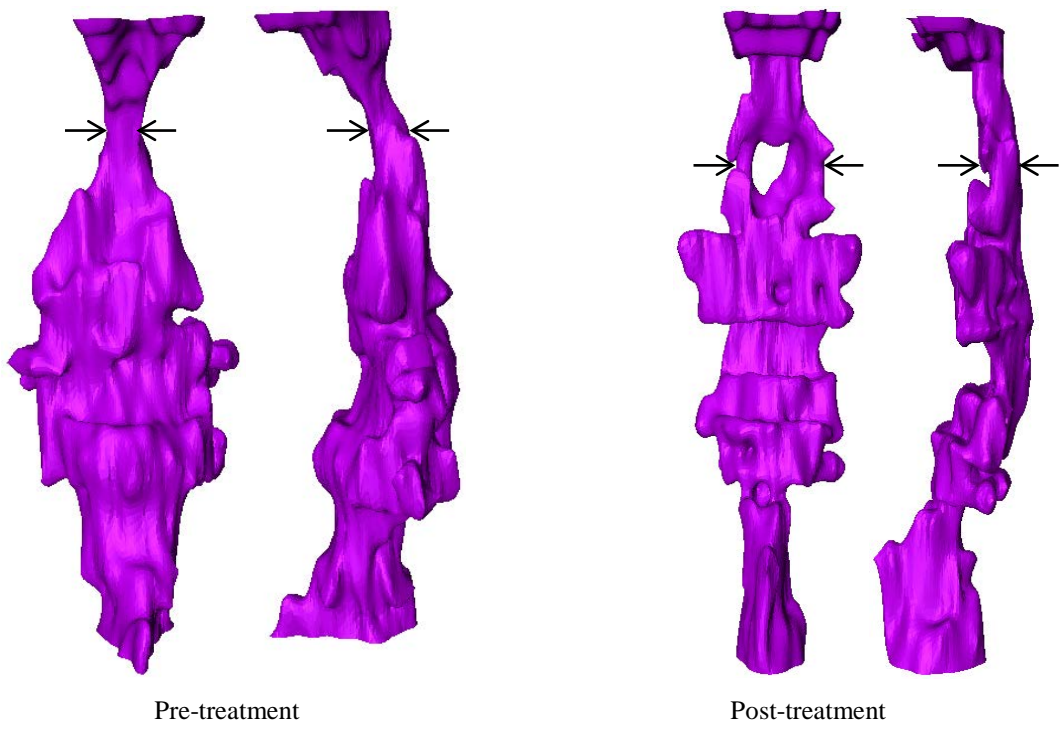
Post-treatment

(c) Responder-3



1
2
3

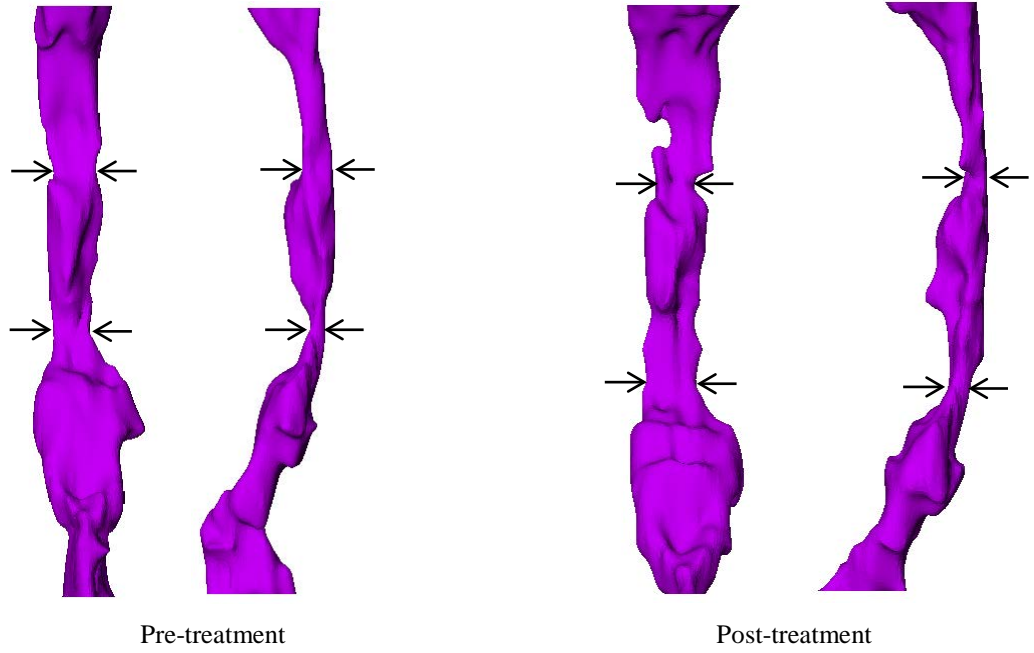
(d) Partial Responder



4
5
6

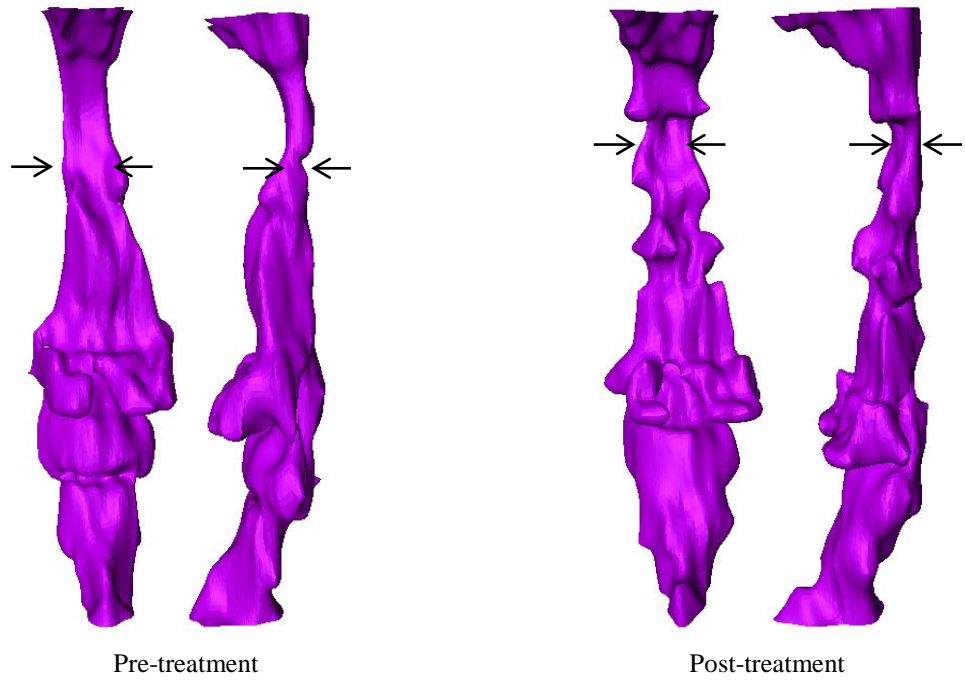
(e) Non-responder

1
2
3



(f) Failure-1

4
5
6



(g) Failure-2

7

Note: The arrows indicate the restricted regions in the UA.

8

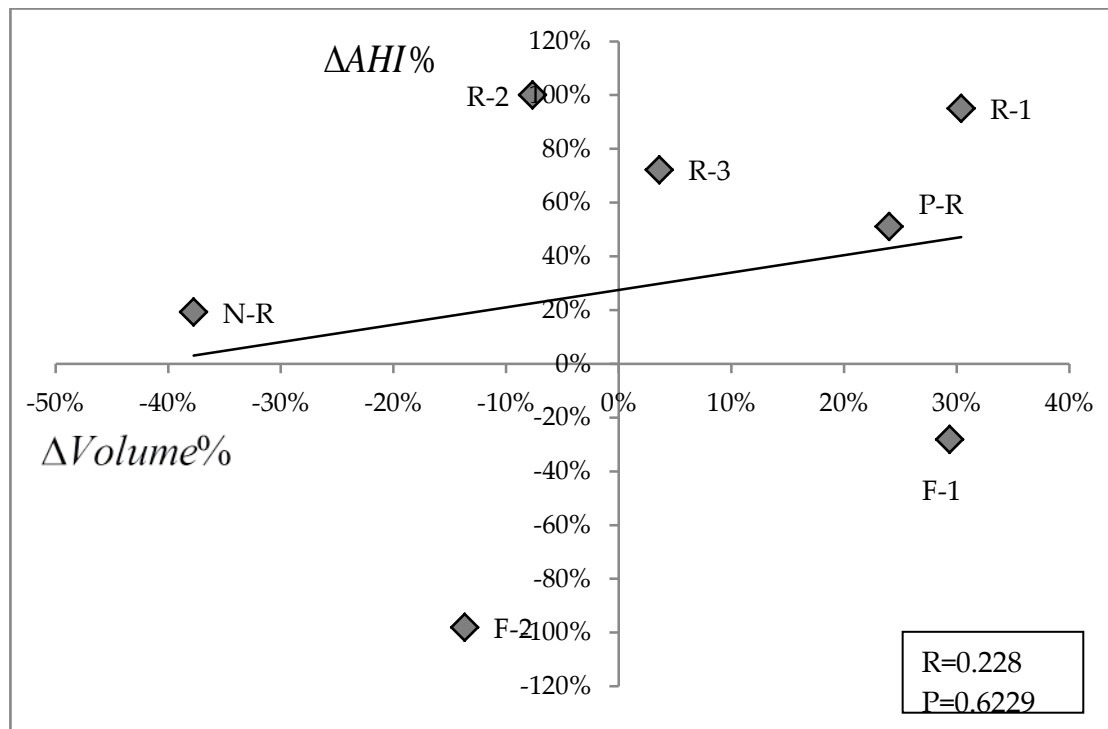
Figure 47: Amira Reconstructed 3D Images of the UA Geometry of Seven Patient

9

Cases before and after MAS Treatment

1 **4.3.2 The Changes of UA Geometry by MAS**

2 For all patients, the MRI scan showed that the lower mandible was successfully
 3 protruded by the MAS. This protrusion produced some increases and some decreases in
 4 the airway volume by varying magnitudes. However, in contrast to the findings of De
 5 Backer et al. [59], there was no strong relationship found between the change in UA
 6 volume and AHI (Figure 48).



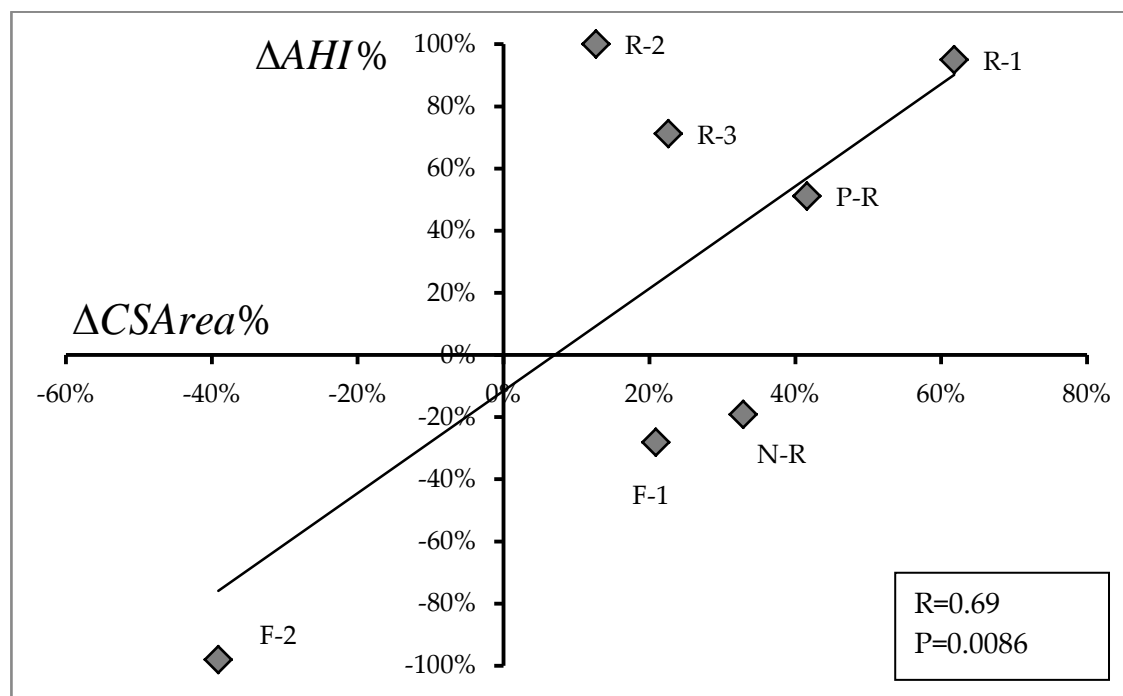
7
 8 Note: R = responder, P-R = partial responder, N-R = non-responder, F = failure, R = Pearson's correlation
 9 coefficient, P = two-tail probability.

10 **Figure 48: Correlation between the Percentage Changes in the UA Volume**
 11 **(ΔVolume%) and AHI (ΔAHI%) before and after MAS Treatment**

12 Chan et al. found no obvious difference in the UA volumetric and structural change
 13 between responders and non-responders to MAS treatment [69]. In contrast, Bosshard et
 14 al. observed that MAS treatment usually increased the velopharyngeal area in the lateral
 15 dimension. Subjects who had greater improvement in velopharyngeal size were more
 16 likely to receive a better treatment result [83]. The current study found that some
 17 responder cases, such as Responder-2, achieved a significant increase in lateral
 18 velopharyngeal dimension; however, this increase was also observed in the non-
 19 responder and Failure-1. The velopharynx of these two subjects increased in the lateral
 20 dimension, but resulted in anterior-posterior closure. The collapse of the soft palate

1 towards the posterior UA wall may explain the reason for the treatment's lack of
 2 success. Some responder cases, such as Responder-3, had no obvious change in
 3 velopharyngeal geometry after treatment. This emphasises that the change in
 4 velopharyngeal dimension may not be an efficient index to predict the treatment
 5 outcome of MAS.

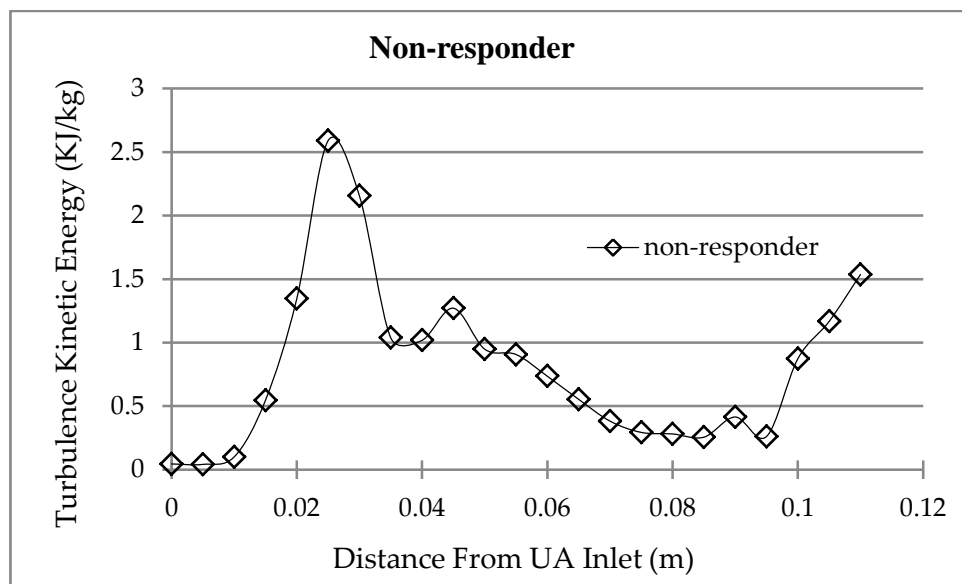
6 Overall, the MAS treatment was successful in treating OSA, partly by effectively
 7 increasing the UA volume. The enlargement in the cross-section was more likely to
 8 occur in the lateral direction than in the anterior-posterior direction. However, there was
 9 no strong correlation between the above geometrical features and the treatment response,
 10 since the geometrical changes were not proportional to the AHI changes. The minimum
 11 cross-section was found to be the best geometrical parameter, as indicated by Figure 49,
 12 showing the change in the minimum cross-section area plotted against AHI changes. As
 13 can be seen, there appeared to be a relatively moderate correlation between the change
 14 in this area and the change in AHI. Figure 49 indicates that cross-sectional area
 15 enlargement could result in non-responders and failures to MAS treatment. The 69%
 16 correlation was not stronger enough to clearly predict the treatment response.



17
 18 Note: R = responder, P-R = partial responder, N-R = non-responder, F = failure, R = Pearson's correlation
 19 coefficient, P = two-tail probability.

20 **Figure 49: Correlation between the Percentage Changes in the Minimum Cross-**
 21 **sectional area ($\Delta CSArea\%$) and AHI ($\Delta AHI\%$) before and after MAS Treatment**

1 The minimum cross-section areas were varied in lateral and anterior-posterior
 2 dimensions and shape. An increase in the area may not lead to relief of OSA. The non-
 3 responder case had a 32.9% enlargement in the minimum cross-section area. There was
 4 a 165.2% increase in the lateral direction; however, the UA collapsed anterior-
 5 posteriorly. The velopharynx separated into two narrow pathways with increased flow
 6 speed (Figure 51-e). As a result, the Reynold's number was enlarged dramatically from
 7 600 to over 4,000 in this area, and the flow turbulence largely increased (Figure 50), so
 8 as the negative air pressure.



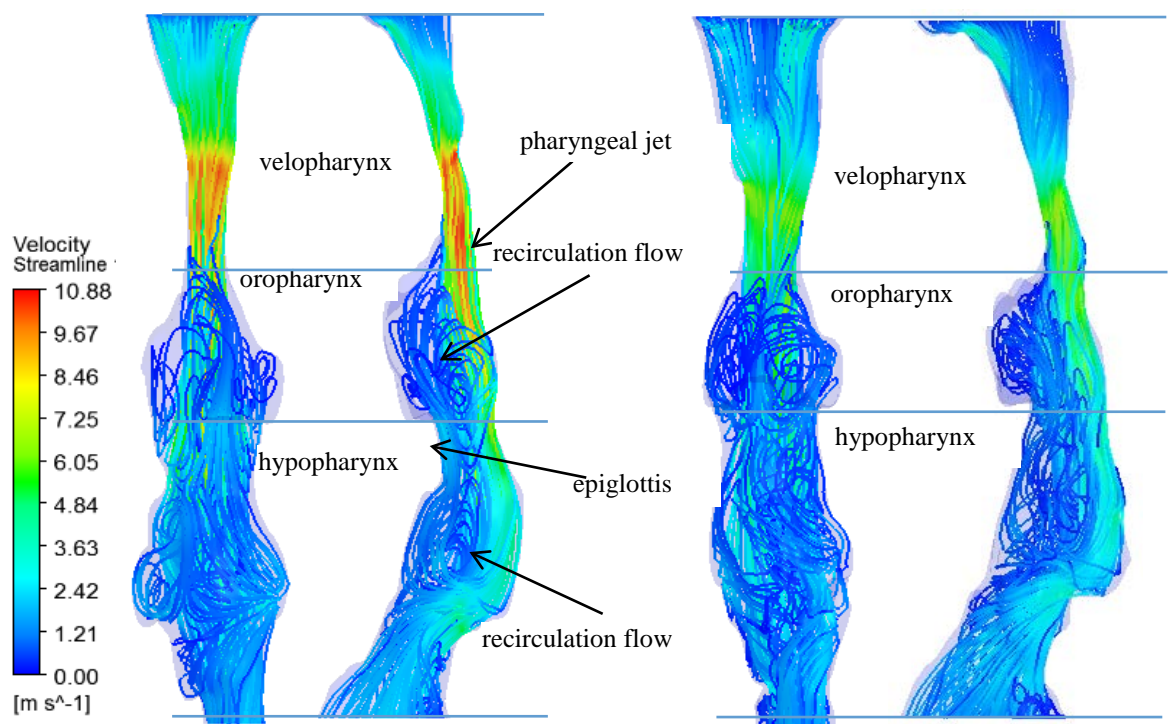
9
 10 **Figure 50: Maximum Turbulence Kinetic Energy Profile of Non-responder Post-**
 11 **treatment Case**

12 The turbulence kinetic energy increased from 0.045 KJ/kg at the UA inlet to 2.594
 13 KJ/kg at the separation of UA geometry. The pressure profile can be found in Figure 55.
 14 The increase of the cross-section area could not directly lead to a reduced pressure drop
 15 and the turbulence of the airflow in the velopharynx. The MAS could widen the
 16 velopharynx of this non-responder; however, the collapsed anti-posterior wall largely
 17 increased the irregularity of the velopharyngeal geometry by creating an 'obstacle' to
 18 force the air to travel sideways. Despite the increased velopharynx cross-section area
 19 (32.9%), the interruption and separation of UA flow stream by velopharyngeal
 20 geometry resulted in a high turbulence and large pressure drop. Thus, the constancy of
 21 the UA flow streamline and regularity of the UA geometry is another important factor.
 22 A shape parameter that took into account the geometric regularity was intended to help

1 predict the response, but none was found. However, this study concluded that the
2 change in flow associated with geometrical change would affect the treatment outcome.

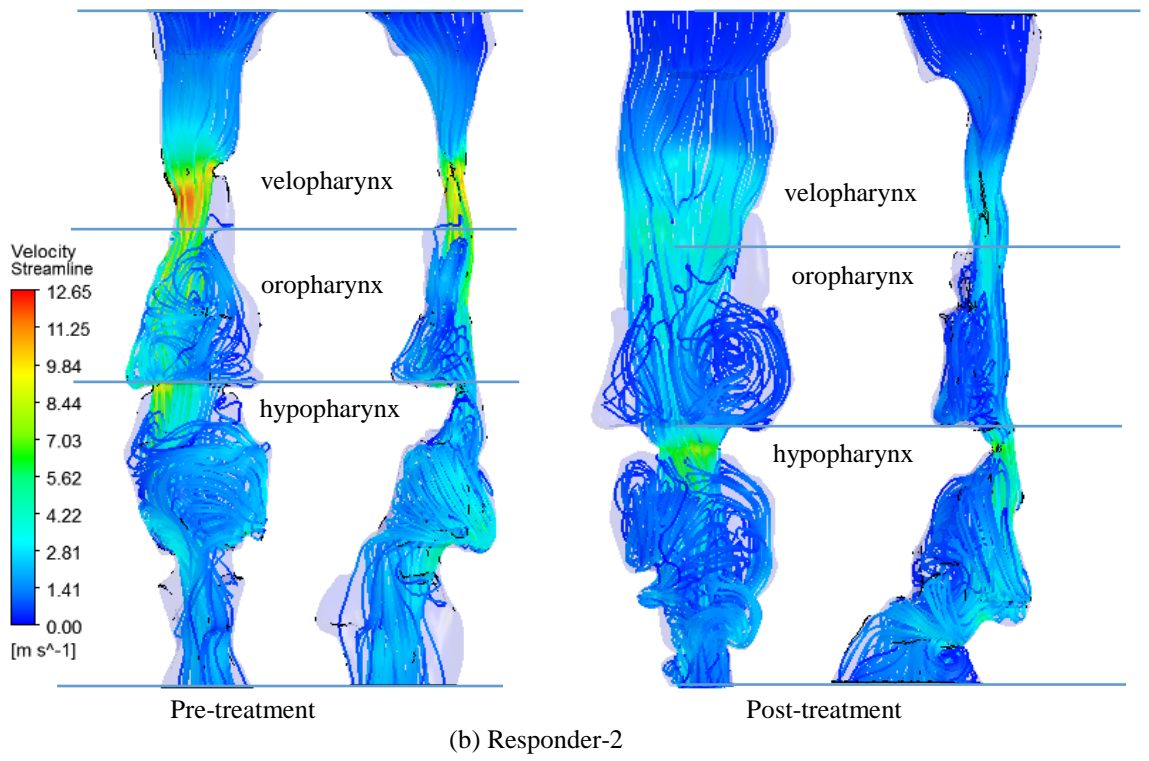
3 **4.4 The Multi-case CFD Result: Flow Patterns**

4 In order to determine the effect of geometry on the flow field, streamline plots are
5 shown in Figure 51. The results indicate a similar flow pattern in most cases. The
6 transition between the constricted airway at the velopharynx and sudden expansion in
7 the oral cavity formed a significant adverse pressure gradient in the oropharynx. Thus,
8 the flow recirculation and reversed flow occurred in this region. Similarly, a region
9 exists where the epiglottis narrowed the airway between the oropharynx and
10 hypopharynx. The airflow was constricted around the uvula. It then attached to the
11 posterior wall of the oropharynx and hypopharynx before travelling through the vocal
12 cord. This flow pattern has been described as the ‘pharyngeal jet’ [50]. There were
13 strong recirculation flows in the oral cavity and the region near the root of the tongue
14 and the epiglottis. In many cases, such as for Responder-1, this swirling flow was
15 generated from the flow separated in the hypopharynx and then travelling up to the
16 oropharynx.

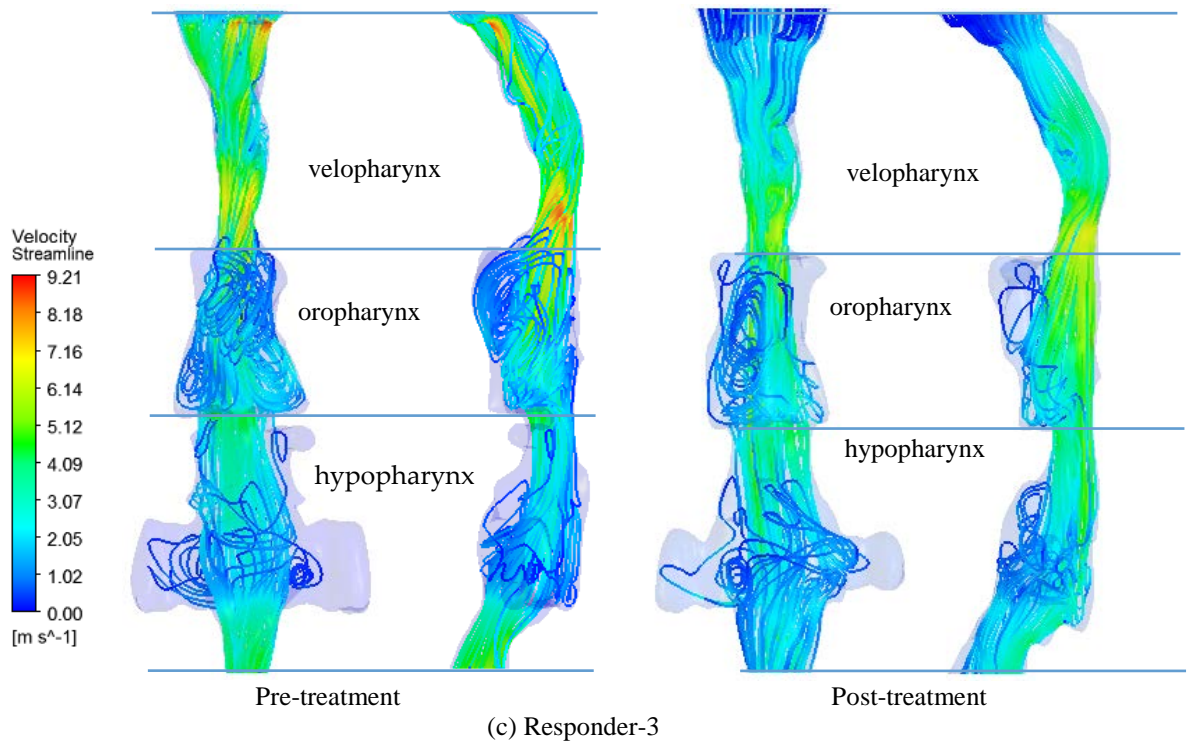


17
18
19

(a) Responder-1

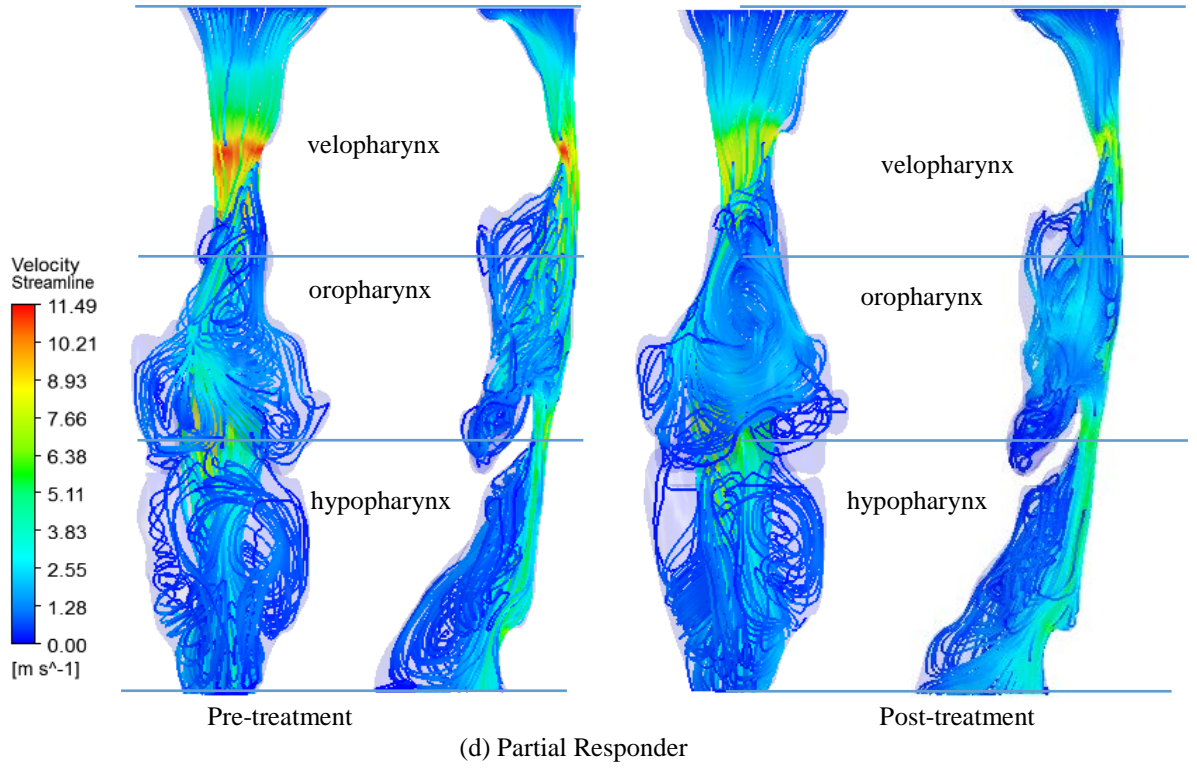


1
2
3
4

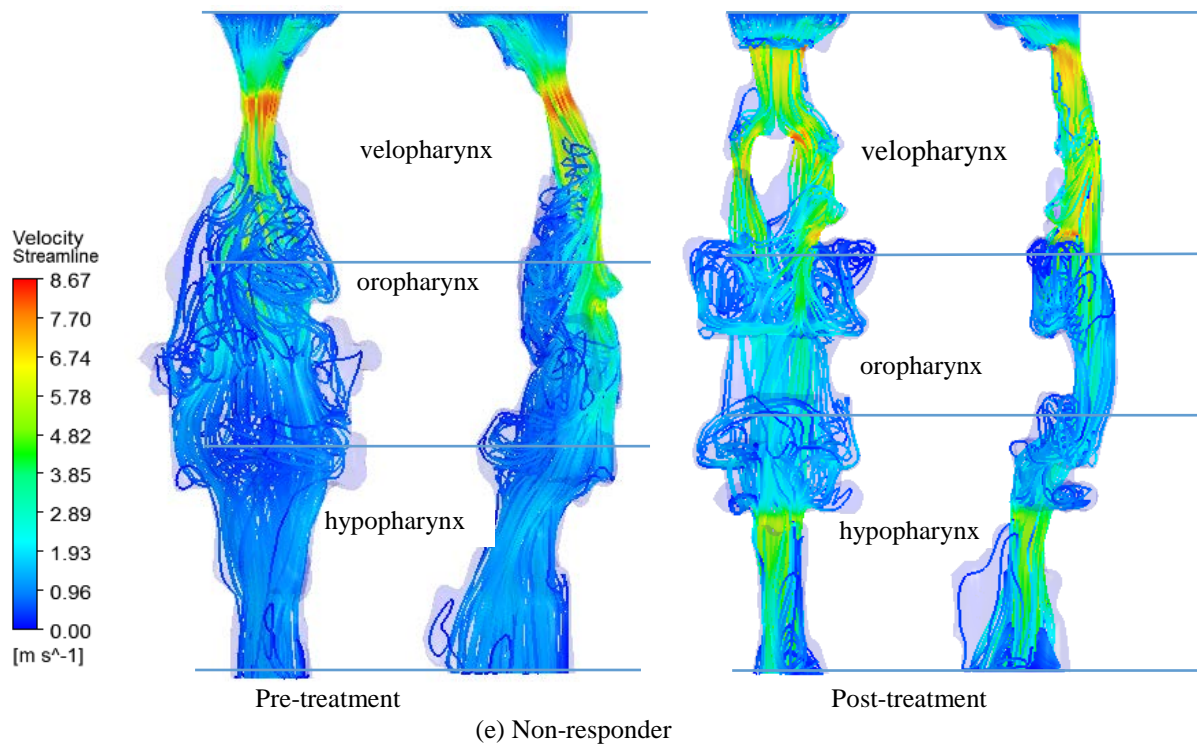


5
6
7

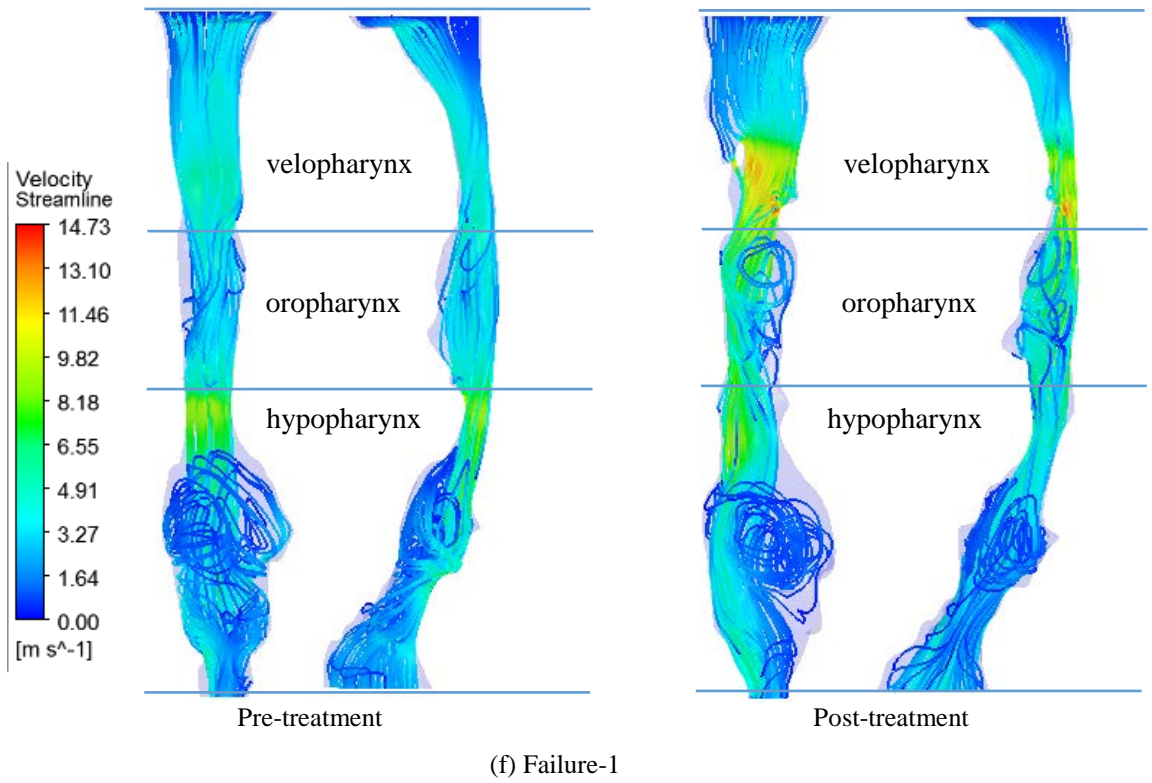
1
2
3
4



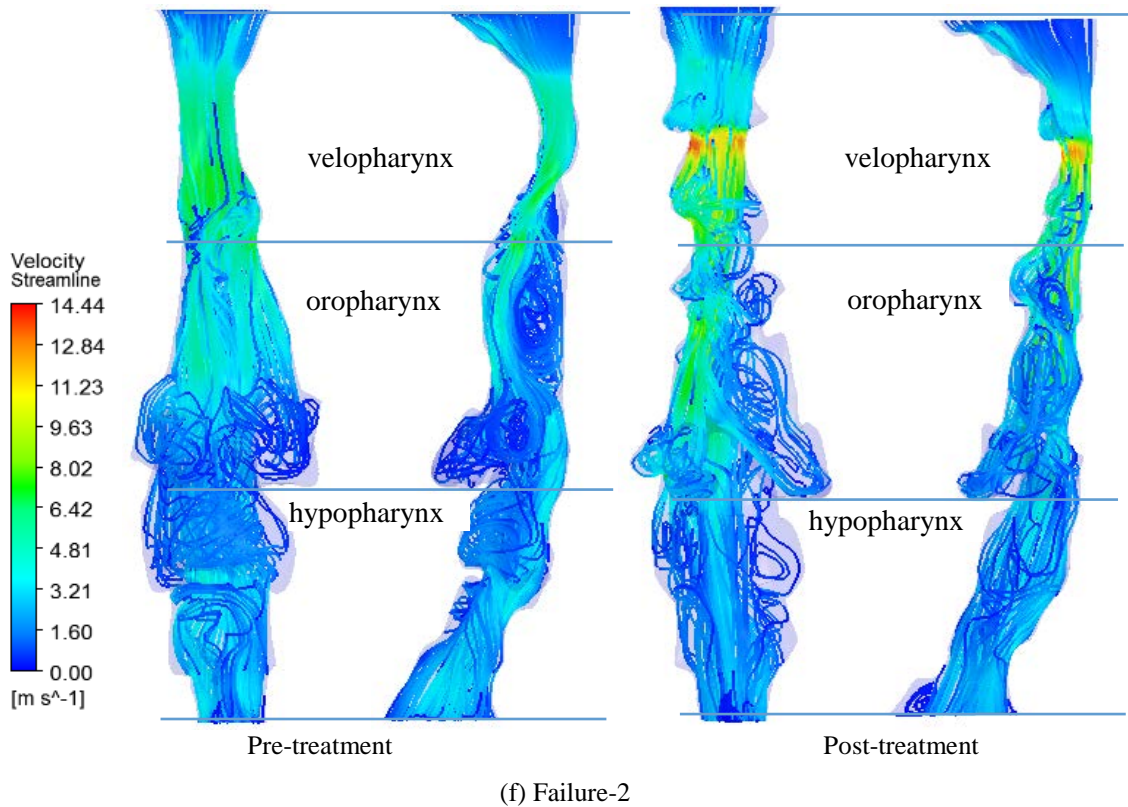
5
6
7



1
2
3
4



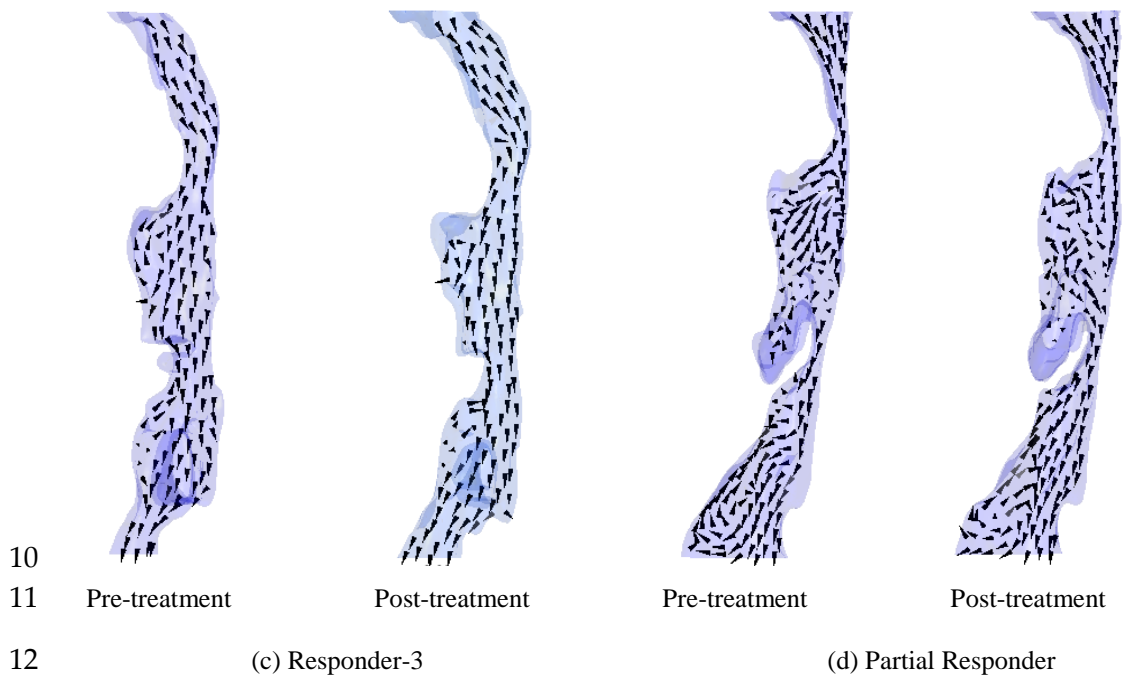
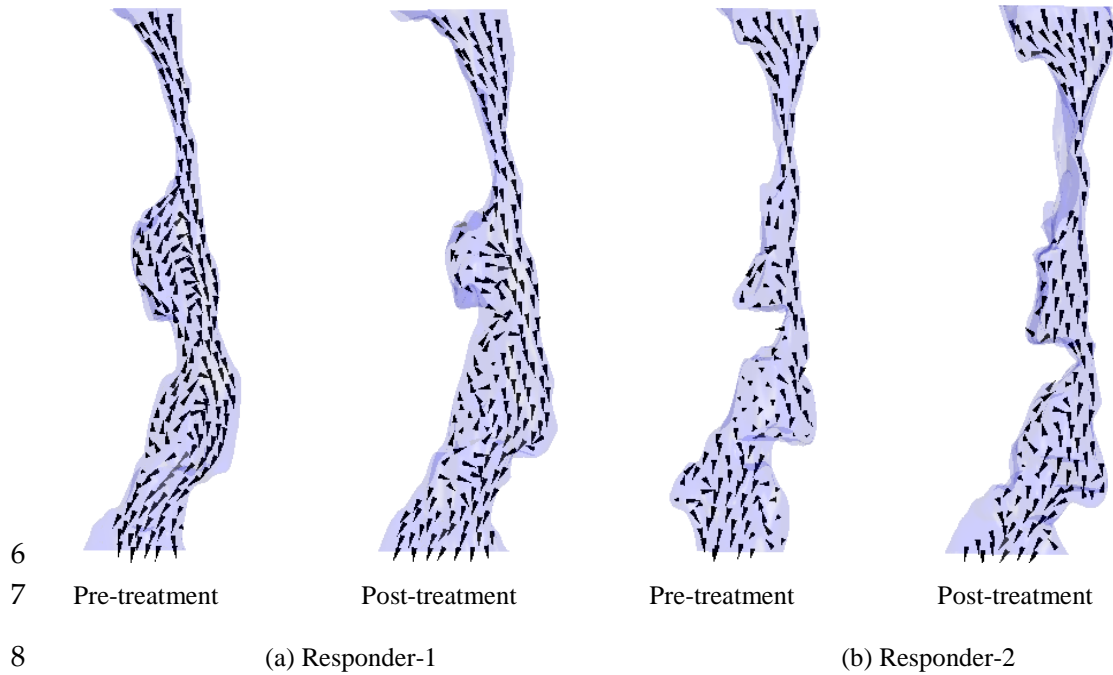
5
6
7

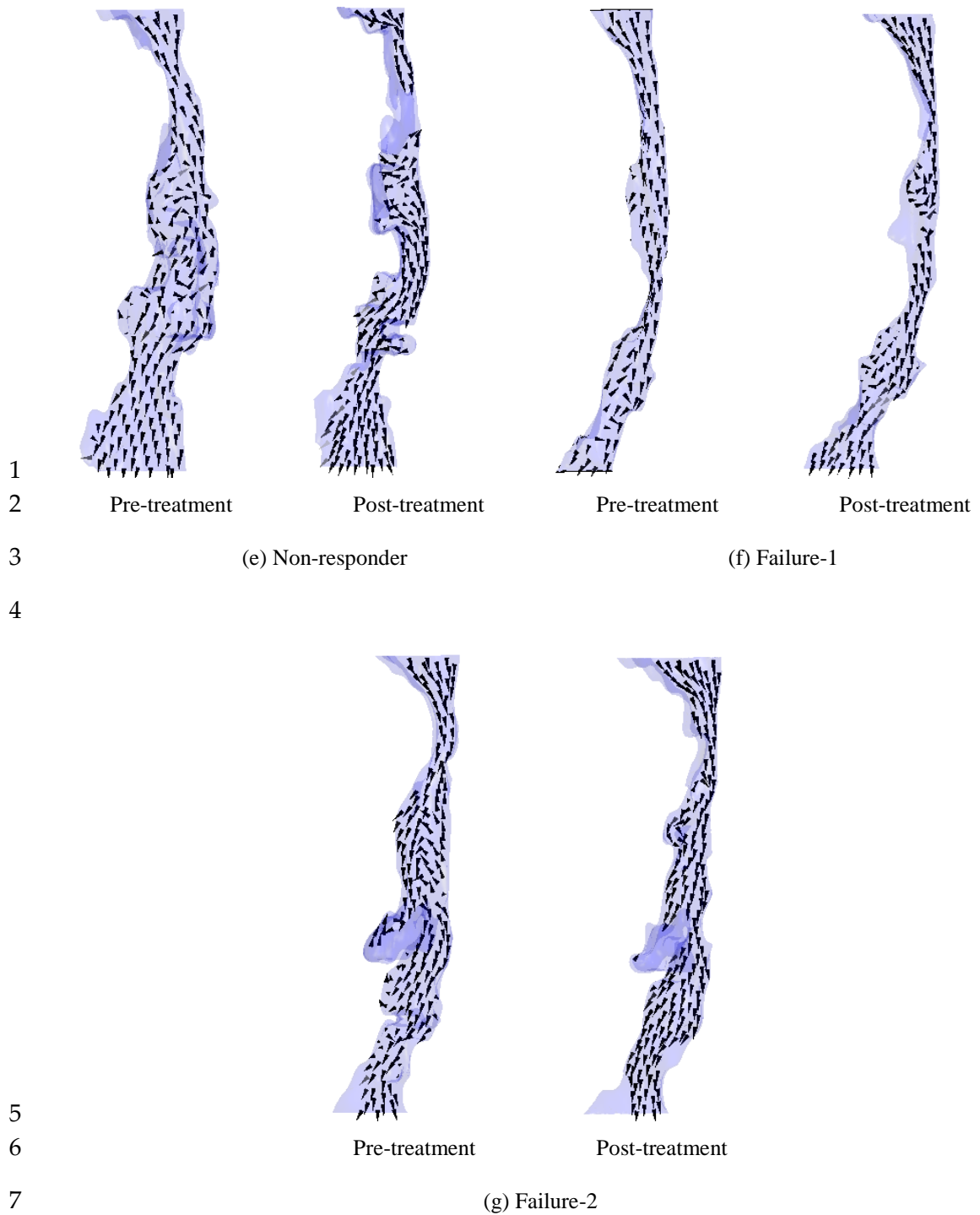


8 **Figure 51: UA Flow Streamline of All Patient Cases Pre- and Post-treatment**

9 The vector plots in Figure 52 indicate that there was a high velocity down to the lower
10 pharynx. In cases such as Responder-2 and Failure-1, the epiglottis and root of the

1 tongue induced an equivalent or even more significant flow restriction than that at the
2 soft palate. These alternating regions of high shear force on the posterior wall and the
3 recirculation could affect the movement of different parts of the UA. It was also evident
4 that the pharyngeal jet and velocity of recirculation were significantly reduced in the
5 treated case, which may be an indicator of successful treatment.



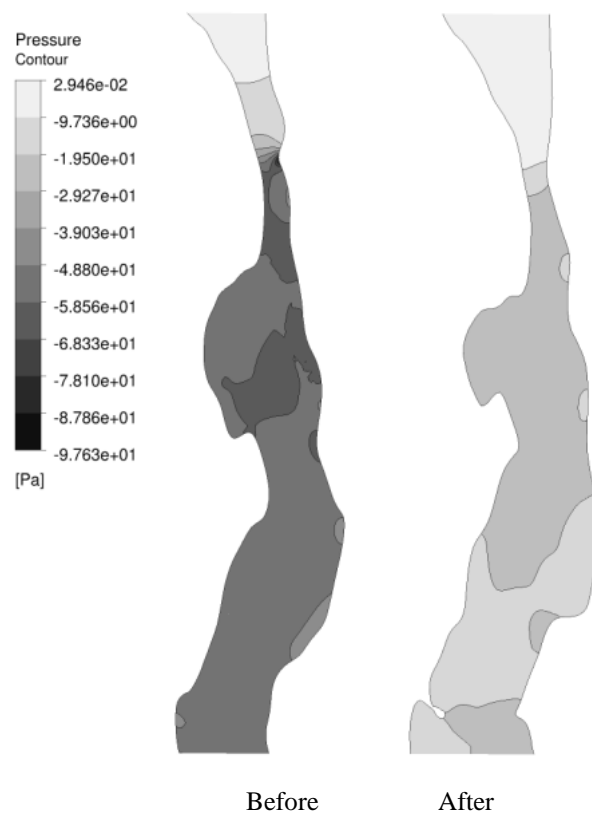


9 **Figure 52: UA Flow Vector Plot at the Vertical Mid-plane of UA**

9 **4.5 UA Pressure Profiles of Responder-1**

10 Responder-1 was a typical case who received successful treatment. The pressure
11 contours of the UA before treatment indicated that low pressure regions were located at
12 the distal velopharynx, oropharynx and hypopharynx (Figure 53). At the velopharynx,
13 the higher velocities indicated lower static pressures, as per Bernoulli's theory. A

1 significant inward pressure force (average 0.304 N on the entire UA) was generated
2 from the pressure difference between this low pharyngeal pressure and the external
3 tissue pressure on the UA wall, which could effectively collapse the UA. The pressure
4 gradient in the oropharynx was relatively large, since the flow features of the
5 pharyngeal jet and a large recirculation zone occurred in this region, high-speed jet flow
6 and strong eddies resulted in relatively low pressures. The post-treatment pressure
7 profile was similar to the pre-treatment, whereby the lowest pressure remained at the
8 velopharynx. However, the pressure fluctuation in the oropharynx became negligible
9 and the magnitude of the pressure gradient was much lower. A measure of maximum
10 pressure drop (ΔP_{Max}) was defined as the pressure difference between the inlet pressure
11 and lowest pressure in the UA model. This ΔP_{Max} reflected the level of negative pressure
12 in the UA. The environmental pressure would force the UA wall tissues to close the UA
13 lumen. A greater ΔP_{Max} could refer to a lower UA pressure and more intensive
14 collapsing pressure force would act on the UA wall. Thus, the ΔP_{Max} might quantitatively
15 indicate the OSA severity.

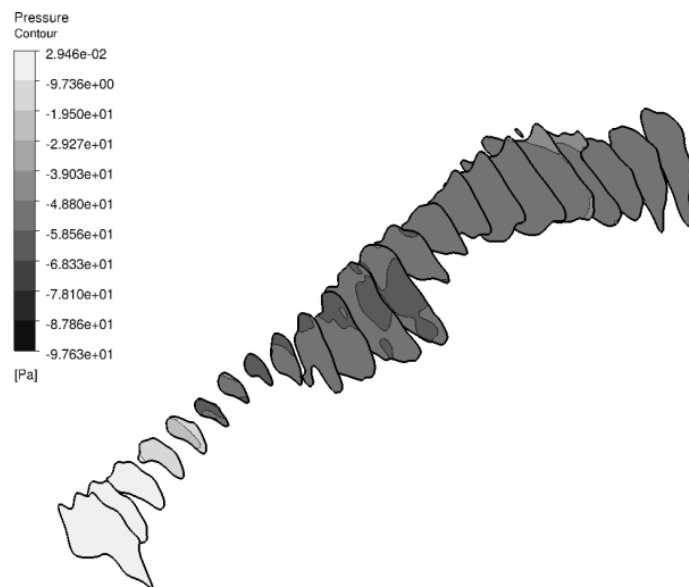


16
17

18 **Figure 53: 2D Pressure Contours on the Mid-plane of the UA Model of Responder-**
19 **1, before and after MAS Treatment**

1 4.6 UA Quantitative Pressure Profile in All Cases

2 The pressure profile of Responder-1 indicated an obviously higher UA pressure level in
3 the post-treatment model. This increase in UA pressure is a positive sign for MAS
4 treatment. The expansion in UA volume significantly reduced the pressure drop, and a
5 higher UA pressure was believed to reduce the level of UA collapse, which determines
6 the severity of OSA (AHI). It was considered useful to obtain the quantitative pressure
7 profile of all cases. Thus, the UA flow field was horizontally segmented into planes
8 every 5 mm (Figure 54). Each horizontal segment contained the minimum pressure,
9 since the lowest pressure region was always located at the airway wall (Figure 52).



10

11

Note: Airway segments were taken at 5 mm intervals along the length of the UA.

12

Figure 54: Pressure Represented by Horizontal Slices in the UA Model of

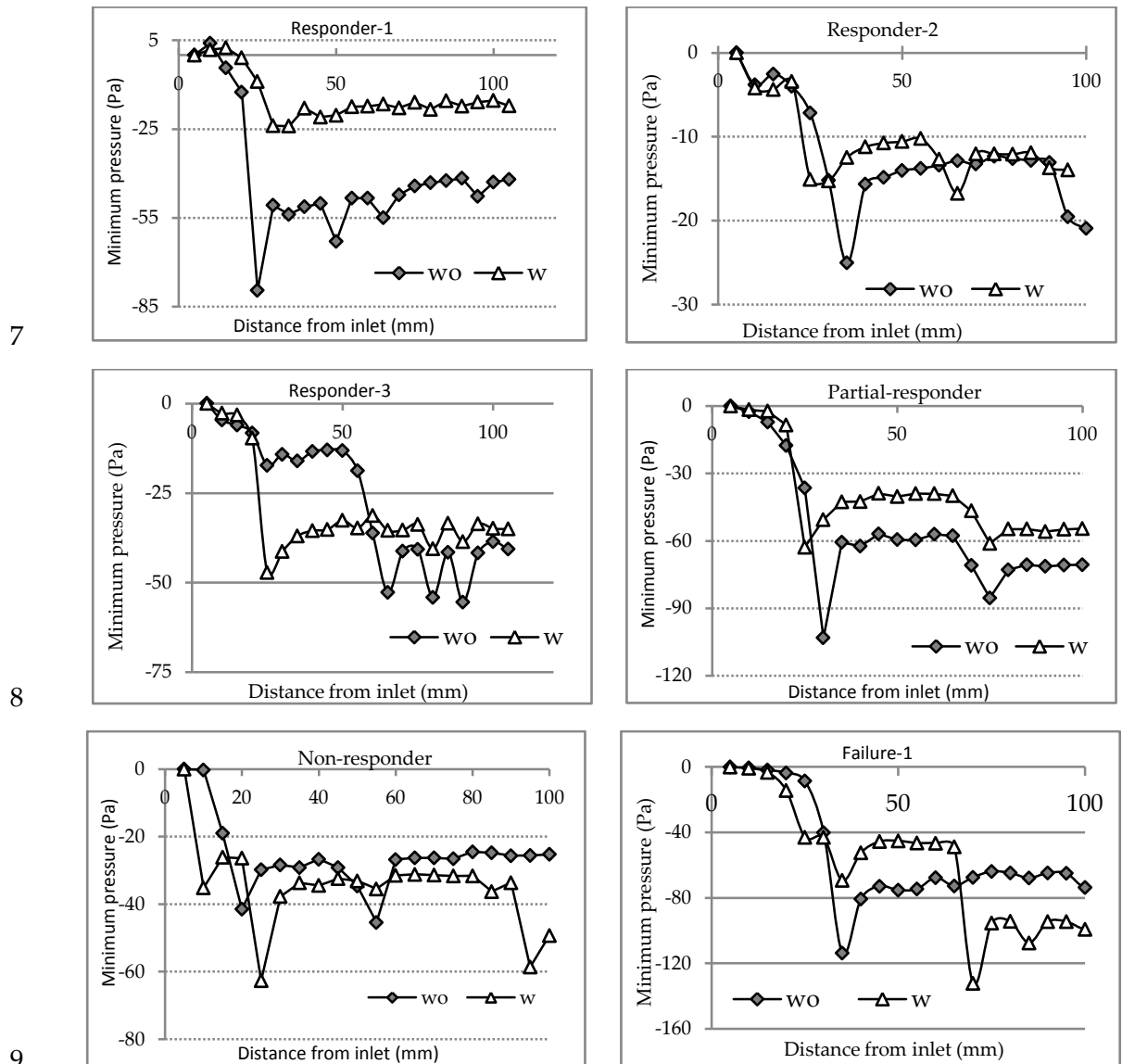
13

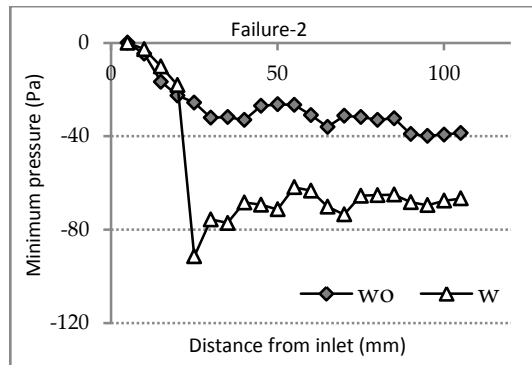
Responder-1 before MAS Treatment

14

Figure 55 plots the minimum pressure value of every 5 mm in the UA of all patient
15 cases. Responder-1 had a 50 Pa increase (-90 to -40 Pa) in the lowest pressure with the
16 MAS, while Failure-2 showed the reverse, with a 50 Pa decrease. The other patients did
17 not show dramatic changes in lowest pressure. It is worth noting that, in two airway
18 geometries (Responder-3 without MAS and Failure-1 with MAS), the pressure profiles
19 additionally showed a relatively large pressure drop behind the epiglottis at the tongue
20 base, demonstrating a different pressure pattern and another region of losses compared
21 to that with soft palate restricted flow only. In many cases, the location of the minimum

1 pressure changed after treatment. However, it was obvious that the changes in the
 2 minimum pressure of the entire UA followed the treatment response. For responder
 3 cases, the minimum pressure was increased, although some in a different location. In
 4 the failure cases, a lowered minimum pressure was found after treatment. The results
 5 indicated the possibility that there was a connection between the changes in the
 6 minimum pressure of UA and the treatment response (changes in AHI).



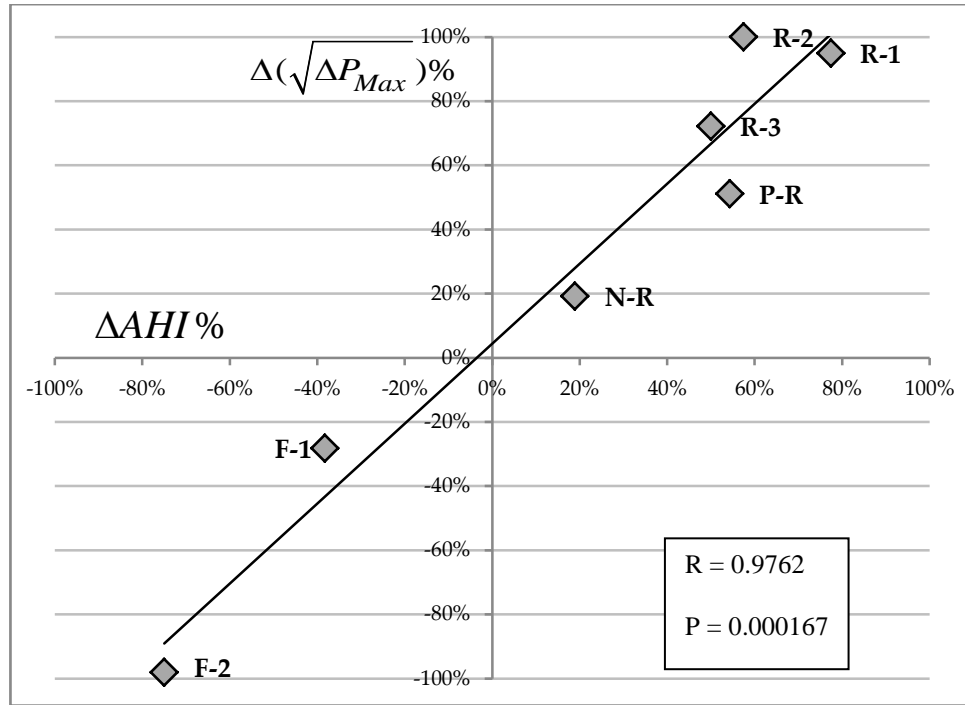


1

2 **Figure 55: Minimum Pressure (Pa) Value along Each UA Model (WO = Without**
 3 **MAS, W = with MAS)**

4 **4.7 Relationship with Treatment Outcome**

5 Section 4.3 compared the changes in UA geometry parameters with MAS to the
 6 treatment response using correlation analysis. There were no significant correlations
 7 between changes in airway geometry and AHI (all $p > 0.05$), but there was a trend
 8 towards a relationship with increased minimum cross-section area ($\Delta\text{CSA}_{\text{Area}}\%$) and AHI
 9 change ($\Delta\text{AHI}\%$) ($r = 0.69$, $p = 0.086$, Figure 49). However using CFD results, a new
 10 parameter ($\Delta\sqrt{\Delta P_{\text{Max}}}\%$) was developed from the pressure results—the percentage
 11 change in the square root of the maximum pharyngeal pressure drop with MAS. This
 12 had a strong correlation with $\Delta\text{AHI}\%$ ($r = 0.9762$, $p = 0.000167$, Figure 56). These two
 13 endpoints may be strongly related because UA pressure is coupled to the flow velocity,
 14 which is largely varied by UA geometry and movement. This correlation with treatment
 15 response suggests that the change in UA pressure profile with MAS has great potential
 16 as a predictor of treatment outcome.



1

2 Note: R = responder, P-R = partial responder, N-R = non-responder, F = failure, R = Pearson's correlation
 3 coefficient, P = two-tail probability.

4

Figure 56: Relationship between $\Delta\sqrt{\Delta P_{Max}}\%$ and $\Delta AHI\%$

5

These results are similar to those of De Backer et al. [59], although a higher correlation was observed in this study. However, there were some key areas upon which we built in this work. A vital aim of this study was practical application in the clinical setting. The

6

current study had the advantage of introducing $\Delta\sqrt{\Delta P_{Max}}\%$ and $\Delta AHI\%$, which

7

measure the effects of the MAS on UA based on the individual baseline. This minimised the individual difference in respiration flow rates and UA pressures.

8

Previous studies, as well as our flow sensitivity study, showed that, in the same UA geometry, under the assumption of rigid UA wall, the flow rate (\dot{V}) has an approximately linear correlation with the square root of the maximum pressure drop

9

($\sqrt{\Delta P_{Max}}$) [49, 51], which can be written as:

10

$$\dot{V} \propto \sqrt{\Delta P_{Max}} \tag{4-1}$$

11

when $\dot{V}=0$, $\sqrt{\Delta P_{Max}}=0$. Hence, Equation 4-2 can be expressed as:

12

$$\sqrt{\Delta P_{Max}} = C\dot{V} \tag{4-3}$$

1 assuming that C is a nonzero and positive constant.

2 \dot{V} is a typical ventilation flow rate of OSA. It is predominantly dependant to personal
3 ventilation effort. The UA geometry can be deformed when a MAS is fitted. The change
4 in UA geometry can result a different flow resistance and therefore impact on the
5 ventilation flow. However the variation in ventilation flow that associates to UA
6 collapse is insignificant. Thus, the same \dot{V} before and after MAS is used here. From
7 Equation 4-4:

$$8 \quad \sqrt{\Delta P_{\text{Max}(\text{before})}} = C_{\text{before}} \dot{V}, \quad 4-5$$

$$9 \quad \sqrt{\Delta P_{\text{Max}(\text{after})}} = C_{\text{after}} \dot{V}, \quad 4-6$$

10 where C_{before} and C_{after} are constants before and after MAS treatment, respectively.

11 Thus:

$$12 \quad \Delta(\sqrt{\Delta P_{\text{Max}}})\% = \frac{\sqrt{\Delta P_{\text{Max}(\text{before})}} - \sqrt{\Delta P_{\text{Max}(\text{after})}}}{\sqrt{\Delta P_{\text{Max}(\text{before})}}} = \frac{C_{\text{before}} \dot{V} - C_{\text{after}} \dot{V}}{C_{\text{before}} \dot{V}} = \frac{C_{\text{before}} - C_{\text{after}}}{C_{\text{before}}} \quad 4-7$$

13 Finally, this results in:

$$14 \quad \Delta(\sqrt{\Delta P_{\text{Max}}})\% = \frac{C_{\text{before}} - C_{\text{after}}}{C_{\text{before}}} \% \quad 4-8$$

15 which is independent of \dot{V} .

16 In contrast, since the UA pressure was calculated based on the velocity-pressure
17 coupling method in CFD, the catheter-measured UA pressure will be cancelled when
18 calculating the ΔP_{Max} . As a result, the patient-specific flow rate and UA pressure could
19 be approximated in our study method. De Backer and colleagues also found largely
20 geometric correlations with AHI response, although, in larger studies, UA structure and
21 AHI are usually not related [69]. It seems unlikely that geometric changes alone will be
22 adequate to enable clinical prediction of MAS treatment response.

23

1 **4.8 Summary**

2 The CFD simulation provides a method to non-invasively acquire the UA flow
3 characters of OSA patients. In order to increase the efficacy of MAS, treatment
4 prediction method is required to target suitable patients for MAS treatment. Based on
5 the CFD results in this thesis, a predicting parameter ($\Delta\sqrt{\Delta P_{\text{Max}}}$ %) was designed based
6 on the changes of UA pressure drop pre- and post-MAS treatment. The parameter
7 $\Delta\sqrt{\Delta P_{\text{Max}}}$ % is superior to other parameters in terms of having the highest correlation
8 factor of 0.9762 with the AHI data. However, a large quantity of patient cases is
9 required to further develop and examine this prediction model.

10

1 **Chapter 5: Fluid Structure Interaction Results of Collapsible** 2 **UA Models**

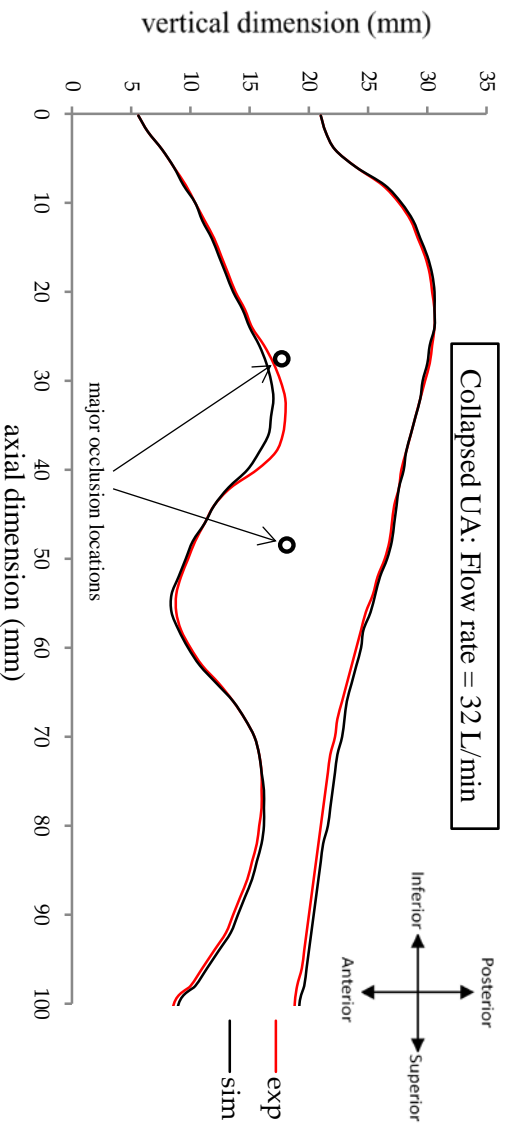
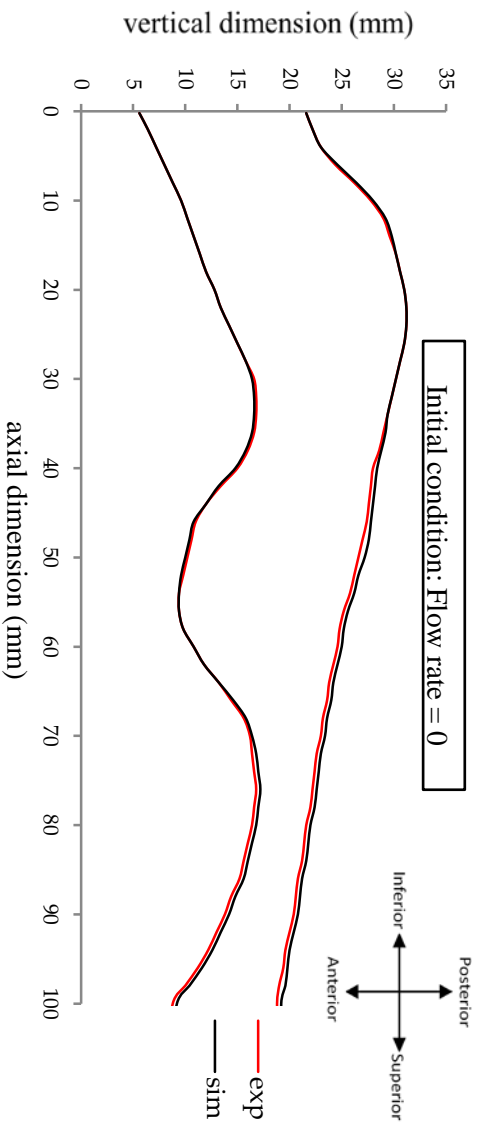
3 **5.1 Introduction**

4 The FSI results demonstrated the way that UA collapses in regard to OSA. The self-
5 contact of the UA wall was found in the pre-treatment case of a responder and post-
6 treatment case of a failure. Further, the FSI pressure profile indicated that the CFD-
7 based treatment prediction model may be sufficient, since the minimum pressure in the
8 UA remained unchanged despite the narrowing of the UA lumen because of collapse.
9 Both the CFD and FSI results were validated with experimental data. Sections 5.2 and
10 5.3 have been previously published in the paper ‘Using Computational Fluid Dynamics
11 and Fluid–Structure Interaction to Study Upper Airway Occlusion in Obstructive Sleep
12 Apnea’ [75].

13 **5.2 Validation of UA Deformations**

14 **5.2.1 Comparison of Wall Deformation in the Experimental and FSI Models**

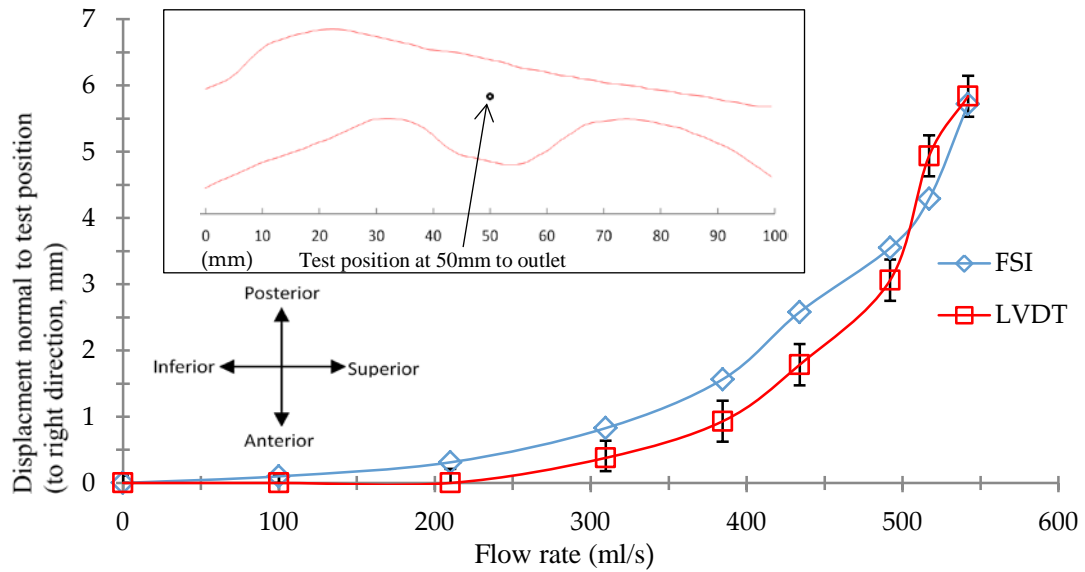
15 Section 3.11 described the experimental setup for the flexible UA wall model. Figure 57
16 shows a comparison between the experimental and FSI boundary deformation. The
17 boundary should initially be the same for zero flow. The slight mismatch between the
18 experiment and numerical results in the image (top graph) was caused by a fabrication
19 error. When the model collapsed (lower graph), there was an obvious difference
20 between the two results at the epiglottis region. The experimental results showed a more
21 obvious inward movement of the tongue base area, with a maximum difference of 1.2
22 mm compared to the simulation results. The occlusion events at the left posterior
23 oropharynx and anterior hypopharynx (indicated in Figure 57) were observed in both
24 the experiment and simulations.



Note: exp = experimental result, sim = simulation result. The top graph shows the initial condition with no airflow. The bottom graph shows the boundary displacement when the walls collapsed to the point at which the two initially touched each other. The images were recorded using a high-speed camera. The boundaries were then extracted from the images.

Figure 57: Comparison of Wall Boundary of FSI and Experimental Models

Figure 58 shows the wall displacement as a function of flow rate at a test point 50 mm from the outlet for both the experimental and FSI results. Overall, there was excellent agreement between the two results. The experiments showed slightly less horizontal movement compared to the simulations at low flow rates. A maximum discrepancy of 0.7 mm was found at 434 ml/s.



1

2 **Figure 58: Comparison of the Wall Displacement 50 mm from the Outlet between**
 3 **FSI and Experiment Results**

4 **5.2.2 The Uncertainty in Experimental Results**

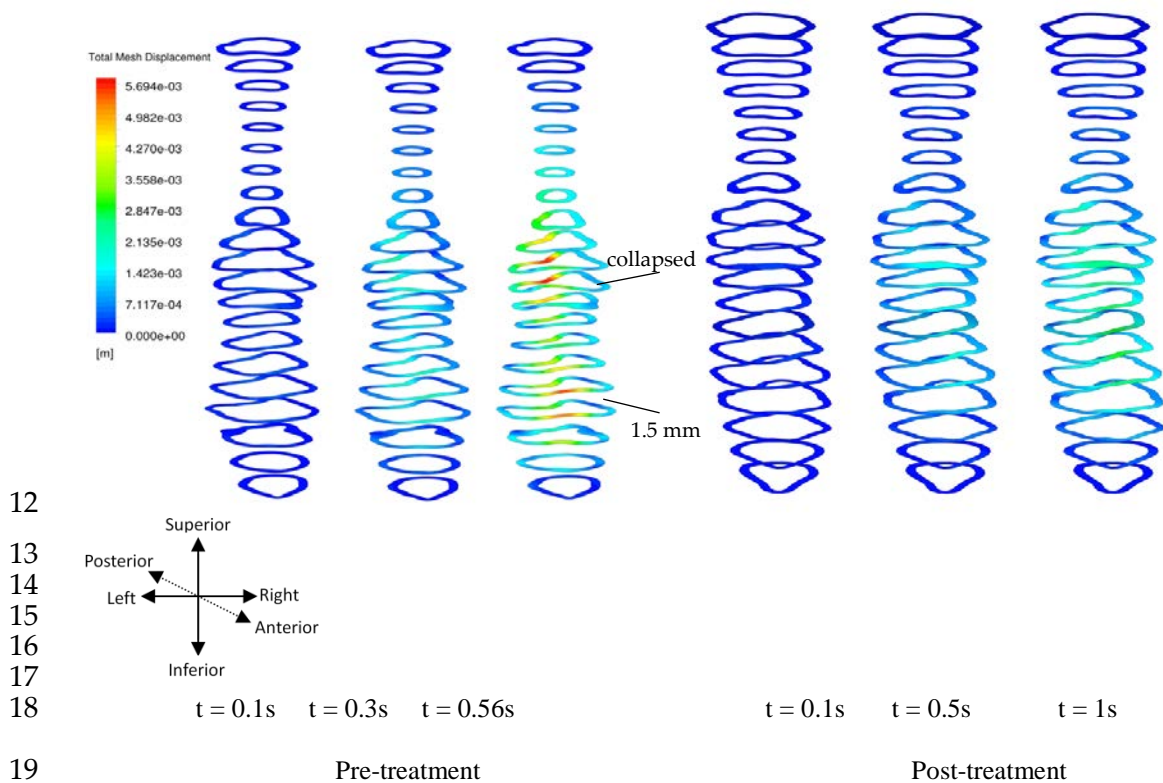
5 The Young's modulus of the SLA resin was tested with a biomaterial tensile testing
 6 system, Instron 5543 (LBEQ-300). The accuracy of the material elongation
 7 measurement was +/- 0.02 mm or 0.05% of the readings (whichever was greater). As
 8 the extension of the testing material was 12 to 15 mm, the estimated error was +/-0.02
 9 mm. This test also considered the accuracy of the testing load measurement, which was
 10 +/- 0.5% of the reading. The maximum error on the applied load was 0.067 N at the
 11 peak load of 13.5 N. The total errors on the Young's modulus and Poisson's ratio were
 12 2.52% and 1.33%, respectively.

13 The boundary of the UA wall in the experiments was captured with a high-speed camera
 14 with an image resolution of 800 x 600. The error in the plotted UA boundary line was
 15 negligible. The LVDT sensor had a measuring accuracy of 0.2 mm, while the ADC unit
 16 and oscilloscope had an accuracy of 0.4% and 0.3% of the readouts. The combined
 17 uncertainty was 0.27 mm.

1 5.3 FSI Results of Responder

2 5.3.1 Deformation of the UA Wall

3 Figure 59 indicates the deformation of the UA boundary obtained from the FSI
4 simulations. Contact between the anterior and left side retroglossal walls occurred at
5 0.56s with a flow rate of 127 ml/s for the before-MAS case. This wall contact showed
6 that a lateral wall initiated occlusion happened at the base of the tongue. The maximum
7 deformation was 5.81 mm, located at the left posterior side of the oropharynx. Another
8 potential occlusion was at the anterior wall of the pharynx, with a remaining gap of 1.5
9 mm. The wall displacement at the velopharynx was negligible. The simulation was
10 terminated when the elements were significantly distorted in the contact region and the
11 convergence targets were no longer achieved.



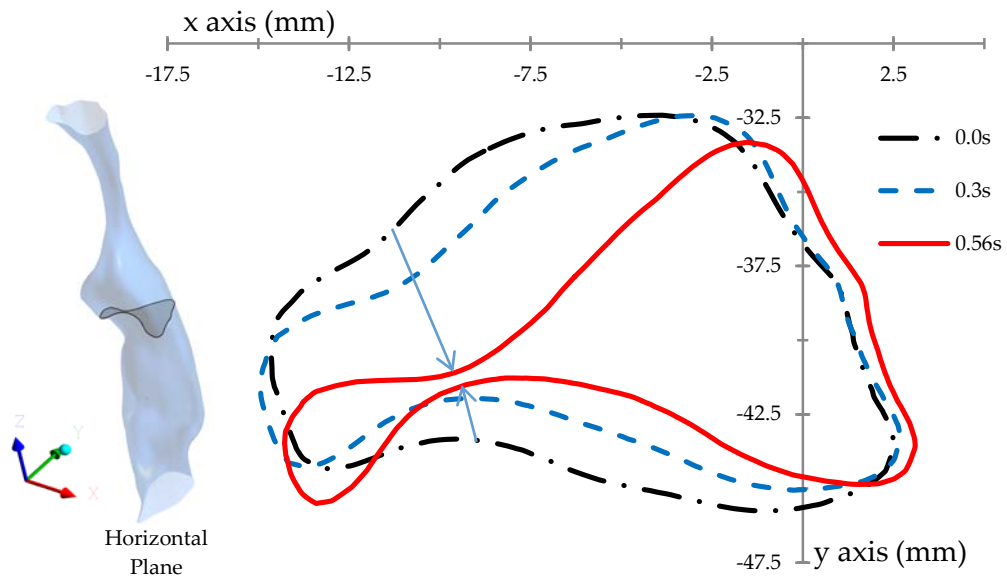
Note: The full simulation times for pre- and post-treatment model were 0.56s and 1s, respectively. Times were selected to present different stages of wall displacement.

24 **Figure 59: Geometry Displacement of the UA Wall of Responder-1 (Left) before**
25 **and (Right) after MAS Fitted, at Three Time Points During the Cycle**

In the UA geometry with the MAS in place, the UA deformation was significantly reduced. Noticeable deforming regions were found at similar locations to the pre-

1 treatment case; however, the collapse of the UA was prevented. These results
 2 corresponded with the known clinical response of this patient, who went from having
 3 severe OSA (baseline geometry) to having no OSA via MAS treatment, thereby
 4 indicating the possibility of treatment prediction. However, the question remains how
 5 influential the flow is during the airway collapse.

6 Figure 60 demonstrates that the major UA wall deformation occurred at an area on the
 7 left side of the oropharynx, 50 mm from the inlet. The anterior and posterior UA walls
 8 collapsed towards each other. At 0.3s, the anterior wall collapsed 1.7 mm, while the
 9 posterior wall collapsed 1.8 mm. The posterior and anterior wall touched at 0.56s. The
 10 maximum deformations on the anterior and posterior wall were approximately 2.1 mm
 11 and 5.2 mm finally. It was found that the collapse of the posterior wall sped up after
 12 0.3s. This might have resulted from a dramatic change of pressure distribution in this
 13 area, which means that a significantly low pressure was generated at the posterior wall
 14 after 0.3s. The UA pressure result will be discussed in the following sections.



15
 16 The cross-section plane was located 50 mm from the inlet. The x and y axes represent the coordinates of
 17 the entire 3D UA model.

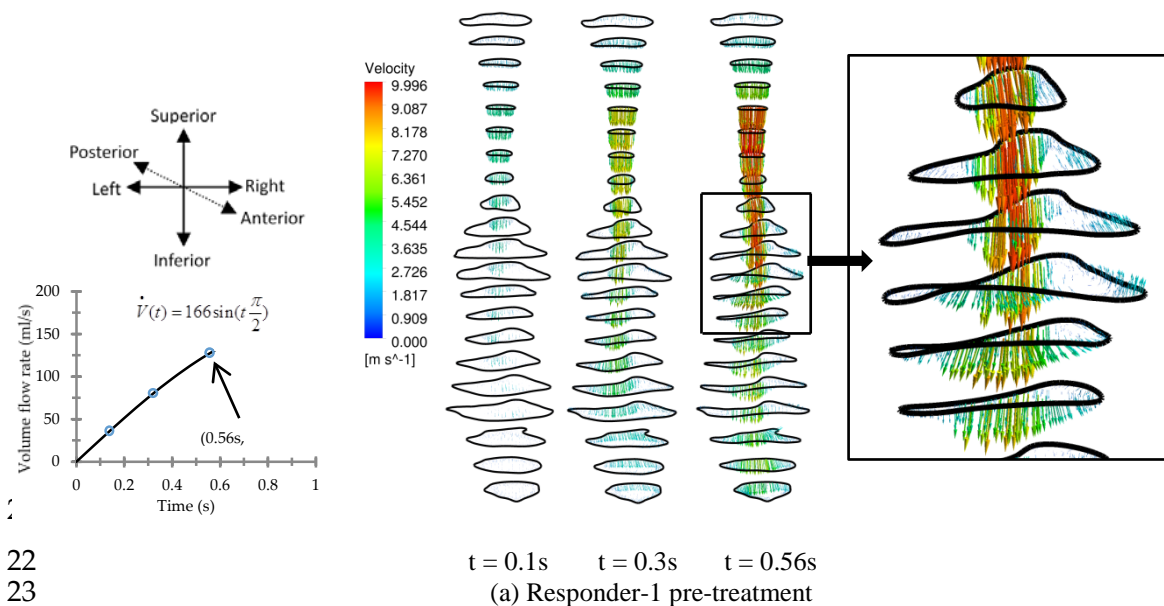
18 **Figure 60: UA Wall Deformation of Responder-1 before Treatment at 0.0s, 0.3s**
 19 **and 0.56s**

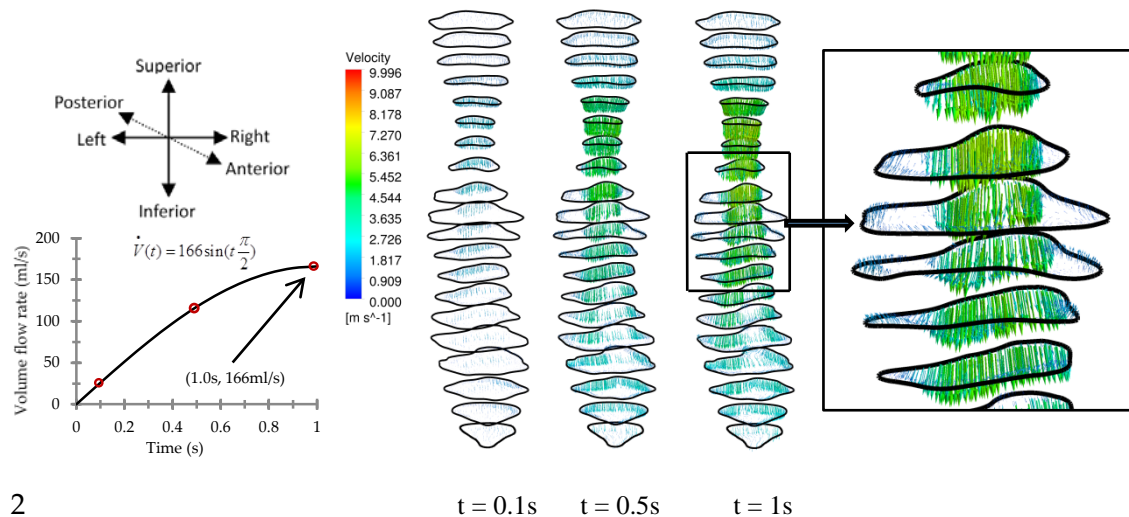
20 **5.3.2 Velocity Profile**

21 Figure 61 presents the cross-sectional vector profiles of the UA flow. The pre-treatment
 22 case indicated a fast-developing pharyngeal flow, which was reported as ‘pharyngeal jet’

1 in previous studies [22, 49, 75], formed at the velopharynx. The jet flow closely
 2 attached to the posterior UA wall with a maximum velocity of 10.0 m/s. At 0.1s and
 3 0.3s, the developing jet flow travelled vertically from the velopharynx to the
 4 hypopharynx. A symmetrical flow pattern was found in the oropharynx. When the
 5 occlusion occurred, the path of the jet flow was slightly offset to the right. This induced
 6 an asymmetric flow structure with high turbulence. The flow was restricted at the left
 7 side due to the retroglossal occlusion. The continuous narrowing of the UA pathway
 8 increased the local jet velocity, which further helped the collapsing process. A strong
 9 flow recirculation was generated in the right oropharynx lumen, which dissipated the jet
 10 flow kinetic energy by decreasing the flow velocity and producing significant
 11 turbulence.

12 For the post-treatment (with MAS) model, more uniform flow profiles with lower figure
 13 velocity were found at the velopharynx. The slightly deforming UA wall had no
 14 obvious effect on the flow structure. The maximum velocity of 6.74 m/s was located at
 15 the velopharynx. This uniform and low velocity flow formed a weak ‘pharyngeal jet’.
 16 However, without a flow restriction in the oropharynx, the jet flow energy was largely
 17 preserved as it passed the oropharynx, thereby creating a relatively insignificant
 18 displacement. The higher jet velocity and turbulence in the pre-treatment case caused
 19 higher pressure drops (lower pressure), which led to higher collapsing forces on the
 20 airway wall.





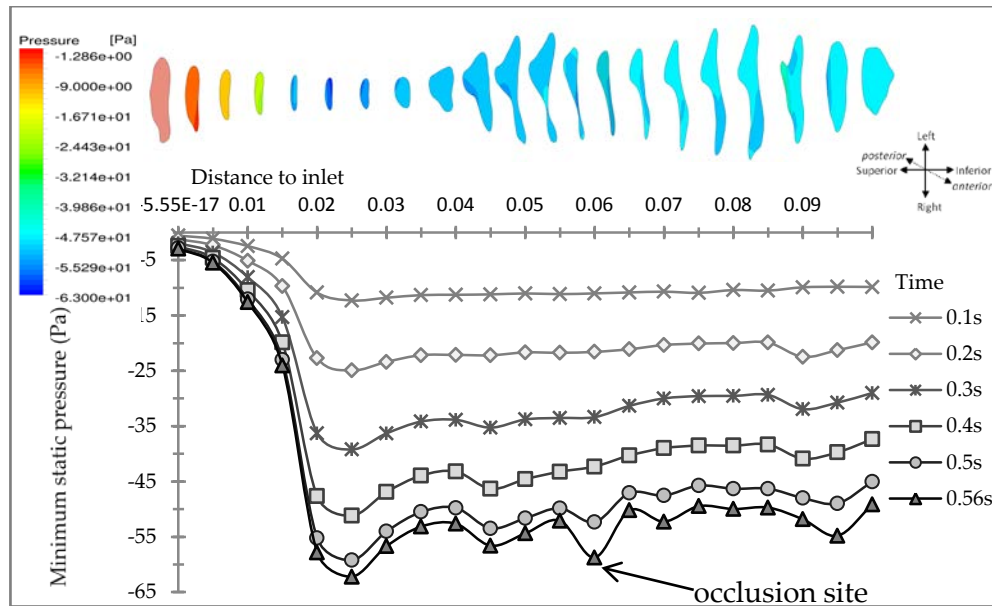
(b) Responder-1 post-treatment

Note: Times were selected to present different stages of UA flow development.

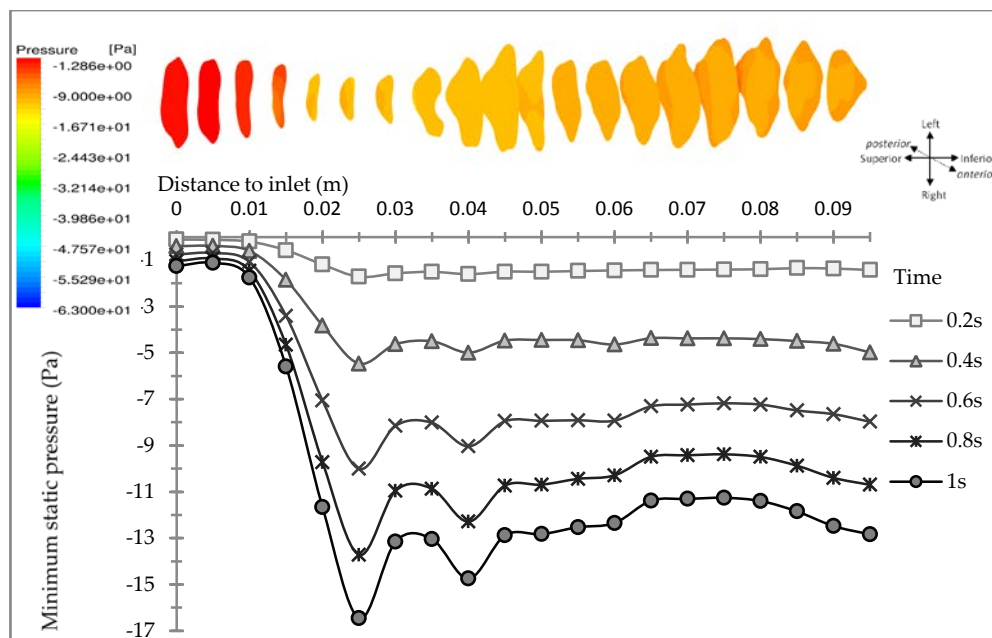
Figure 61: Velocity Vectors at the Longitudinal Cross-sections of UA of Responder-1 (a) before and (b) after MAS Fitted

5.3.3 Pressure Distribution

9 Figure 62 demonstrates the development of UA pressure distribution during the
 10 inspiratory period. A significant pressure decrease was found at the velopharynx in both
 11 the pre- and post-treatment conditions. A relatively high-pressure drop (maximum 62.2
 12 Pa) occurred in the pre-treatment case, indicating an increased possibility of UA
 13 occlusion (see Section 4.6). This low retroglottal pressure (-62.2 Pa) did not directly
 14 cause UA collapse as the velopharyngeal displacement was negligible. However, it
 15 decreased the overall oropharyngeal and laryngeal pressures, and induced wall
 16 occlusion in these regions. In the post-treatment case, this pressure drop was reduced to
 17 a very low level (maximum 16.4 Pa).



1



2

3

Note: The minimum pressure was captured from transverse planes every 5 mm from inlet.

4

Figure 62: Time Variation of Pressure Distribution along UA with (Top) Pre-treatment and (Bottom) Post-treatment Conditions

5

6 The overall pressure distribution was similar in both cases, except for an abnormal
 7 pressure decrease at the transverse plane 60 mm to inlet of the non-treatment case, at the
 8 0.5s and 0.56s of the experimental time. It was formed by flow acceleration induced by
 9 the oropharyngeal collapse. The location of the pressure abnormality appeared to reflect
 10 the site of UA collapse. At 0.4s, the pressure in the oropharynx fell to a level that had an
 11 average value of -43.8 Pa (minimum -51.2 Pa and maximum -39.1 Pa). The posterior

1 region of the oropharynx generally had a lower pressure than the anterior region, since
2 the pharyngeal jet flow was attached at the posterior oropharynx wall. This low pressure
3 in the oropharynx triggered the collapse of the left side wall. At that moment, the
4 inward pressure force overcame the ring stiffness of the surrounding UA wall, which
5 induced a rapid retroglossal occlusion. This oropharyngeal pressure level was
6 considered the ‘collapsing pressure’ of this UA.

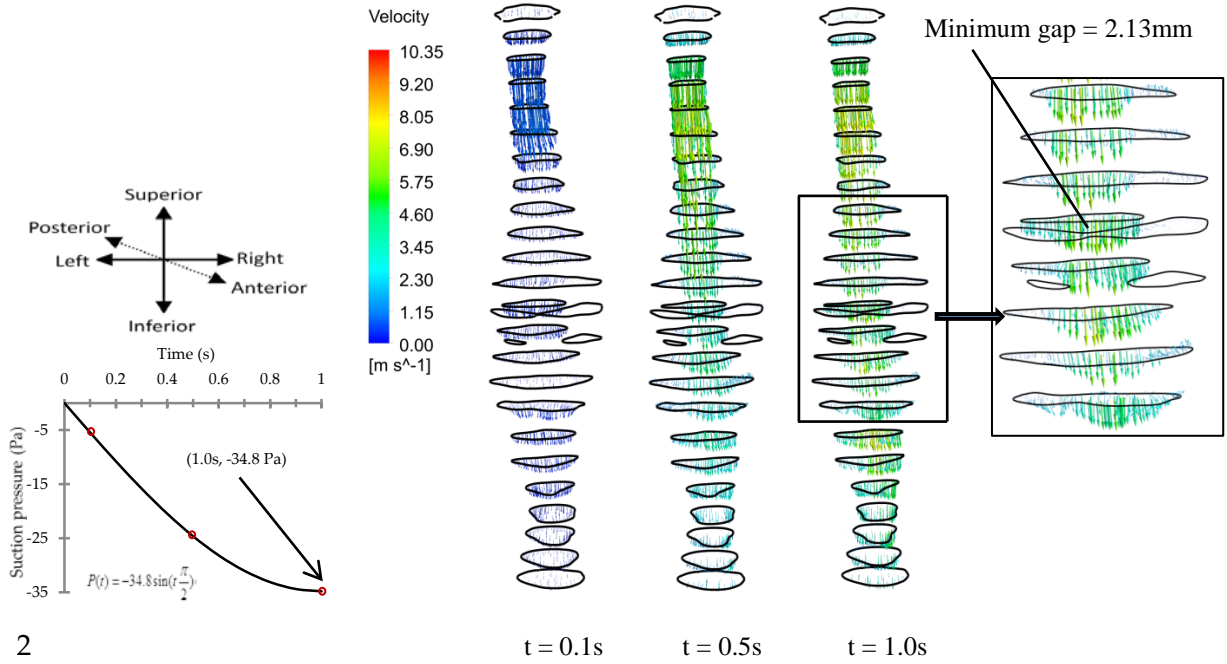
7

8 **5.4 FSI Result of a Failure Case**

9 **5.4.1 Wall Deformation and Velocity Vector**

10 The velocity vector profile of the failure pre-treatment case (Figure 61) showed an
11 increasing UA flow in a narrowing UA structure. The previous time-dependent flow
12 rate boundary condition of the responder case might not fully represent the nature of
13 breathing, as the UA flow should be generated by a negative pressure in lung. In this case,
14 a pressure-driven boundary condition was introduced for both pre- and post-treatment
15 cases. Negative suction pressures were defined at the discharge of the UA lumen. The
16 pressure value followed a sinusoidal curve and ended up at -34.8 Pa for the pre-
17 treatment case and -66.5 for the post-treatment case at 1s. The final pressure values at 1s
18 were selected according to the outlet pressure of previous CFD results, which just
19 enabled generation of a 166 ml/s flow rate for both CFD cases.

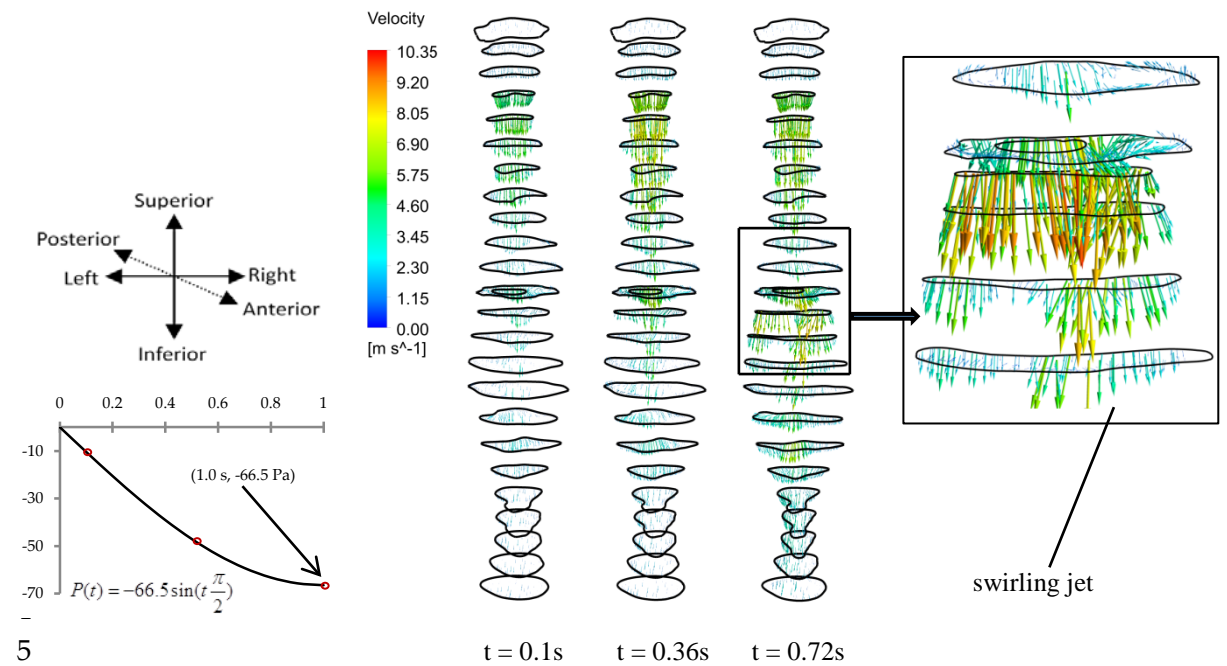
20 For the result of the pre-treatment case, the maximum deformation of 2.54 mm was
21 found at the front of oropharynx, while the minimum gap of UA of 2.13 mm was
22 located at the back of the epiglottis at the time of 1s. It can be estimated that this UA
23 model was approaching collapse and would finally collapse at higher flow rates. The
24 UA velocity appeared to be equally high at the velopharynx and hypopharynx. The
25 maximum flow velocity of 6.78 m/s was generated at the hypopharynx, which was
26 slightly higher than the flow region at the velopharynx (6.56 m/s).



2

3

(a) Failure-2 pre-treatment



5

6

(b) Failure-2 post-treatment

7

Note: Times were selected to present different stages of UA flow development.

8

Figure 63: Velocity Vectors at the Longitudinal Cross-sections of UA of Failure-2

9

(a) before and (b) after MAS Fitted

10

The wall boundary line of the failure post-treatment case depicts a collapsed UA wall.

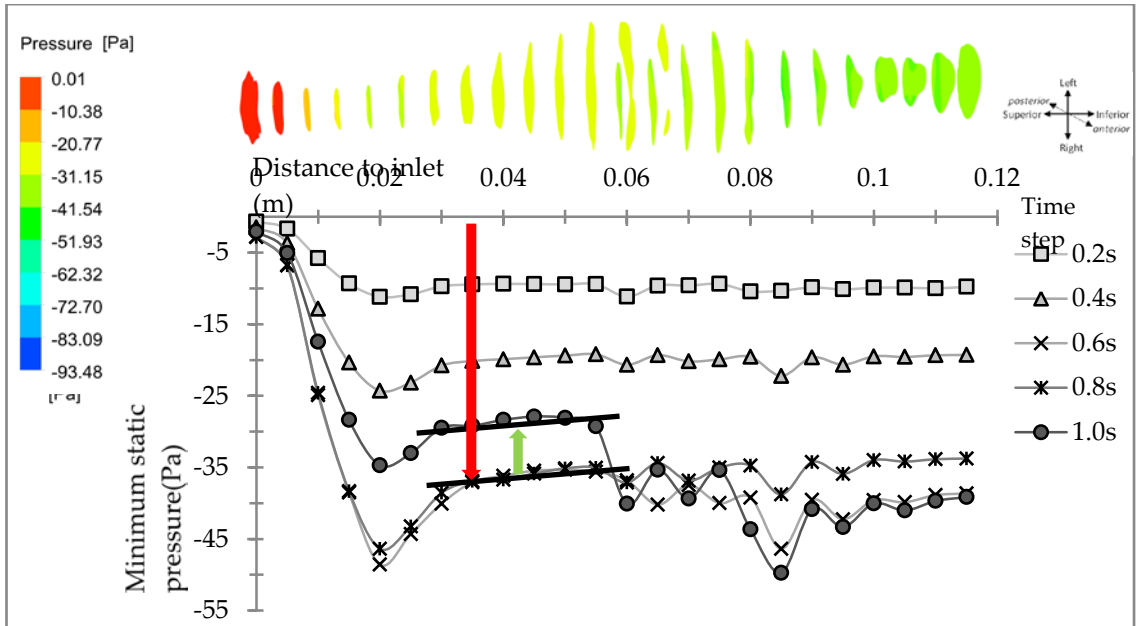
11

The self-contact of the UA wall was found at the back of the epiglottis. The wall

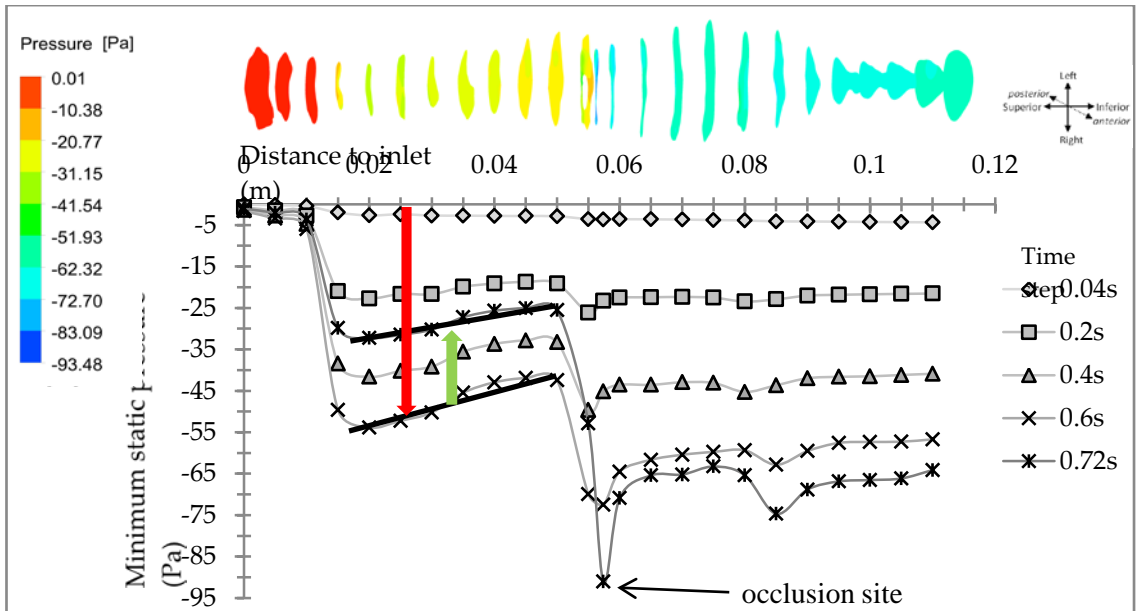
1 collapse and maximum deformation at the anterior hypopharynx (4.1 mm) largely
2 reduced the cross-section area, which significantly increased the regional velocity. The
3 flow was disturbed by the wall narrowing, which resulted in a fast swirling jet flow at
4 the hypopharynx. The maximum jet speed was 10.65 m/s. However, an enlarged
5 velopharynx was found from 0.6s to 0.72s. The average enlargement of the velopharynx
6 cross-sectional area was 3.2%, which slightly reduced the maximum velopharyngeal
7 flow velocity from 8.37 m/s at 0.6s to 6.75 m/s at 0.72s. This abnormal wall movement
8 was associated with the UA wall oscillation and will be further investigated in Section
9 5.4.3.

10 **5.4.2 Pressure Distribution**

11 Figure 64 shows the pressure distributions along the airway for different times of the
12 breathing cycle. For the pre-treatment case (AHI = 16), a maximum pressure drop of
13 49.7 Pa was found in the hypopharynx 83.5 mm to inlet boundary at the simulation time
14 1.0s. A similar 48.6 Pa velopharyngeal pressure drop occurred at 0.6s. It was observed
15 in the simulations that the velopharyngeal and hypopharyngeal wall were vibrating
16 under UA wall oscillation, which resulted in the fluctuation of the velopharyngeal and
17 hypopharyngeal volume. Similar UA wall oscillation was found in the post-treatment
18 case (AHI = 31.7). The velopharyngeal pressure rose significantly after 0.6s due to the
19 volume expansion. However, the wall oscillation had a small effect on the collapse
20 region, where a maximum pressure drop of -93.4 Pa was generated. This large pressure
21 drop finally closed the UA and led to higher deformation than for the pre-treatment case.
22 In both pre- and post- treatment cases, the UA pressure fluctuated during the time of the
23 simulation. As shown in Figure 64, the pressure fluctuation occurred in the velopharynx.
24 An increasing reduction (average -35.9 Pa) of velopharyngeal pressure was observed
25 from 0.0s to 0.6s. This pressure decreasing process ceased at 0.8s, while an approximate
26 9.1 Pa increase in velopharyngeal occurred at 1.0s. In the hypopharynx, the pressure
27 decrease was less after 0.6s, and the pressures at 0.8s and 1.0s were very close.



1
2



3

4

5

6

Note: The minimum pressure was captured from transverse planes every 5 mm from inlet. The red arrow states the maximum pressure drop at the velopharynx, and the green arrow states the velopharyngeal pressure rise because of pressure fluctuation.

7

8

Figure 64: Time Variation of Pressure Distribution along UA with (Top) Pre-treatment and (Bottom) Post-treatment Conditions

9

10

11

12

13

In the post-treatment case, pressure fluctuation only occurred at the velopharynx. The pressure level at the occlusion site continuously decreased during the simulation time, which resulted in a large pressure drop of 65.5 Pa at the lower oropharynx. The enormous fluctuation of UA pressure was induced by frequent increase and decrease in UA volume. This repetitive change in UA air space indicated that UA wall oscillation

1 could happen. In addition, in the occlusion site of the wall, the increasing negative
2 pressure force dominated the structure field. The UA wall was forced to collapse, rather
3 than vibrate.

4 **5.4.3 UA Wall Oscillation**

5 Self-excited wall oscillation occurred in the FSI simulations for both the pre- and post-
6 treatment models of the failure case. This type of oscillation has been shown to occur on
7 elastic tubes for flow with a Reynold's number greater than 200 [84]. The oscillations
8 rapidly extract energy from the flow through the surrounding wall to compensate for the
9 energy that dissipates in vibration [85]. The oscillation that occurs in the UA structure
10 may lead to snoring. The eigenfrequency of oscillation is determined by the oscillation
11 time scale [86]:

$$12 \quad T = \frac{D}{2} \sqrt{\frac{\rho_f}{K}} \quad 5-1$$

13 where D is the average hydraulic diameter of UA, ρ_f is the fluid density and K is the
14 bending stress of the UA wall [86]:

$$15 \quad K = EI \quad 5-2$$

16 Here, E is the material Young's modulus and I is the area moment inertia, which can
17 be estimated as:

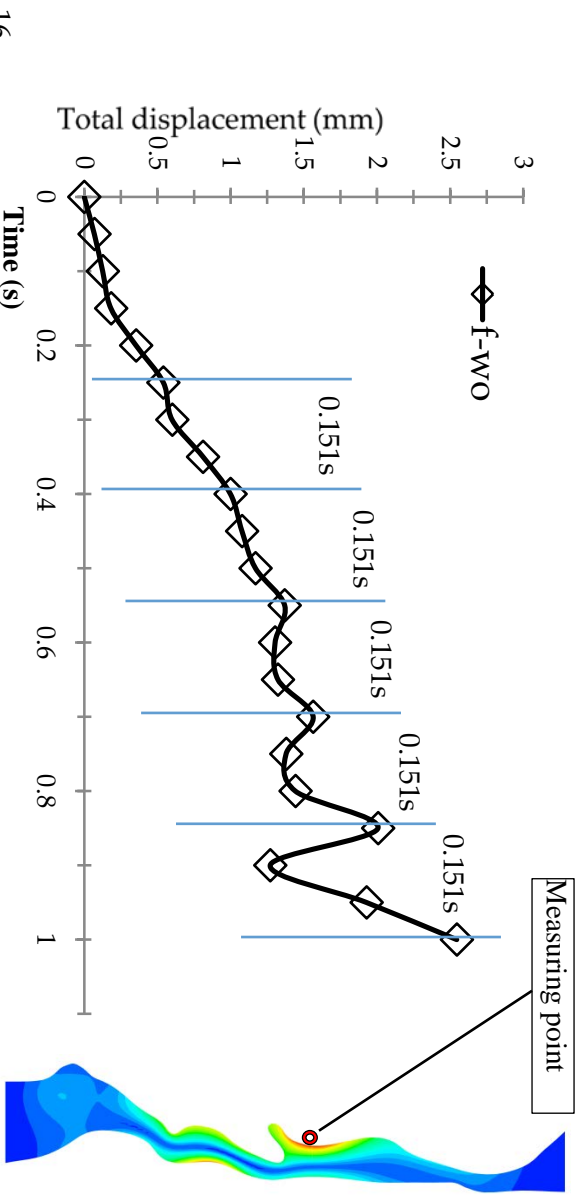
$$18 \quad I = \frac{\pi}{4} (r_e^4 - r_i^4) \quad 5-3$$

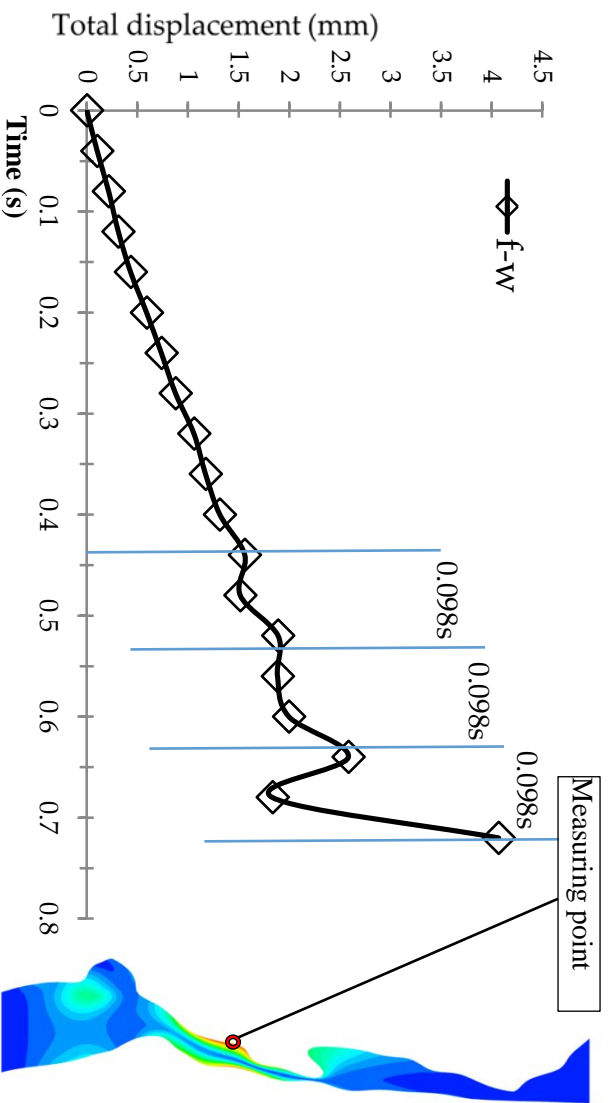
19 where r_e is the external hydraulic diameter of UA and r_i is the inner hydraulic diameter
20 of UA.

21 Using Equation 5-1, the resultant oscillation eigenfrequencies were 0.612 Hz and 0.598
22 Hz for failure in the pre- and post-treatment FSI model. The oscillation of the structure
23 should ideally occur at the n^{th} order of the fundamental frequency. However, due to the
24 interaction between the structure and flow, the actual oscillation frequency will be close,
25 yet not equal, to the n^{th} order of the fundamental frequency.

1 Figure 65 plots the UA wall oscillation of pre- (f-w0) and post- (f-w) treatment of a
2 failure case. The measuring point was selected on each model at the location with the
3 maximum displacement. The estimated periods of oscillation of the pre- and post-
4 treatment model from the simulation were 0.151s and 0.098s, respectively, which gave
5 frequencies of 6.6 Hz and 10.2 Hz. In low frequency oscillations such as this situation,
6 the wall deformation was dominated by transverse bending deflections. The frequencies
7 were low because the oscillations were governed by a balance between wall inertia and
8 the wall's relatively small bending stiffness [86].

9 The eigentfrequency determined by Equations 5-1 to 5-3 is a rough estimation of the
10 resonance frequency of UA wall structures. The equations were originally designed for
11 a uniform diameter collapsible tube [86]. The oscillating frequency of the UA wall
12 would be further influenced by the high complexity of the UA wall geometry and the
13 resultant flow recirculation and turbulence. The accurate fundamental frequency of the
14 UA structure could be predicted with the harmony analysis in the FE analysis program,
15 which may be achieved in future research.





Note: The measuring point was selected at the location with maximum displacement. The estimated period of oscillation is denoted in the figure.

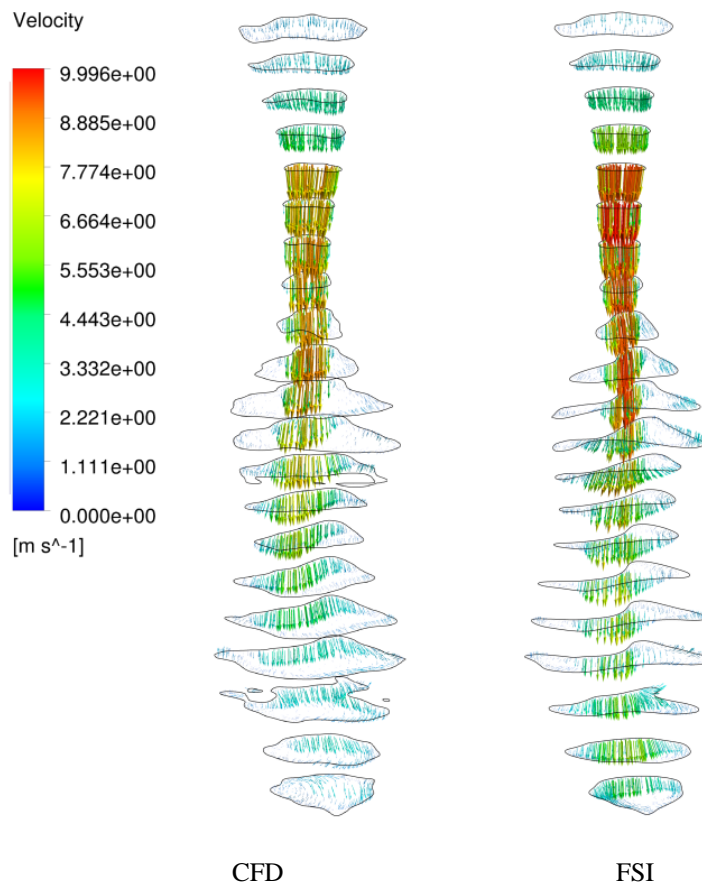
Figure 65: UA Wall Oscillation of Pre- (f-w₀) and Post- (f-w) Treatment Failure Case

5.5 Comparison of CFD with FSI

This section explores the advantages of using FSI over CFD in order to determine whether the significant extra computational time associated with FSI is justified in terms of useful output information.

FSI has an advantage over CFD because the wall is not artificially considered rigid, and the dynamics between the UA flow and soft tissue are considered. In this study, to analyse the flow profile in three dimensions across the UA, transverse cross-sectional planes were created every 5 mm from the inlet to the discharge boundary. The FSI simulation of the pre-treatment case ceased at 0.56s when collapse occurred on the oropharynx wall. The equivalent time in the cycle was used in the CFD. All figures below present the pre-treatment result at the moment that flow rate reached 128 ml/s, which was at 0.56s. The post-treatment result was plotted at a flow rate of 166 ml/s, which occurred at 1s. The collapse of the UA was demonstrated in the FSI simulations when the UA wall between the anterior and posterior side touched at the left side of the oropharynx. The larynx showed a significant deflection. Very small deflections of the UA geometry were found in the post-treatment case.

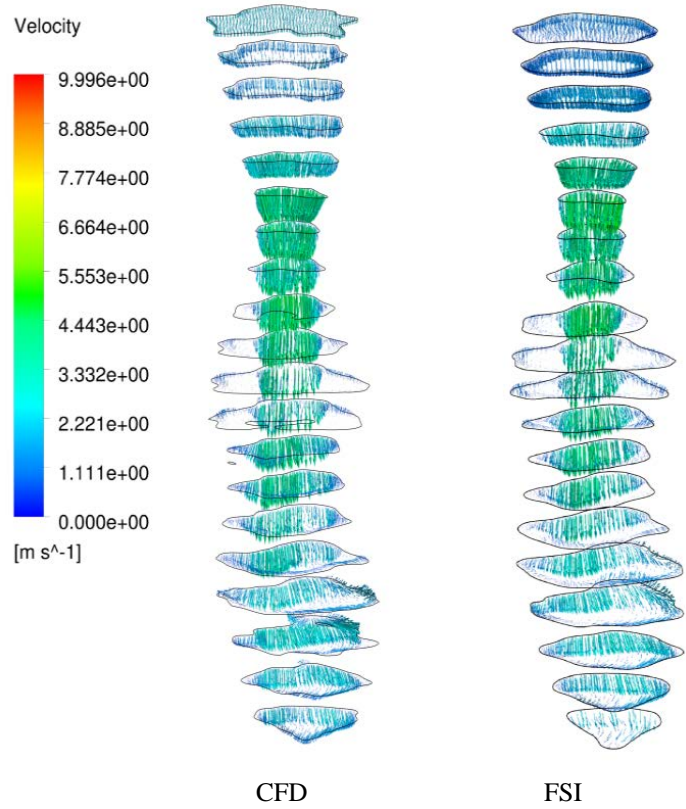
1 Figures 66 and 67 show the velocity vectors on each plane obtained from the CFD and
 2 FSI simulations for the pre-treatment case of Responder-1. The FSI model had a slightly
 3 higher maximum flow velocity (9.99 m/s) at the velopharynx than did the CFD model
 4 (9.69 m/s). However, the compliant UA boundary in the FSI model resulted in a
 5 significantly higher average flow velocity in the oropharynx and larynx, by 12.9% and
 6 13.8%, respectively. The two models had a maximum difference in velocity (1.596 m/s)
 7 at the cross-section 60 mm from the inlet, where UA collapse occurred. In the post-
 8 treatment cases, both the flow velocity and flow vector pattern were similar, as the wall
 9 motion was very small here. A maximum velocity difference of 0.22 m/s was found at
 10 the lower oropharynx.



11
 12

13 Note: Left is the CFD model and right is the FSI model. Patient case: Responder-1. The figure is plotted
 14 at a maximum flow rate of 166 ml/s.

15 **Figure 66: Velocity Vector Profile of Pre-treatment (without MAS)**

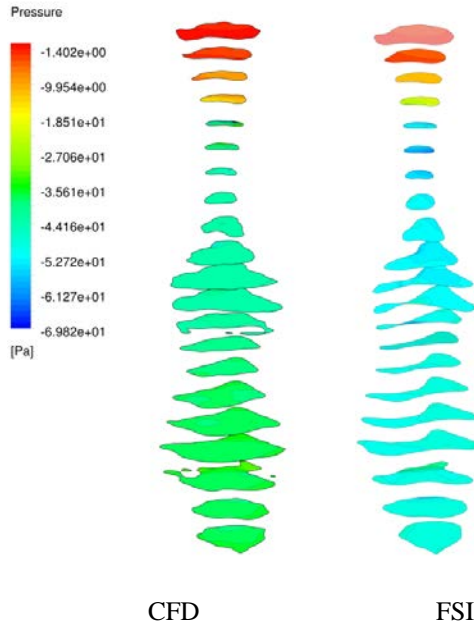


1
2

3 Note: Left is the CFD model and right is the FSI model. Patient case: Responder-1. The figure is plotted
4 at a maximum flow rate of 166 ml/s.

5 **Figure 67: Velocity Vector Profile of Post-treatment (with MAS)**

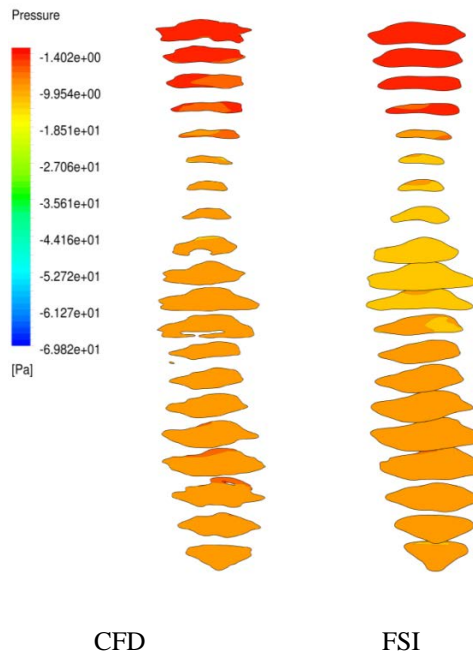
6 Figures 68 and 69 show the pressure contours in each UA cross-section for the different
7 cases. The FSI model of the pre-treatment case showed lower pressure from the lower
8 velopharynx to the larynx. The pressure difference was small for the post-treatment
9 models, with a slightly higher oropharyngeal pressure predicted by the FSI model.



1
2
3
4

Note: Left is the CFD model and right is the FSI model. Patient case: Responder-1.

Figure 68: Pressure Contours of Pre-treatment (without MAS)



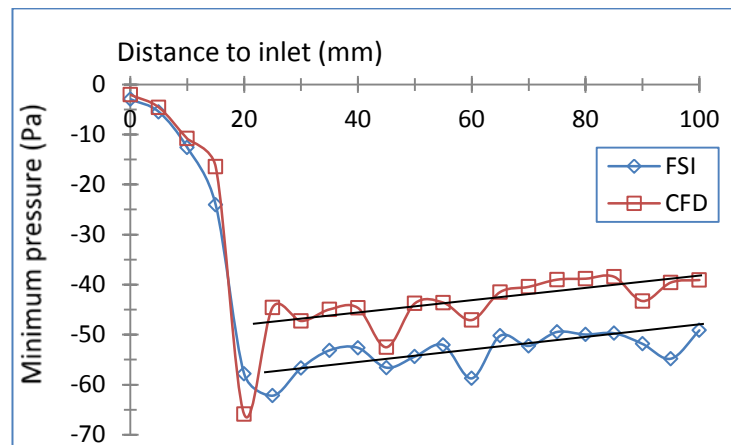
5
6
7
8

Note: Left is the CFD model and right is the FSI model. Patient case: Responder-1.

Figure 69: Pressure Contours of Post-treatment (with MAS)

9 Section 5.3 indicated that the maximum pressure drop closely correlated with the
10 treatment response (changes in AHI). The maximum pressure drop was determined
11 from the variation of minimum pressures across the UA. Figure 70 shows the minimum

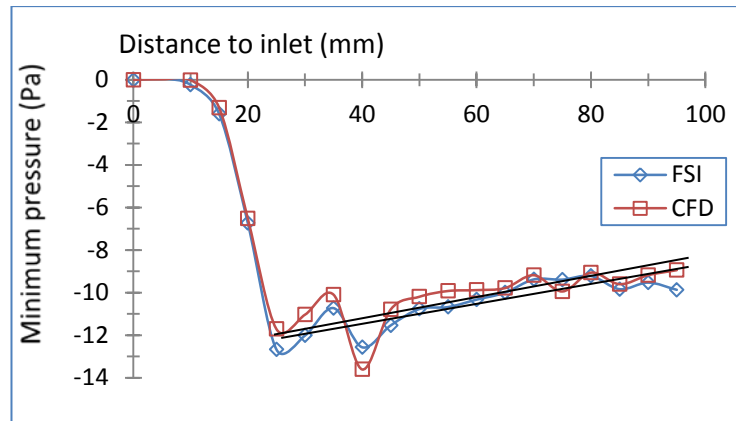
1 pressure values that were calculated from the cross-section planes in all studied FSI
 2 cases with the CFD cases. The maximum pressure drop in the CFD result was 65.5 Pa,
 3 and located in the velopharynx. A similar 63.2 Pa maximum pressure drop was found in
 4 the FSI result, also located in the velopharynx. This evidences that the UA
 5 velopharyngeal wall movement was fairly small for Responder-1. For the pre-treatment
 6 FSI model, the lower volume expansion in the deformed oropharynx and larynx resulted
 7 in a lower pressure (average 9.3 Pa less than CFD) in these areas. These low UA
 8 pressures would further react on the UA structure by speeding up collapse. The self-
 9 contact of UA wall (60 mm from inlet) resulted in a relatively low regional pressure;
 10 however, it was only 11.66 Pa less than that found using CFD. Although the wall
 11 collapse resulted in a narrow gap or even a partially closed airway, the reduction of UA
 12 volume was effective in reducing the pressure. This volume reduction was more likely
 13 to occur at the larger UA section. There were negligible changes in the geometry and
 14 velocity features between the CFD and FSI post-treatment models (no airway collapse);
 15 thus, their pressure profiles were reasonably close.



16

17

(a) Pre-treatment case



(b) Post-treatment case

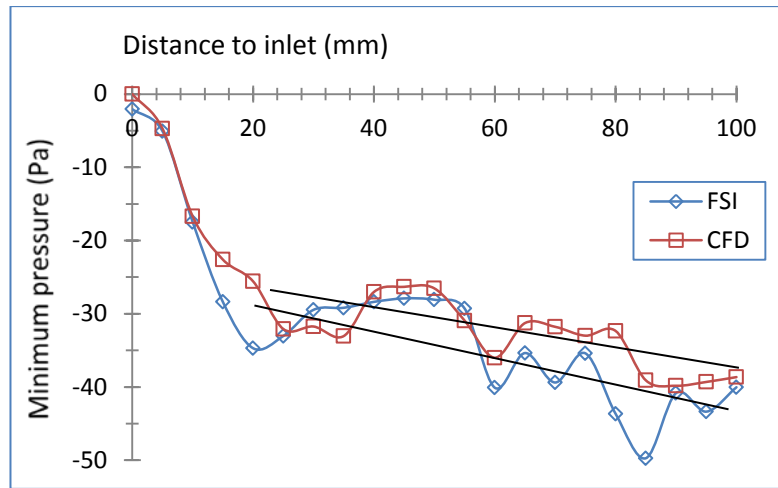
Note: Graphs show the minimum pressure value of each cross-section plane (Figures 65 and 66). The solid dark straight lines represent the pressure level in the oropharynx and hypopharynx.

Figure 70: Pressure Profiles of (a) Pre-treatment and (b) Post-treatment Models of Responder-1

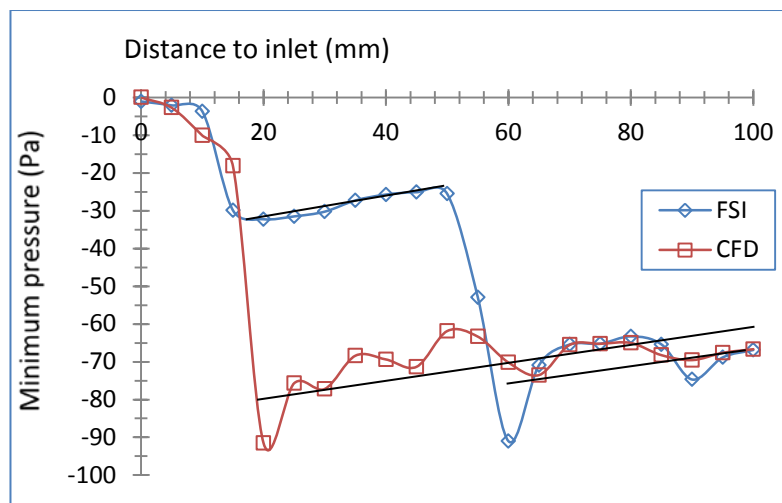
The minimum pressure along the airway calculated using CFD and FSI for Failure-2 (Figure 71) further proved the advantage of the FSI method by involving the structural analysis. The discrepancy of the minimum pressure at the oropharynx and hypopharynx was minor for the UA pre-treatment case, but marked for the post-treatment case. For the pre-treatment case, the minimum pressures level was in the lower velopharynx and oropharynx. A lower minimum pressure was found in the hypopharynx for the FSI result.

At the cross-sectional plane 85 mm from the inlet, the difference of the lowest pressure between the two results was 10.7 Pa. The narrowed lower hypopharynx in the FSI case induced a 25% (10.7 Pa) increase in the total UA pressure drop. This means that the FSI method is able to take into account the significant geometric changes that will affect pressure.

Figure 71-b indicates an enormous difference in the pressure profile using CFD and FSI. As aforementioned, the slight expansion of the velopharynx reduced the pressure drop by 65%, which increased the velopharyngeal pressure, while the collapsed wall at the higher hypopharynx generated a 66 Pa pressure drop from oropharynx. Similar minimum pressure levels were discovered in the mid to low hypopharynx. The total pressure drop values in the CFD and FSI results were very close (91.5 for CFD and 91.0 for FSI), although the locations were different.



(a) Pre-treatment case



(b) Post-treatment case

Note: Graphs show the minimum pressure value of each cross-section plane (Figures 65 and 66). The solid dark straight lines represent the pressure level in the oropharynx and hypopharynx.

Figure 71: Pressure Profiles of (a) Pre-treatment and (b) Post-treatment Models of Failure-2

The results showed that the maximum pressure drop (ΔP_{Max}) values were similar for the CFD and FSI models for the pre- and post-treatment cases (Figure 68). The ΔP_{Max} is a critical index because it can be used in the treatment predicting model of MAS (Section 4.7; $\Delta\sqrt{\Delta P_{Max}} \% \propto \Delta AHI\%$). The pressure predicted by the FSI result was considered more realistic because it encompassed the deformation of the UA wall. The ΔP_{Max} calculated with the CFD and FSI results of Responder-1 were close to each other. However, the ΔP_{Max} calculated using FSI for the Failure-2 pre-treatment model was

1 higher by 26.1% (39.1 Pa for CFD and 49.7 Pa for FSI). The higher pressure drop found
2 in the FSI case compared to the CFD led to a significant reduction of $\Delta\sqrt{\Delta P_{\text{Max}}}$ %
3 (from -98.4% in CFD to -56.2% in FSI). This may indicate that the treatment predicting
4 model developed from the CFD results should be verified with the FSI method. More
5 patient cases will be analysed to determine the correlation between the FSI pressure
6 results and the AHI changes.

7 **5.6 Summary**

8 This chapter modelled the collapse of the UA wall using the FSI modelling method. For
9 Responder-1, the UA wall of the pre-treatment case was fully collapsed at the left
10 region of the oropharynx. The post-treatment case demonstrated excellent resistance to
11 collapse because its geometry was larger in volume and lower in flow resistance. This
12 effectively controlled the pressure drop in the UA lumen. The opposite result was found
13 for patient Failure-2. The pre-treatment result demonstrated that the airway almost fully
14 closed, while the UA wall collapsed at the epiglottis area for the post-treatment case.
15 These FSI results were encouraging because the calculated treatment response agreed
16 with the clinical data (AHI). However, considering the large computational expense of
17 the FSI modelling method, the predictive accuracy of CFD simulations may be more
18 appropriate in a large-scale case study due to the reduced time involved, given that the
19 CFD analysis of a patient case can be finished within 20 hours, while the estimated FSI
20 modelling of a CFD case can take four to six weeks.

21

Chapter 6: Conclusion and Discussion

6.1 Introduction

The objective of this research was to use CFD to study the upper airflow characteristics of OSA patients and to use a two-way FSI to model the UA wall movement in correspondence to the changes from the UA airflow properties. The aim of this was to gain a greater understanding of air–tissue interactions in UA and develop a potentially effective method to predict the treatment response of MAS treatment. The conclusion of this research is summarised in Section 6.2, while Section 6.3 presents an overall discussion of this work and makes recommendations for future study.

6.2 Conclusions

The conclusions of the research presented in this thesis are summarised below.

Table 3 listed the major geometry changes in the UA of seven study cases after fitting MAS. The key indexes like volume increasing, widening in lateral or anti-posterior dimension of UA lumen showed no relationship with AHI changes. The enlargement of a restricted cross-section area was found to be the best geometrical parameter because it had a correlation coefficient of $R = 0.69$ and $P = 0.086$ to changes in AHI; however, the results still indicated that it was probably not sufficiently strong to predict the treatment response.

A 1:1 scale rigid UA model was designed in Pro/E and fabricated with rapid prototyping (3D printing), and then the pressure profile along the back of the lumen was captured. A comparison of the CFD and experimental pressure values was plotted in Figure 45, with the two results indicating a close match. The maximum discrepancy of 17% in static pressure was found at the velopharynx; however, much better agreement was achieved on the rest locations Overall, this CFD method was considered valid.

The flow structure and pressure distribution of the UA air domain of all seven studied cases were demonstrated in Figures 51 to 55. A pharyngeal jet was generated at the velopharynx, which resulted in a high air velocity. The sudden enlarged oral cavity

1 formed strong air circulations and turbulence. The maximum velocity and minimum
2 pressure were found in the restricted area for all cases.

3 The change in maximum pressure drop in the UA was proven to have a significant
4 correlation with the changes in AHI before and after MAS treatment. A potential
5 treatment prediction method was developed from $\Delta\sqrt{\Delta P_{\text{Max}}}$ % and $\Delta\text{AHI}\%$, which had
6 a correlation coefficient of 0.97 and *P* value of 0.000167 (Figure 56).

7 A 1:1 flexible thin-wall UA model was designed from Responder-1's UA geometry and
8 fabricated via SLA method. The material property (Young's modulus: 325 kPa,
9 Poisson's ratio: 0.306) of the soft material was determined via tensile testing. The same
10 material property and flow conditions were applied in the FSI modelling to match the
11 experiment. The wall movement of UA was compared between the virtual and physical
12 models, and an acceptable match was found. The maximum discrepancy was only 0.7
13 mm when the supply airflow was 434 ml/s. The computational model had a greater
14 velocity in wall collapsing at lower airflow; however, it finally slowed down and
15 matched the physical model.

16 The results of the FSI simulation of the cases for Responder-1 and Failure-2 were
17 presented in Figures 59 to 64. Airway total closure was found in the Responder-1 pre-
18 treatment case, with a maximum wall displacement of 5.2 mm at the back of the
19 oropharynx. This displacement was found to be negligible in the Responder-1 post-
20 treatment case. The FSI result of the Failure-2 post-treatment case showed a complete
21 UA collapse at the epiglottis, with a maximum wall displacement of 4.1 mm. Less wall
22 movement of 2.4 mm was found in the Failure-2 pre-treatment case, and the UA had a
23 small air gap of 2.1 mm between the epiglottis and posterior UA wall. Overall, the FSI
24 result was considered to match with the treatment response.

25 The large geometrical changes in the UA of the flexible wall cases resulted in different
26 pressure distributions in comparison with the rigid wall model. The Responder-1 pre-
27 treatment FSI result had a lower oropharyngeal and laryngeal pressure (average 9.1 Pa)
28 in comparison with the CFD result at the same flow boundary condition. The Failure-2
29 post-treatment FSI had a 65% higher velopharyngeal pressure, yet 24% lower pressure
30 at the epiglottis, which resulted in a completely different UA pressure pattern. Neither
31 case showed a significant difference in maximum UA pressure drop between the FSI

1 and CFD cases, which could indicate that the CFD-based treatment prediction method is
2 still valid.

3 **6.3 Discussion and Recommendations for Future Research**

4 This thesis demonstrated good concordance between the clinical treatment response and
5 simulation of the UA response to MAS, using CFD and patient-specific airway
6 geometries. The CFD analysis of UA flow was extended by using FSI analysis of an
7 OSA case treated with MAS, and this case showed improved UA flow. The results
8 indicated how an enlarged and less-deformable UA geometry revealed a positive
9 response that matched the clinical treatment response.

10 This is the first research to use FSI to examine the behaviour of the complete airway
11 and to provide a means to better understand UA collapse in OSA. Previous FSI studies
12 only modelled partial UA structures (such as the soft palate or tongue) and assumed a
13 rigid wall for the rest of the UA structures, which is a significant limitation [62, 63].
14 However, the pharyngeal airway is not sufficiently restricted by bony structures, and
15 lateral narrowing could be a dominant factor of UA collapse [2, 87]. The full pharyngeal
16 FSI model in this thesis overcame these limitations, while also providing experimental
17 validation. This thesis reproduced a significant lateral occlusion. This could be an early
18 stage of lateral narrowing, which was found to be a typical UA collapsing process in
19 regard to OSA [88]. This thesis indicated that flow-induced pressure variations alone
20 are sufficient to collapse the airway, which is important in treating OSA because
21 changing the flow can stop the collapse.

22 The FSI analysis of the UA with MAS showed less UA deformation, and no collapse of
23 the UA for the responder case. The opposite result was achieved for the failure case.
24 This is an important finding because it matches the clinical treatment response measured
25 on an overnight sleep study. Previous imaging studies have shown the MAS to enhance
26 UA dimensions, particularly in the velopharyngeal region [69]; however, geometrical
27 changes alone did not correspond with the treatment response. In the patients in the
28 current study, although there was a greater increase in velopharyngeal volume with
29 MAS, the prevention of UA deformation was observed in the oropharynx. The findings
30 in the current study of UA collapse behind the tongue (oropharynx region),
31 circumvented by MAS in a treatment responder, are interesting because a previous

1 clinical study measuring the site of UA collapse identified oropharyngeal ‘collapsers’ as
2 MAS treatment responders, while primary velopharyngeal ‘collapsers’ were not as
3 successful in MAS treatment [64].

4 Although the FSI model in this thesis represents a significant advance, this research had
5 some limitations. One potential limitation is describing the pharyngeal structure as a
6 ‘collapsible homogeneous tube’. The UA was reconstructed as an empty lumen
7 surrounded by a continuous wall with homogenous material properties and thickness.
8 This differs from the real situation, where the pharynx is surrounded by organs, such as
9 the tongue, soft palate and epiglottis. With 2 mm uniform wall thickness, the
10 velopharynx was defined as a narrow tube with a relatively thick wall. This tube could
11 only passively deform under low pressure force. The active movement of the
12 surrounding UA muscle group could not be included. In the respiratory cycle, the UA
13 muscles would provide extra force to the UA lumen, which may contribute to UA
14 collapse or prevent UA occlusion at certain times. Saboisky et al. [89] examined how
15 complex neural activity assisted the Genioglossus muscle in breathing activities, while
16 Eckert et al. [90] revealed that non-anatomic abnormalities could be a major factor of
17 OSA. Brown et al. [91] found that patients with more severe OSA (higher AHI) were
18 more likely to have less movement of tissues around the UA. However, the neuro-
19 mechanical activity in the UA was not integrated in the current FSI model due to the
20 limitation of modelling technologies and lack of comprehensive understanding.
21 However, it could be considered another important feature to improve the computational
22 UA model in the future.

23 In addition, the soft palate should have free movement in the anti-posterior direction,
24 and normally contributes to the retropalatal occlusion [63]. This soft palate motion
25 could not be reproduced by the current FSI model. Although a large pressure force in
26 the radial direction was found in the retropalatal region, the dominant plane-strain effect
27 resisted the force and prevented the wall from collapsing.

28 Another limitation of the current study was assuming the tissue property to be linear
29 elastic and isotropic, which contrasts with the known nonlinear feature of common
30 biomaterials. This could have resulted in an over-prediction of UA displacement. The
31 nasal cavity was also excluded in this UA model because it has comparatively high wall

1 rigidity and modelling complexity. Previous work has indicated that UA flow
2 parameters are not particularly sensitive to the nasal cavity [53].

3 Finally, performing FSI simulation on a complex 3D UA requires intensive
4 computational power, which limits its usage in normal clinical studies. However, with
5 the development of computing technology and hardware innovation, FSI has the
6 potential to be solved on a desktop PC within an acceptable time period.

7 The future scope of continuous research is to confirm the relationship between the FSI
8 results and treatment response through a large-case study. A complicated and more
9 realistic UA geometry will improve the accuracy of the FSI simulation to predict the
10 treatment response of MAS.

11

References

- 2 1. Guilleminault, C., R. Korobkin, and R. Winkle, *A review of 50 children with obstructive*
3 *sleep apnea syndrome*. Lung, 1981. **159**(1): p. 275-287.
- 4 2. Ayappa, I. and D.M. Rapoport, *The upper airway in sleep: physiology of the pharynx*.
5 *Sleep Medicine Reviews*, 2003. **7**(1): p. 9-33.
- 6 3. Young, T., et al., *The Occurrence of Sleep-Disordered Breathing among Middle-Aged*
7 *Adults*. New England Journal of Medicine, 1993. **328**(17): p. 1230-1235.
- 8 4. Redline, S., et al., *Risk factors for sleep-disordered breathing in children. Associations*
9 *with obesity, race, and respiratory problems*. Am J Respir Crit Care Med, 1999. **159**(5 Pt
10 1): p. 1527-32.
- 11 5. Ali, N.J., D.J. Pitson, and J.R. Stradling, *Snoring, sleep disturbance, and behaviour in 4-5*
12 *year olds*. Archives of Disease in Childhood, 1993. **68**(3): p. 360-366.
- 13 6. Young, T., P.E. Peppard, and D.J. Gottlieb, *Epidemiology of Obstructive Sleep Apnea*.
14 *American Journal of Respiratory and Critical Care Medicine*, 2002. **165**(9): p. 1217-1239.
- 15 7. Gastaut, H., C.A. Tassinari, and B. Duron, [*Polygraphic study of diurnal and nocturnal*
16 *(hypnic and respiratory) episodal manifestations of Pickwick syndrome*]. Rev Neurol
17 (Paris), 1965. **112**(6): p. 568-79.
- 18 8. Badr, M.S., *Pathogenesis of obstructive sleep apnea*. Prog Cardiovasc Dis, 1999. **41**(5):
19 p. 323-30.
- 20 9. Duron, B., et al., *Les pauses respiratoires survenant au cours du sommeil chez l'homme*.
21 *CR Soc. Biol*, 1967. **161**: p. 634-639.
- 22 10. Lugaresi, E., et al., [*"Ondine's curse": the disorder of respiration and sleep in primary*
23 *alveolar hypoventilation*]. Sist Nerv, 1968. **20**(1): p. 27-37.
- 24 11. Kuhlo, W., E. Doll, and M.C. Franck, [*Successful management of Pickwickian syndrome*
25 *using long-term tracheostomy*]. Dtsch Med Wochenschr, 1969. **94**(24): p. 1286-90.
- 26 12. Pathology, E.S.f.C.R., *Hypersomnia with Periodic Breathing*. 1972.
- 27 13. Roux, F., C. D'Ambrosio, and V. Mohsenin, *Sleep-related breathing disorders and*
28 *cardiovascular disease*. The American Journal of Medicine, 2000. **108**(5): p. 396-402.
- 29 14. Young T, S.J.P.P.E., *Risk factors for obstructive sleep apnea in adults*. JAMA, 2004.
30 **291**(16): p. 2013-2016.
- 31 15. Redline, S., et al., *Racial differences in sleep-disordered breathing in African-Americans*
32 *and Caucasians*. Am J Respir Crit Care Med, 1997. **155**(1): p. 186-92.
- 33 16. Cakirer, B., et al., *The relationship between craniofacial morphology and obstructive*
34 *sleep apnea in whites and in African-Americans*. Am J Respir Crit Care Med, 2001.
35 **163**(4): p. 947-50.
- 36 17. Coltman, R., et al., *Craniofacial form and obstructive sleep apnea in Polynesian and*
37 *Caucasian men*. Sleep, 2000. **23**(7): p. 943-50.
- 38 18. Ip, M.S., et al., *A community study of sleep-disordered breathing in middle-aged*
39 *Chinese women in Hong Kong: prevalence and gender differences*. Chest, 2004. **125**(1):
40 p. 127-34.
- 41 19. Young, T., P.E. Peppard, and D.J. Gottlieb, *Epidemiology of obstructive sleep apnea: a*
42 *population health perspective*. Am J Respir Crit Care Med, 2002. **165**(9): p. 1217-39.
- 43 20. Young, T., P.E. Peppard, and S. Taheri, *Excess weight and sleep-disordered breathing*. J
44 *Appl Physiol*, 2005. **99**(4): p. 1592-9.
- 45 21. Netter, F.H., *Atlas of Human Anatomy*. 2010: Elsevier Health Sciences.
- 46 22. Jeong, S.-J., W.-S. Kim, and S.-J. Sung, *Numerical investigation on the flow*
47 *characteristics and aerodynamic force of the upper airway of patient with obstructive*
48 *sleep apnea using computational fluid dynamics*. Medical Engineering & Physics, 2007.
49 **29**(6): p. 637-651.

- 1 23. Vos, W., et al., *Correlation between severity of sleep apnea and upper airway*
2 *morphology based on advanced anatomical and functional imaging*. Journal of
3 Biomechanics, 2007. **40**(10): p. 2207-2213.
- 4 24. Sun, X., et al., *Numerical simulation of soft palate movement and airflow in human*
5 *upper airway by fluid-structure interaction method*. Acta Mechanica Sinica, 2007. **23**(4):
6 p. 359-367.
- 7 25. Wang, Y., et al., *Numerical analysis of respiratory flow patterns within human upper*
8 *airway*. Acta Mechanica Sinica, 2009. **25**(6): p. 737-746.
- 9 26. Schwab, R.J., et al., *Identification of upper airway anatomic risk factors for obstructive*
10 *sleep apnea with volumetric magnetic resonance imaging*. Am J Respir Crit Care Med,
11 2003. **168**(5): p. 522-30.
- 12 27. Chouly, F., et al., *Simulation of the Retroglossal Fluid-Structure Interaction During*
13 *Obstructive Sleep Apnea*, in *Biomedical Simulation*, M. Harders and G. Székely, Editors.
14 2006, Springer Berlin Heidelberg. p. 48-57.
- 15 28. Huynh, J., K.B. Kim, and M. McQuilling, *Pharyngeal Airflow Analysis in Obstructive*
16 *Sleep Apnea Patients Pre- and Post-Maxillomandibular Advancement Surgery*. Journal
17 of Fluids Engineering, 2009. **131**(9): p. 091101-10.
- 18 29. Hoffstein, V., J.H. Mateika, and S. Mateika, *Snoring and sleep architecture*. Am Rev
19 Respir Dis, 1991. **143**(1): p. 92-6.
- 20 30. Vgontzas, A.N., et al., *Sleep apnea and sleep disruption in obese patients*. Arch Intern
21 Med, 1994. **154**(15): p. 1705-11.
- 22 31. Tangugsorn, V., et al., *Obstructive sleep apnea: a canonical correlation of*
23 *cephalometric and selected demographic variables in obese and nonobese patients*.
24 Angle Orthod, 2001. **71**(1): p. 23-35.
- 25 32. Rajala, R., et al., *Obstructive sleep apnoea syndrome in morbidly obese patients*. J
26 Intern Med, 1991. **230**(2): p. 125-9.
- 27 33. Busetto, L., et al., *Obstructive sleep apnea syndrome in morbid obesity: effects of*
28 *intra-gastric balloon*. Chest, 2005. **128**(2): p. 618-23.
- 29 34. Fleisher, K.E. and A.C. Krieger, *Current trends in the treatment of obstructive sleep*
30 *apnea*. J Oral Maxillofac Surg, 2007. **65**(10): p. 2056-68.
- 31 35. Davies, R.J., N.J. Ali, and J.R. Stradling, *Neck circumference and other clinical features in*
32 *the diagnosis of the obstructive sleep apnoea syndrome*. Thorax, 1992. **47**(2): p. 101-5.
- 33 36. Oksenberg, A., et al., *Positional vs nonpositional obstructive sleep apnea patients:*
34 *anthropomorphic, nocturnal polysomnographic, and multiple sleep latency test data*.
35 Chest, 1997. **112**(3): p. 629-39.
- 36 37. Ferguson, K.A., et al., *Oral appliances for snoring and obstructive sleep apnea: a review*.
37 Sleep, 2006. **29**(2): p. 244-62.
- 38 38. Krieger, J., et al., *Long-term compliance with CPAP therapy in obstructive sleep apnea*
39 *patients and in snorers*. Sleep, 1996. **19**(9 Suppl): p. S136-43.
- 40 39. Aneeza, W.H., et al., *Effects of uvulopalatopharyngoplasty: a seven year review*. Med J
41 Malaysia, 2011. **66**(2): p. 129-32.
- 42 40. Riley, R.W., N.B. Powell, and C. Guilleminault, *Maxillofacial surgery and obstructive*
43 *sleep apnea: a review of 80 patients*. Otolaryngology--head and neck surgery : official
44 journal of American Academy of Otolaryngology-Head and Neck Surgery, 1989. **101**(3):
45 p. 353-361.
- 46 41. PRINSELL, J.R., *Maxillomandibular advancement surgery for obstructive sleep apnea*
47 *syndrome*. The Journal of the American Dental Association, 2002. **133**(11): p. 1489-
48 1497.
- 49 42. Gotsopoulos, H., et al., *Oral Appliance Therapy Improves Symptoms in Obstructive*
50 *Sleep Apnea*. American Journal of Respiratory and Critical Care Medicine, 2002. **166**(5):
51 p. 743-748.

- 1 43. Grover, F.L., *The role of CT and MRI in staging of the mediastinum*. Chest, 1994. **106**(6
2 Suppl): p. 391S-396S.
- 3 44. Chan, A.S., et al., *Nasopharyngoscopic evaluation of oral appliance therapy for*
4 *obstructive sleep apnoea*. Eur Respir J, 2010. **35**(4): p. 836-42.
- 5 45. MEHTA, A., et al., *A Randomized, Controlled Study of a Mandibular Advancement Splint*
6 *for Obstructive Sleep Apnea*. American Journal of Respiratory and Critical Care
7 Medicine, 2001. **163**(6): p. 1457-1461.
- 8 46. Ng, A.T., et al., *Effect of Oral Appliance Therapy on Upper Airway Collapsibility in*
9 *Obstructive Sleep Apnea*. American Journal of Respiratory and Critical Care Medicine,
10 2003. **168**(2): p. 238-241.
- 11 47. Yu, G., Z. Zhang, and R. Lessmann, *Fluid Flow and Particle Diffusion in the Human*
12 *Upper Respiratory System*. Aerosol Science and Technology, 1998. **28**(2): p. 146-158.
- 13 48. Martonen, T., et al., *Flow simulation in the human upper respiratory tract*. Cell
14 Biochemistry and Biophysics, 2002. **37**(1): p. 27-36.
- 15 49. Heenan, A.F., et al., *Experimental measurements and computational modeling of the*
16 *flow field in an idealized human oropharynx*. Experiments in Fluids, 2003. **35**(1): p. 70-
17 84.
- 18 50. Collins, T.P., G.R. Tabor, and P.G. Young, *A computational fluid dynamics study of*
19 *inspiratory flow in orotracheal geometries*. Medical & Biological Engineering &
20 Computing, 2007. **45**(9): p. 829-836.
- 21 51. Xu, C., et al., *Computational fluid dynamics modeling of the upper airway of children*
22 *with obstructive sleep apnea syndrome in steady flow*. Journal of Biomechanics, 2006.
23 **39**(11): p. 2043-2054.
- 24 52. Schroeter, J.D., J.S. Kimbell, and B. Asgharian, *Analysis of particle deposition in the*
25 *turbinate and olfactory regions using a human nasal computational fluid dynamics*
26 *model*. Journal of aerosol medicine, 2006. **19**(3): p. 301-313.
- 27 53. Persak, S.C., et al., *Noninvasive estimation of pharyngeal airway resistance and*
28 *compliance in children based on volume-gated dynamic MRI and computational fluid*
29 *dynamics*. J Appl Physiol, 2011. **111**(6): p. 1819-27.
- 30 54. Wen, J., et al., *Numerical simulations for detailed airflow dynamics in a human nasal*
31 *cavity*. Respiratory Physiology & Neurobiology, 2008. **161**(2): p. 125-135.
- 32 55. Hahn, I., P.W. Scherer, and M.M. Mozell, *Velocity profiles measured for airflow through*
33 *a large-scale model of the human nasal cavity*. J Appl Physiol, 1993. **75**(5): p. 2273-87.
- 34 56. Schroter, R.C. and M.F. Sudlow, *Flow patterns in models of the human bronchial*
35 *airways*. Respir Physiol, 1969. **7**(3): p. 341-55.
- 36 57. Zhao, Y. and B.B. Lieber, *Steady Expiratory Flow in a Model Symmetric Bifurcation*.
37 Journal of Biomechanical Engineering, 1994. **116**(3): p. 318-323.
- 38 58. Van Hirtum, A., X. Pelorson, and P.Y. Lagree, *In vitro validation of some flow*
39 *assumptions for the prediction of the pressure distribution during obstructive sleep*
40 *apnoea*. Med Biol Eng Comput, 2005. **43**(1): p. 162-71.
- 41 59. De Backer, J.W., et al., *Functional imaging using computational fluid dynamics to*
42 *predict treatment success of mandibular advancement devices in sleep-disordered*
43 *breathing*. Journal of Biomechanics, 2007. **40**(16): p. 3708-3714.
- 44 60. Mylavarapu, G., et al., *Validation of computational fluid dynamics methodology used*
45 *for human upper airway flow simulations*. J Biomech, 2009. **42**(10): p. 1553-9.
- 46 61. Martonen, T.B., et al., *Flow simulation in the human upper respiratory tract*. Cell
47 Biochem Biophys, 2002. **37**(1): p. 27-36.
- 48 62. Chouly, F., et al., *Numerical and experimental study of expiratory flow in the case of*
49 *major upper airway obstructions with fluid–structure interaction*. Journal of Fluids and
50 Structures, 2008. **24**(2): p. 250-269.

- 1 63. Wang, Y., et al., *Fluid–structure interaction modeling of upper airways before and after*
2 *nasal surgery for obstructive sleep apnea*. International Journal for Numerical Methods
3 in Biomedical Engineering, 2012. **28**(5): p. 528-546.
- 4 64. Ng, A.T., J. Qian, and P.A. Cistulli, *Oropharyngeal collapse predicts treatment response*
5 *with oral appliance therapy in obstructive sleep apnea*. Sleep, 2006. **29**(5): p. 666-71.
- 6 65. Ng, A., et al., *Cephalometry and prediction of oral appliance treatment outcome*. Sleep
7 and Breathing, 2012. **16**(1): p. 47-58.
- 8 66. Van Holsbeke, C., et al., *Anatomical and functional changes in the upper airways of*
9 *sleep apnea patients due to mandibular repositioning: A large scale study*. Journal of
10 Biomechanics, 2011. **44**(3): p. 442-449.
- 11 67. Rasani, M.R., K. Inthavong, and J.Y. Tu, *Simulation of Pharyngeal Airway Interaction*
12 *with Air Flow Using Low-Re Turbulence Model*. Modelling and Simulation in
13 Engineering, 2011. **2011**.
- 14 68. Mehta, A., et al., *A Randomized, Controlled Study of a Mandibular Advancement Splint*
15 *for Obstructive Sleep Apnea*. American Journal of Respiratory and Critical Care
16 Medicine, 2001. **163**(6): p. 1457-1461.
- 17 69. Chan, A.S.L., et al., *The effect of mandibular advancement on upper airway structure in*
18 *obstructive sleep apnoea*. Thorax, 2010. **65**(8): p. 726-732.
- 19 70. Mavriplis, D., *Unstructured grid techniques*. Annual Review of Fluid Mechanics, 1997.
20 **29**(1): p. 473-514.
- 21 71. Munson, B.R., et al., *Fundamentals of fluid mechanics*. 2009: Wiley.
- 22 72. Wilcox, D.C., *Turbulence Modeling for CFD*. 1994: DCW Industries, Incorporated.
- 23 73. Boussinesq, J., *Essai sur la théorie des eaux courantes*. 1877: Imprimerie Nationale.
- 24 74. Menter, F.R., *Performance of popular turbulence model for attached and separated*
25 *adverse pressure gradient flows*. AIAA Journal, 1992. **30**(8): p. 2066-2072.
- 26 75. Zhao, M., et al., *Computational fluid dynamics for the assessment of upper airway*
27 *response to oral appliance treatment in obstructive sleep apnea*. J Biomech, 2013.
28 **46**(1): p. 142-50.
- 29 76. Javidinejad, A., *FEA Practical Illustration of Mesh-Quality-Results Differences between*
30 *Structured Mesh and Unstructured Mesh*. ISRN Mechanical Engineering, 2012. **2012**: p.
31 7.
- 32 77. Birch, M.J. and P.D. Srodon, *Biomechanical properties of the human soft palate*. Cleft
33 Palate Craniofac J, 2009. **46**(3): p. 268-74.
- 34 78. Xu, C., et al., *Modeling upper airway collapse by a finite element model with regional*
35 *tissue properties*. Med Eng Phys, 2009. **31**(10): p. 1343-8.
- 36 79. Cheng, S., et al., *Viscoelastic properties of the tongue and soft palate using MR*
37 *elastography*. J Biomech, 2011. **44**(3): p. 5-5.
- 38 80. UnitedSensorCorp. *Pitot-Static Properties & Characteristics 2011* [cited 2015
39 April,2015]; Available from: <http://www.unitedsensorcorp.com/pitot-properties.html>.
- 40 81. Isono, S., et al., *Interaction of cross-sectional area, driving pressure, and airflow of*
41 *passive velopharynx*. J Appl Physiol (1985), 1997. **83**(3): p. 851-9.
- 42 82. Henke, K.G., D.E. Frantz, and S.T. Kuna, *An oral elastic mandibular advancement device*
43 *for obstructive sleep apnea*. Am J Respir Crit Care Med, 2000. **161**(2 Pt 1): p. 420-5.
- 44 83. Bosshard, V., J.F. Masse, and F. Series, *Prediction of oral appliance efficiency in patients*
45 *with apnoea using phrenic nerve stimulation while awake*. Thorax, 2011. **66**(3): p. 220-
46 5.
- 47 84. Pedley, T.J. and X.Y. Luo, *Modelling Flow and Oscillations in Collapsible Tubes*.
48 Theoretical and Computational Fluid Dynamics, 1998. **10**(1-4): p. 277-294.
- 49 85. Bertram, C., et al., *Aperiodic flow-induced oscillations of collapsible tubes: a critical*
50 *reappraisal*. Medical engineering & physics, 2004. **26**(3): p. 201-214.
- 51 86. Heil, M. and S.L. Waters, *How rapidly oscillating collapsible tubes extract energy from a*
52 *viscous mean flow*. Journal of Fluid Mechanics, 2008. **601**(1): p. 199-227.

- 1 87. Pohunek, P., *Development, structure and function of the upper airways*. Paediatric
2 Respiratory Reviews, 2004. **5**(1): p. 2-8.
- 3 88. Rodenstein, D.O., et al., *Pharyngeal shape and dimensions in healthy subjects, snorers,
4 and patients with obstructive sleep apnoea*. Thorax, 1990. **45**(10): p. 722-727.
- 5 89. Saboisky, J.P., et al., *Tonic and phasic respiratory drives to human genioglossus
6 motoneurons during breathing*. J Neurophysiol, 2006. **95**(4): p. 2213-21.
- 7 90. Eckert, D.J., et al., *Defining phenotypic causes of obstructive sleep apnea. Identification
8 of novel therapeutic targets*. Am J Respir Crit Care Med, 2013. **188**(8): p. 996-1004.
- 9 91. Brown, E.C., et al., *Respiratory Movement of Upper Airway Tissue in Obstructive Sleep
10 Apnea*. Sleep, 2013. **36**(7): p. 1069-1076.

11

1

Appendix B: The Study Case Data Sheet

Study case	AHI- without MAS	AHI- with MAS	AHI- change	AHI- %change	Age	Gender	Height	Weight	BMI	Neck circumference
Reponder-1	41.5	2.1	-39.4	-94.9	52	M	170	85	29.41	42
Responder-2	22.2	0	-22.2	-100.0	24	M	174	105	34.68	43
Responder-3	14.2	4.1	-10.1	-71.1	43	M	183.5	90	26.73	41.5
Partial- responder	28.4	13.9	-14.5	-51.1	31	M	175	74.3	24.26	38
Non- responder	29.2	23.6	-5.6	-19.2	49	M	166	101	36.65	41
Failure-1	19.5	25	5.5	28.2	65	M	171	73.5	25.10	38
Failure-2	16.0	31.7	15.7	98.1	57	M	168	80	28.34	40

2

3

4

1

Appendix C: Engineering Drawings

2